"DEVELOPMENT OF A LOW COST SHOCK PRESSURE SENSOR"

A Thesis Presented to

The Faculty of the College of Engineering and Technology

Ohio University

In Partial Fulfillment

of the Requirements for the Degree

Master of Science

by

SYED FARHAT ABBAS

March, 1988

ACKNOWLEDGEMENTS

I wish to express my sincere thanks to my advisors Dr. J. S. Gunasekera and Dr. D. E. Scheck, for their valuable advice and help during the course of this thesis.

I also wish to express my deep gratitude to Dr. Calvin Konya, without whose advice and support this study would not have been possible.

Finally, I wish to thank my parents for their constant encouragement and patience.

January 1988 Syed Farhat Abbas

TABLE OF CONTENTS

TABLE OF CONTENTS (CONTINUED)

TABLE OF CONTENTS (CONTINUED)

TABLE OF CONTENTS (CONTINUED)

LIST OF FIGURES

LIST OF FIGURES (CONTINUED)

LIST OF TABLES

CHAPTER 1

INTRODUCTION

Applications that require stress-wave analysis arose in the early 1940's in connection with nuclear weapon design. With the introduction of realistic constitutive models of material strength, these analyses have found wide application to nuclear weapon effects, to conventional ordnance problems such as interior and terminal ballistics and fragmentation, and to a rapidly expanding range of non-military applications ranging from explosive forming and processing, percussive rock breakage and explosive excavation to reactor accident analysis.

Increasing competition in industry and emerging frontiers in science and technology lead to ever-increasing additional demands for more accurate analyses of physical processes. These demands call for better understanding of the material behavior to the high amplitude stress waves, reducing the number of assumptions and simplifications in the problem formulation. A salient feature of the propagation of high amplitude stress waves in solid materials is the presence of shock waves. Even if shock waves are not introduced by discontinuities in the initial/boundary data, they may arise spontaneously in the

body by steepening of the compressive waves due to nonlinear response of the material. Although shock waves cannot exist as mathematical discontinuities in real materials, but on a molecular scale, shock waves may nevertheless be very thin. Another feature of stress wave propagation is the presence of acceleration waves, that is, discontinuities in stress and strain gradients. The presence of shock and acceleration waves implies that stress wave solutions possess a substantially high frequency content. Any numerical method which relies on a discretization of space (e.g finite element method) will act as a low pass filter that removes components with a wavelength smaller than twice to four times the spatial mesh size. It is almost always prohibitive, in engineering calculations, to provide a sufficiently fine numerical grid so that physically realistic shock and acceleration wave thicknesses are resolved. Consequently, special provisions are necessary to accommodate shock and acceleration waves. These phenomena are discussed in Chapter 7.

The experimental measurement of stress-time histories in shock-loaded materials has historically been a very difficult task. Since little is known a priori about the piezoelectric response under high-stress, short-duration loading, confidence in the gauge responses rests upon extensive experimental investigations of the properties of

the gauge materials under controlled loading conditions. Individual transducers cannot be calibrated under conditions of use since the tests are destructive. The meteoritic character of the events with their short durations (typically 1 micro second), high pressures, and high-velocity deformations isolate the experimenter from any direct intuitive contact. As a result, most of the presently accepted views and differences in views of material response are strongly influenced by details of the instrumentation used in the experiment. Improvements in experimental technique and the development of complex computer codes have dominated the technical advances in the field, and it appears that instrumentation and experimental technique will continue to play a leading role.

At present, quartz and manganin transducers are routinely used to determine the shock pressures. However, these gauges are found to be less than satisfactory because of their physical form and inability to track the release portion of the stress history. Moreover, their high cost has been a barrier to their wide spread use in industrial applications.

In the present investigation, a new low cost shock pressure transducer is developed. It is capable of recording stress pulses up to 20 Kbar with durations of

several micro seconds. Epon 828-Z epoxy is the potting material and Polyvinylidene Fluoride (PVDF) polymer is used as the pressure sensing element. Polyvinylidene Fluoride, a newly available piezoelectric transducer material for stress gauges, is useful in shock wave propagation studies (Crystalline quartz and tourmaline and ceramic $BaTiO_3$ and PZT have previously been used). The material is sensitive, versatile, well characterized, give reproducible results and readily available from several sources [1].

In piezoelectric materials, the time varying electric displacement serves as a communication link that permits the downstream boundary conditions to influence the stress through the electromechanical coupling constant, and affect the shock wave even during its first transit. This effect has been modeled into the constitutive equations to describe the transient electromechanical response of the piezoelectric sensing element. This constitutive model is implemented using a modified version of a one-dimensional finite difference wave propagation code (WONDY), developed by Sandia National Laboratories, Albuquerque. This computer code treats shock waves by the method of artificial viscosity and employs a dynamic rezoning technique to provide a desired degree of resolution with a minimum amount of computer time.

The resulting shock pressure transducer is tested using a compressed gas gun, the components of which were loaned by Battelle Laboratories Columbus Division. This equipment allows testing the transducer over a wide range of shock loading under very reproducible conditions.

In this report, Chapter 2 is a review of existing shock pressure transducers. Chapter 3 covers the basic theory of shock wave propagation in solid media. The selection process for the pressure sensing element and the potting material is discussed in Chapter 4 and 5 respectively. Chapter 6 contains the heat transfer analyses of the shock pressure transducer. The constitutive modeling of the pressure sensing element and the potting material is done in Chapter 7. Chapter 8 covers the experimental setup used for performing the compressed gas gun experiment. Results and conclusions are discussed in Chapter 9.

CHAPTER 2

SURVEY OF DIFFERENT SHOCK PRESSURE MEASURING SYSTEMS

The time-resolved measurements of stress wave profiles must be carried out in an extremely short time, since such high energy densities cannot be steadily maintained. Experimental measurements must be read from a remote location, since the energy densities involved cannot be dissipated in a nondestructive manner and, the diagnostics must be as complete as possible, since the system cannot be returned to its original state for a verification of the measured results.

Certain solid-state materials are electrically responsive to mechanical force; they often are used as the mechanical-to-electrical conversion devices in shock pickups. Generally exhibiting high elastic stiffness, these materials can be divided into two categories [4]: the self-generating type, in which electric charge is generated as a direct result of applied force, and the passive-circuit type, in which applied force causes a change in the electrical characteristics of the material. Piezoelectric materials are of the self-generating type. In the linear elastic range, a piezoelectric material produces an electric charge proportional to stress. Passive-circuit types of materials include magnetostrictive

and piezoresistive materials. A magnetostrictive material has a magnetic permeability which depends upon applied force; a piezoresistive material has an electrical resistance which depends upon applied force. The use of manganin piezoresistive, quartz piezoelectric and lithium niobate piezoelectric gauges to measure wave profiles are discussed in detail below. The problems associated with these time-resolved stress wave profile detectors are also discussed.

2.1 Manganin Piezoresistive Gauge

Measurements of the resistance of manganin coils immersed in pressurized fluids have long been used to accurately determine pressure in hydrostatic experiments at up to 2.5 GPa. The success of this application lead to developing analogous techniques for the measurement of stresses induced by shock loading.

In early hydrostatic experiments, various investigators recognized that non-homogeneous stresses had undesirable effects on the performance of manganin gauges. In fact, standard hydrostatic usage requires that a gauge be 'seasoned' by application of elevated temperature or pressure to eliminate irreproducibility and hysteresis. In contrast to the extreme care taken in hydrostatic experiments, shock loading by its very nature produces massive plastic deformation which introduces numerous

defects. The extent of these deformations are sensitive to local conditions surrounding the gauge element; thus, it is not surprising that the principal difficulties with the Manganin gauge for stress-profile measurements are associated with the methods of controlling the deformation of the gauge element. In spite of these difficulties, however, the Manganin gauge has proven quite useful for a variety of measurements and appears to be especially suitable in situations where measurement accuracy of 5 to 10 percent is acceptable.

Manganin is a commercial alloy (usually 84 wt% Cu, 12 wt% Mn, 4 wt% Ni). Its resistance is insensitive to temperature at atmospheric pressure. (Shock-loading investigations conducted to date indicate that resistance changes due to shock heating are small compared to other errors.) In nominal application, Manganin piezoresistive elements, either wires or foils, are encased in an insulator and exposed to the stress pulses. The initial resistance of the gauge and the change in resistance induced by the stress pulse are detected on a high-speed oscilloscope. On the assumption that the change in resistance is a unique function, the stress, σ_x, is related to the resistance change, ΔR by the relation

$$\sigma_x = \Delta R / K R_o \qquad \text{---- (1)}$$

where K is the piezoresistance coefficient, and R_o is the initial resistance of the gauge. Investigations of the change in resistance of Manganin gauges under well-controlled impact loading are required to measure its parameters such as K for a particular configuration and to establish linearity, reproducibility, and geometric effects. The principal characteristics of the Manganin gauge are [2]

(i) total recording time depends on the stress, and is typically about 5 micro seconds;

(ii) the stress range is from 1 to 30 GPa;

(iii) the accuracy is about 5 to 10 percent;

(iv) time resolution for changes in stress is about 50 to 100 nano seconds;

(v) there is a limitation to plane-wave measurements owing to wire stretching in two-dimensional strain fields;

(vi) it is possible to carry out in-material measurements.

Manganin has proven quite useful for a wide variety of measurements and further study of gauge configurations will no doubt improve performance characteristics.

2.2 Quartz Piezoelectric Gauge

Compressed gas gun experiments have established the quartz gauge as a very accurate shock pressure sensor.

These experiments used precisely aligned X-cut quartz impactors hitting quartz samples. The impactor velocity is measured with an accuracy of 0.1 percent. Owing to the symmetry of the impact configuration, the particle velocity imparted to the sample is one-half the impact velocity. Current pulses from the samples were measured with low-impedance resistive circuits and the current pulses were analyzed with electrostatic models to obtain piezoelectric, dielectric, and mechanical properties.

These investigations indicate that a shunted guard-ring gauge configuration [3] which follows specified design rules exhibits a universal response characteristic which is accurate to within 1 to 1.5% for step loading. Furthermore, the limiting input conditions under which gauges will respond with fidelity are the same for all gauges which are designed to the specified shunted guard-ring gauge configuration. The principal characteristics of quartz gauges are as follows [2]:

(i) maximum stress limit is 4 GPa;

(ii) maximum recording time is 1 to 2 micro seconds;

(iii) typical detector diameter is 10 mm;

(iv) specific restrictions are placed on gauge geometry to achieve universal response;

(v) time resolution is inherently subnanosecond but in most cases it is limited by nonplanarity of waves;

(vi) measurements are limited to plane-wave experiments.

The quartz gauge is widely used because of its relative simplicity, its large output signal (typically 10 V GPa^{-1} into a 50Ω load), self-powered operation, direct reading characteristics and precise characterization.

2.3 Lithium Niobate Piezoelectric Gauge

Recent work on lithium niobate, a new piezoelectric crystal, has shown that it can provide unusually large output signals from low level stresses and small sensor areas. The latter feature is important where miniaturization is necessary [2]. Lithium niobate gauges have proven useful for free field stress wave measurement under a diversity of field conditions. Although the lithium niobate gauges are reliable up to several kilobars, the distinctive feature of this gauge system is its ability to reproducibly record stress levels in the range below 1 Kbar to a few bars with very high signal-to-noise ratio.

Unfavorable characteristics of the lithium niobate, relative to stress gauge application, are shared with other stable piezoelectric materials. Lithium niobate is brittle and may fracture under intense bending or shear loading. Charge output during failure has not been well studied. Gauge elements tend to be thick compared to resistive elements. The pyroelectric output of transiently heated gauges does produce substantial noise output in non-

isothermal applications, however, this problem is much less severe than for $BaTiO_3$ and PZT ceramics. Sensitivity to transverse stress is substantial for the y-cut (it may be very small for z-cut) as it is for most piezoelectric and resistive gauge elements. The adverse properties must be overcome by appropriate packaging of the sensor element and restricting its application to appropriate measurement situations. Nevertheless, the various lithium niobate gauges appear to offer important new features to the family of piezoelectric gauges.

CHAPTER 3

SHOCK WAVES IN SOLID MEDIA

Measurements of the performance of the explosives are essential for evaluating the effectiveness of rock-fragmentation, rock-fracturing and for computer simulations of the blast [5]. The chemical energy released in a blast takes the form of a detonation wave, the velocity of which depends on the rate of energy release, density of the explosive and the charge diameter [6]. The determination of the pressure in the detonation wave is possible by studying the characteristics of the shock wave transmitted from the explosive into the surrounding solid media. This chapter covers some basic theory of shock wave propagation in solid media.

3.1 Basic Shock Relations

Based on the assumption that the shock wave profile is steady in time, the Rankine-Hugoniot equations have been developed. These equations relate the pressure (P), internal energy (E), specific volume (v), or density (ρ) behind the shock wave to these same quantities in front of the shock wave in terms of the shock velocity (u_s) and the particle velocity (u_p) due to the shock wave. These

equations express the conservation of mass, momentum, and energy, and, for a coordinate system in which the material in front of the shock wave is at rest, they are, respectively,

$$\rho_o u_s = \rho(u_s - u_p) \qquad \text{---- (2)}$$

$$p - p_o = \rho_o u_s u_p \qquad \text{---- (3)}$$

$$[(E - E_o) - u_p^2/2] \rho_o u_s = p_o u_p \qquad \text{---- (4)}$$

where, the zero subscript refers to the initial state and is often referred to as the centering point of that Hugoniot. Equation (2) and (3) can be combined to give

$$u_s = v_o [(p - p_o)/(v_o - v)]^{1/2} \qquad \text{---- (5)}$$

and

$$u_p = [(p - p_o)(v_o - v)]^{1/2} \qquad \text{---- (6)}$$

By substituting (5) and (6) into equation (4) the well known Hugoniot energy equation is obtained

$$E - E_o = (p + p_o)(v_o - v) / 2 \qquad \text{---- (7)}$$

The definition of these variables and their dimensions are as follows:

p = pressure, bar(N/m^2),

ρ = density, Kg/m^3,

v = specific volume, m^3/Kg,

E = specific internal energy, $bar\text{-}m^3/Kg$

u_p = particle velocity, or bulk velocity behind the shock front, m/sec

u_s = shock wave velocity, m/sec

Any travelling wave which connects these two end states, and which satisfies above equations is called a shock wave. The locus of states (p,v) which satisfy the above equations is called the Rankine-Hugoniot (p,v) curve centered at (p_o,v_o) or, more simply, the Hugoniot or R-H curve. It is also sometimes called the dynamic adiabat or shock adiabat.

The above relations can be fully understood by considering the p-v curve for a typical sample material [7], which is given in figure 1. In this figure, polymorphic transitions in the solid state are ignored. It is important to note that the curves represented here are projections into the p-v plane from an equation-of-state surface in p-v-E or p-v-t space. For example, an isotherm in this plane is the projection onto the p-v plane, of the intersection of the t = constant plane with the p-v-t equation-of-state surface. In Figure 1, the isentrope and isotherm represent a series of states which can be realized continuously, while Hugoniot represents the locus of all

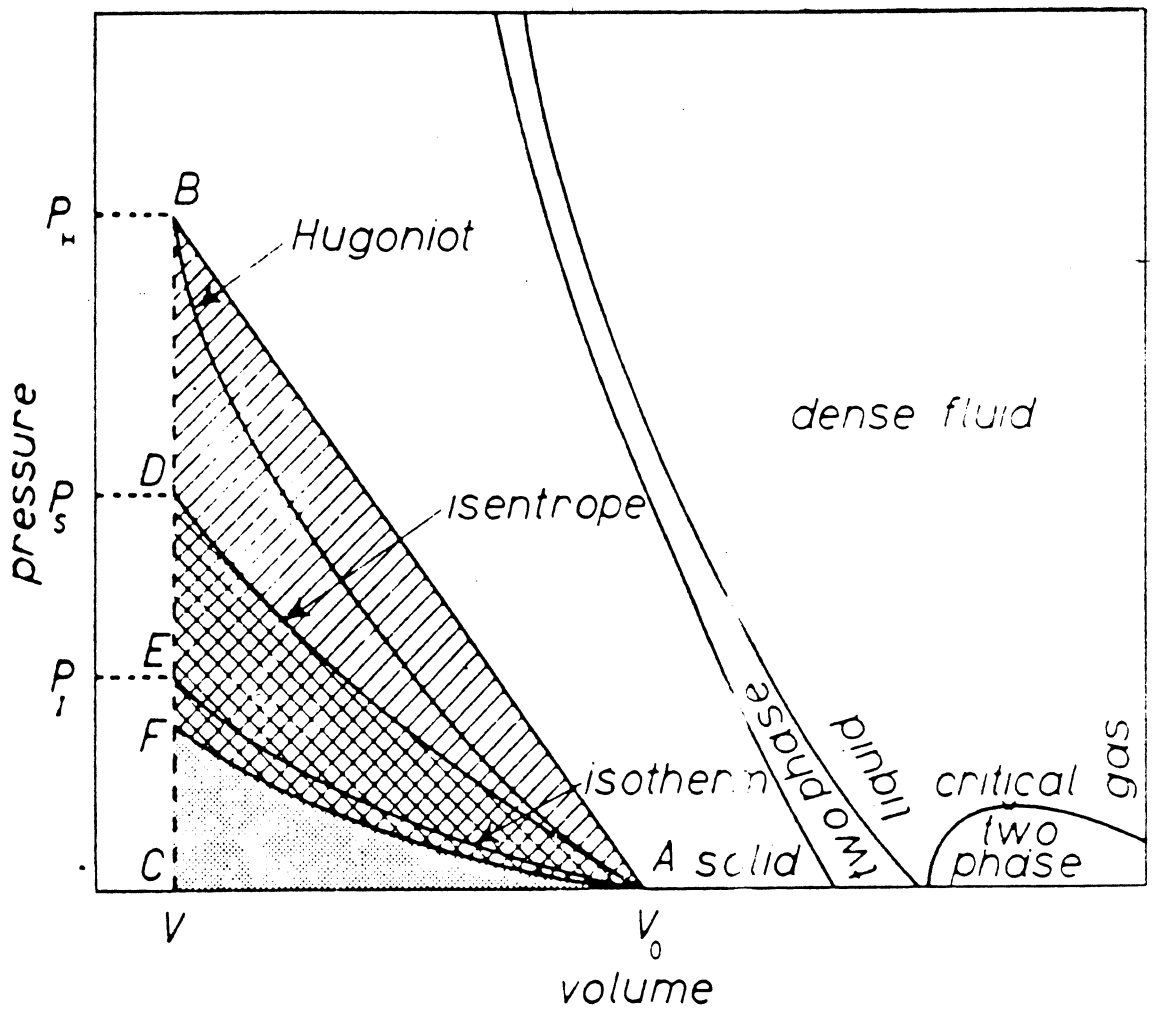

Figure 1: Pressure-Volume plane for a typical sample material [7].

states which can be reached by shocking a material from a given initial state. Hugoniot curve is a series of points for which the heat exchange between system and surroundings in going from the initial to the final state is zero, and for which the change in state is caused by the propagation of a one-dimensional steady-state discontinuous pressure disturbance.

The basic assumption invoked in writing the above equations, is that of steady state; that is, the shock profile is not changing with time. Thus the equations do not apply rigorously when shock formation or attenuation is occurring [8]. The former presents no problem experimentally because essentially instantaneous acceleration of one face of a solid slab is produced by detonation of an explosive in contact with the slab or by impacting the surface with a plate traveling at high velocity. A slow rate of acceleration would result in a profile which (in normal materials) steepens as it propagates to form a shock wave. In simple solids (that is, nonporous and no phase changes), shock attenuation as ordinarily observed is due to rarefaction waves generated at the free surfaces. These waves travel at local sound speed which exceeds the shock velocity, overtake the shock, and reduce the particle velocity and hence the stress. One can eliminate effects due to lateral boundaries by using specimens much wider than they are thick. In the case of

explosive detonated in contact with the solid, attenuation is always present due to the necessarily finite size of the explosive charge, but the rate is reduced by use of plane-wave initiation and large charges. Only in the case of a flying plate impacting a solid, essentially flat-topped specimen, the attenuation-free wave occurs, but this lasts only until the rarefaction from the rear face of the flying plate overtakes the shock.

3.2 Stress - Strain Relations

A state of stress is composed of a stress associated with a uniform hydrostatic pressure p (all three normal components equal) plus a stress tensor associated with the resistance of the material to shear distortion. The three normal components of stress that are assumed to describe the resistance of the material to shear distortion are called the deviatoric stresses [9], and can be defined as

$$\sigma_x^d = \sigma_x - (-p)$$
$$\sigma_y^d = \sigma_y - (-p)$$
$$\sigma_z^d = \sigma_z - (-p) \qquad \text{---- (8)}$$

the minus sign appearing in agreement with the convention that stresses are considered positive in tension, while pressure is considered positive in compression.

Since the shear strains are zero in one dimensional

motion, shear stresses will be zero. The stress components in the coordinate directions are σ_x, σ_y, σ_z. The hydrostatic pressure is defined as

$$(-p) = (\sigma_x + \sigma_y + \sigma_z) / 3 \qquad \text{---- (9)}$$

The compression of individual crystalline unit cells behind the shock front is a non-isotropic phenomena and is associated with the non isotropic stress existing behind the shock front [10]. This stress anisotropy, of course, results from the nonzero yield strengths of the material. In the simple elastic-plastic model, the difference between the longitudinal and transverse components of the stress is proportional to the yield strength of the material and is assumed to be constant at all pressures above yield point.

The most commonly employed geometry is that of one-dimensional strain, in which a plane wave propagates through a plate of large lateral extent. By symmetry, net strain can occur only in the direction of propagation of the wave, and the following relations exist

$$\sigma_x^d = (2/3)\ (\sigma_x - \sigma_y) = 2\ Y_o / 3 \qquad \text{---- (10)}$$

$$\sigma_y^d - \sigma_z^d = -\ (\sigma_x - \sigma_y) / 3 \qquad \text{---- (11)}$$

$$p = -\ (\sigma_x + 2\sigma_y) / 3 \qquad \text{---- (12)}$$

$$\tau = (\sigma_x - \sigma_y) / 2 \qquad \text{---- (13)}$$

At very high pressures, the strengths of materials are so low compared to the shock strengths that the nonisotropy of the stress is assumed negligible and hence shock and particle velocity measurements give directly the hydrostatic pressure p. However, at lower shock strengths (less than 100 Kbar), one must differentiate between the stress normal to the shock front and the hydrostatic pressure p [8].

3.3 Determination of Hugoniot Curve

It has been found that the Hugoniots of many materials can be adequately represented by a linear u_s-u_p relationship [11]

$$u_s = c_o + s\, u_p \qquad \text{---- (14)}$$

Departures from linearity can usually be traced to porosity, large elastic waves, or phase transitions. In a few cases a better representation can be obtained by including a quadratic term, $q.u_p^2$. However, if such a term is very large, the data should probably be reexamined with the possibility of one or more of the previously mentioned effects being present. The shock velocity is basically a very sensitive parameter, being in essence a differential measurement, equation (5). Thus a small change in slope in the u_s-u_p relation in some region could indicate the existence of a second-order transition, an effect quite difficult to observe in the p-v plane.

An additional argument for using equation (14) as a description of the shock wave equation of state is that the leading coefficient can be determined by direct measurements of the elastic wave velocities in an isotropic medium. Hence the zero particle velocity intercepts of the shock wave data can be compared with this quantity, or this important quantity can be used in fitting the data.

By using the linear u_s-u_p Hugoniot, the Hugoniot equation of state of many materials, centered at zero pressure, may be described by the three parameters ρ_o, c_o, and s. The shock wave locus can then be found for any other pair of variables by the use of equation (14) with the Rankine-Hugoniot equations. For this purpose it is useful to introduce the compression η, defined by

$$\eta = (v_o - v)/v_o = 1 - \rho_o v \qquad \text{---- (15)}$$

Combining this function with mass conservation, equation (2) yields

$$\eta = u_p / u_s \qquad \text{---- (16)}$$

The linear u_s-u_p Hugoniot, equation (14), then gives

$$u_p = c_o \eta / (1 - s\eta) \qquad \text{---- (17)}$$

$$u_s = c_o / (1 - s\eta) \qquad \text{---- (18)}$$

Conservation of momentum, equation (3), then yields a pressure-volume shock locus, or, equivalently, the following p-η relations

$$p_H = \rho_o c_o^2 \eta / (1 - s\eta)^2 \qquad \text{---- (19)}$$

$$dp_H/d\eta = \rho_o c_o^2 (1 + s\eta) / (1 - s\eta)^3 \qquad \text{---- (20)}$$

Here the subscript H denotes the conditions on Hugoniot curve. The derivative, equation (20) is necessary for calculating sound speeds and isentropes. The energy equation, with E_o set equal to zero, becomes

$$E_H = \eta P_H / 2 \rho_o \qquad \text{---- (21)}$$

3.4 Heating effects due to Shock

Consider a sample material, being shocked to some pressure p_H and then brought back to ambient pressure by rarefaction waves. This process is represented on a pressure-volume plot in figure 2. Each element of material starts off at some initial density ρ_o and is then compressed on the Hugoniot (points 1-2) to some pressure p_H by a shock wave. The material is then brought back to ambient conditions adiabatically (points 2-3) by rarefaction waves. The initial shocking process is a nonisentropic one, whereas the release process is isentropic [12]. Thus, the entropy of the material has

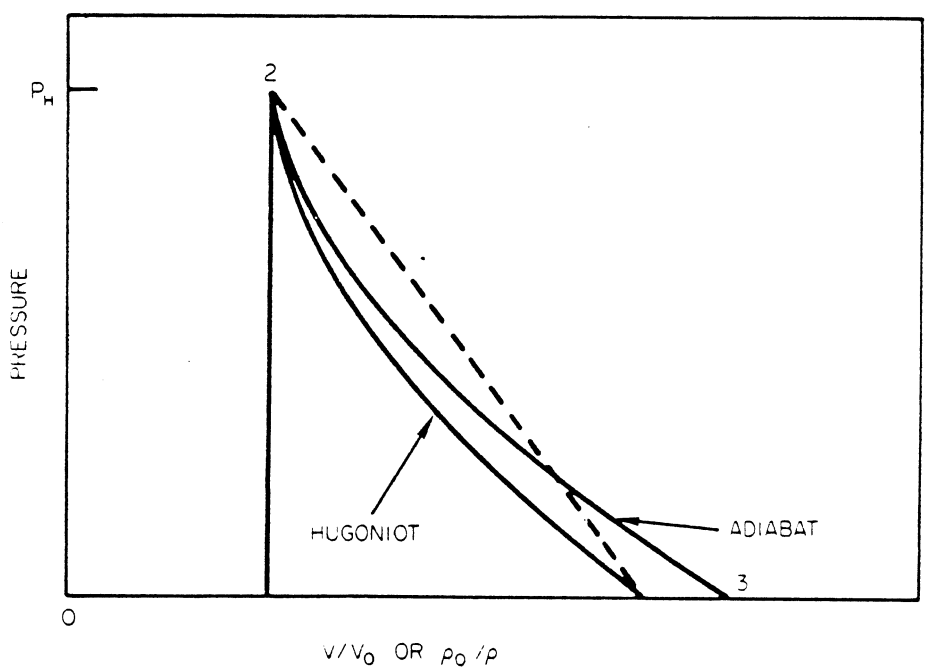

Figure 2: Pressure-volume curve, showing heating effects due to the passage of shock wave [12].

been increased by the impact process. In other words, the element of material in its final state will be heated. The specific internal energy E_H of the shock-compressed material is equal to the area of the dashed triangle in figure 2, whereas the energy that is returned by the material in pressure-volume work on expansion is the area under the adiabat. This latter area is less than the area under the triangle, and the difference between the two areas is proportional to the residual heat left in the element. Shocks of low strength will leave the material heated but in the solid state. As the shock strength is increased, the entropy excess increases rapidly and can lead to melting.

3.5 Concept of Shock Impedance

The concept of Shock Impedance (also called Dynamic Impedance) can be understood by observing the shock wave passage through the interface between different materials. In figure 3-a, a shock wave of pressure p_1 is progressing through material I. Upon impact with material II, shock waves of pressure p_2 are driven into material II and back into material I. When the second material has a lower dynamic impedance, as in figure 3-b, a rarefaction wave is propagated back into the first material, I, while a shock wave of reduced amplitude is driven into the second material, material III.

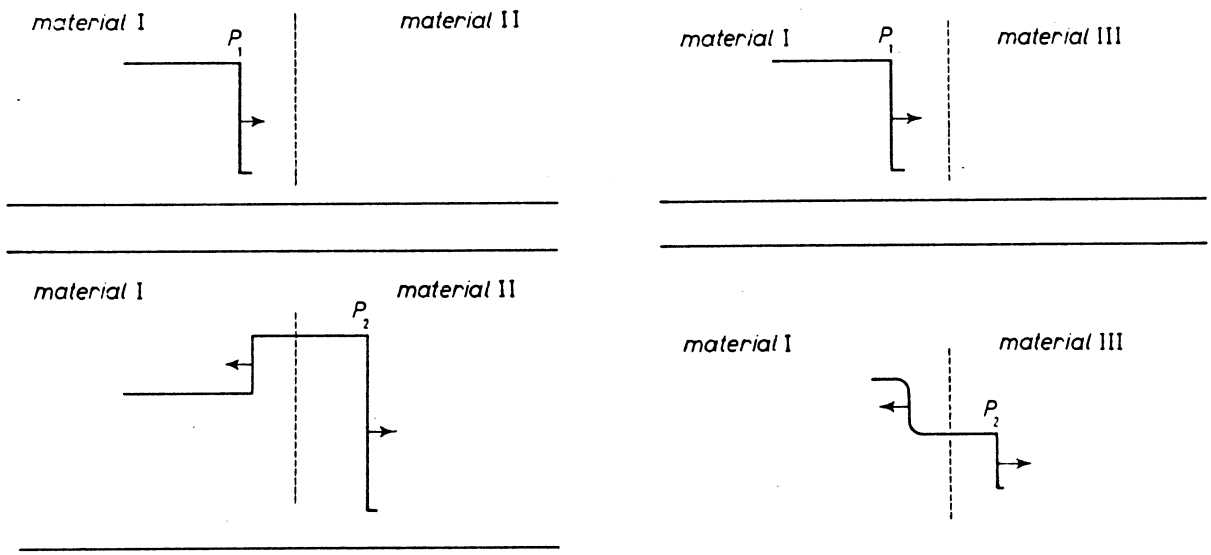

(a) (b)

Figure 3: a) Shock Wave into Higher Impedance material [7].
b) Shock Wave into Lower Impedance material [7].

The p-u_p co-ordinate system is convenient to represent the passage of a shock wave through an interface between materials of different shock impedance, since there must be a continuity of pressure, p, and particle velocity, u_p, across the interface. The question of whether a shock wave of higher pressure than the initial shock wave and rarefaction wave of lower pressure than the initial wave is propagated back from the interface is a question of the relative shock impedance of the materials. The shock impedance is defined as $\rho_o.u_s$, and is, in general, a function of pressure. In the limit of small amplitude waves, the shock impedance becomes equal to the acoustic impedance. Considering the momentum-conservation relationship, $p = \rho_o.u_s.u_p$, the shock impedance at a given pressure, on a p-u_p plot, is nothing more than the slope of the line connecting the origin and the particular pressure on the Hugoniot.

The pressure of the reflected shocks can be calculated from the following equation

$$p_2 = \frac{p_H - (\gamma/v)_2[(p_H - p_1)(v_o - v_2) / 2]}{1 - (\gamma/v)_2 (v_1 - v_2) / 2} \quad \text{---- (22)}$$

where subscript 2 refers to the second shock locus. Here p_H is the pressure on the original Hugoniot at the volume v_2. The point p_1, v_1 is the centering point for the second

shock and lies on the original Hugoniot, which is centered at zero pressure and the volume v_o. In the above equation γ is the Gruneisen parameters, given as

$$\gamma = v\,(\partial p / \partial E)_v \qquad \text{---- (23)}$$

Gruneisen parameter is a dimensionless number used to determine the response of materials to rapid heating at constant volume. Experimental determination of this parameter is discussed in detail in Ref [13]. It was found [14] that variations of 10 percent of γ produced only trivial changes in the calculated results. Thus for present applications γ is always considered to be independent of pressure and is usually determined from the relationship

$$\rho\gamma = \rho_o \gamma_o \qquad \text{---- (24)}$$

where zero subscripts refer to initial standard states. The Gruneisen ratio of the undisturbed state may be related thermodynamically to the volumetric thermal expansion coefficient α, the bulk sound speed C_o and the specific heat at constant pressure C_p by

$$\gamma_o = \alpha . C_o^2 / C_p$$

3.6 Attenuation of shock waves

The shock attenuation in plane waves is essentially due to two mechanisms: The irreversible heating of the material and the pressure reduction by rarefactions. In the case of spherical or cylindrical waves there is an additional pressure decrease due to the expansion of the wave. The irreversible heating E of the test material by the shock wave is given by

$$E = 0.5\ p\ (v_o - v) - \int_{v}^{v_o} (p(v)\ dv)_s = \underline{\text{const.}} \quad (25)$$

The integral in the above equation is taken along the isentrope from specific volume v_o to v. Figure 4 shows the attenuation of shock waves phenomena in different materials [15].

3.7 Splitting of Compression and Unloading Waves

Consider a constant compressive force with pressure p applied at an initial time to the end of a thin rod with a free lateral surface. A compression wave will travel through the body, with a propagation velocity, denoted by c_1. The material between the wave front and the end of the rod deforms and acquires a constant velocity u in the direction of axial force. The expression for the propagation speed of the compression wave (local speed of sound) will be

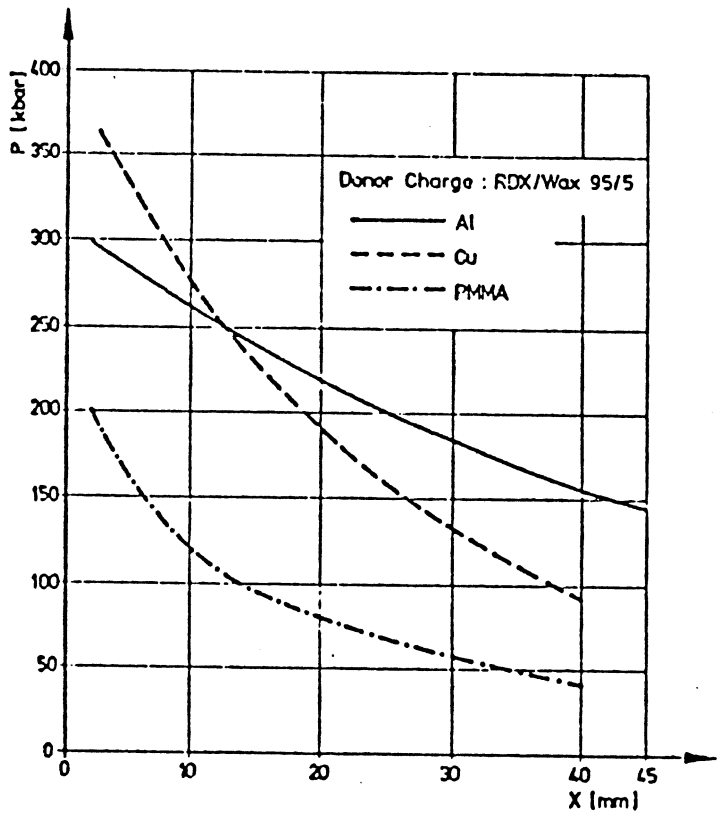

Figure 4: Pressure-Distance curves for different test materials [15].

$$c_1 = (E/\rho)^{1/2} \qquad \text{---- (26)}$$

When the compressive load is removed, a tensile or unloading wave is propagated at the same speed.

Now consider a laterally constrained rod such that the body is not deformed by the compression wave in the plane perpendicular to the direction of wave propagation. In this case the speed of sound will be

$$c_1 = (E'/\rho)^{1/2} = ((K + 4\,G / 3) / \rho)^{1/2} \text{ --- (27)}$$

where K and G represents the Bulk modulus and Shear modulus of the material respectively. The above equation gives the propagation speed of longitudinal waves in an infinite elastic medium. Actually, when a compression wave propagates through an infinite medium no displacements take place in the plane perpendicular to the direction of propagation, and the phenomenon takes place in the same manner as for a laterally constrained rod. The speed c_1 is always greater than the wave speed in the unconstrained rod, since $E' > E$.

The speed c_1 is the propagation speed only for sufficiently weak compression (and rarefaction) waves, in which the pressure is sufficiently small, less than the critical stress (this critical stress is also called

Hugoniot Elastic Limit, HEL, i.e. maximum stress a material can withstand under uniaxial shock compression without internal rearrangement). However, if the dynamic load is greater than critical, then the compressed solid, goes over to a plastic state, similar to that of a fluid. We know that the wave propagation speed is determined by the derivative of the pressure with respect to volume, in this case the normal stress w.r.t the volume. In the plastic state this derivative is proportional to the bulk modulus, and thus the propagation speed of sufficiently strong shock waves is determined only by the compressibility of the material, and is

$$c_o = (K / \rho)^{1/2} = (v / k)^{1/2} \qquad \text{---- (28)}$$

where k is compressibility of the material (Inverse of Bulk Modulus K). The speed c_1 is called the elastic wave speed, and the speed c_o the plastic wave speed. The quantity c_o is always less than c_1; for example, for iron c_1 = 6.8 km/sec and c_o = 5.7 km/sec. The propagation speed of strong shock waves depends on the wave strength. It is always greater than c_o or close to this value. The propagation speed of weak disturbances is always equal to c_1, and independent of the strength of shock. If the external pressure $p < p_{cr}$ then one elastic compression wave will propagate through the body with the speed c_1, as shown

in figure 5a. If, however, the applied pressure $p > p_{cr}$, then two waves travel through the body: One is an elastic wave with a strength p_{cr}, followed by a plastic wave, as shown in figure 5b. In the case of very strong shock wave (in the order of hundreds of thousands of atmospheres and higher) however, the effects of preliminary compression of the medium by the elastic wave to one or two thousand atmospheres and its acceleration to velocities of the order of several meters per second can be neglected and the plastic wave taken to propagate with respect to the undisturbed medium at rest with the speed c_o corresponding to the compressibility.

3.8 Weak Shock Waves

The pressure range of the order of several tens and hundreds of thousands of atmospheres is of great practical importance. These pressures are typical of those generated in detonating explosives and in explosions in water. In calculating flows with shock waves in the above pressure range we can, to a first approximation, neglect the entropy change across the shock wave and use the isentropic equation of state to relate the pressure and the density across the wave front. According to G.E.Duvall [16], when the condensed matter is compressed by shock waves to about 15 percent of its initial volume or less, the entropy change will be negligible and the shock can be treated as

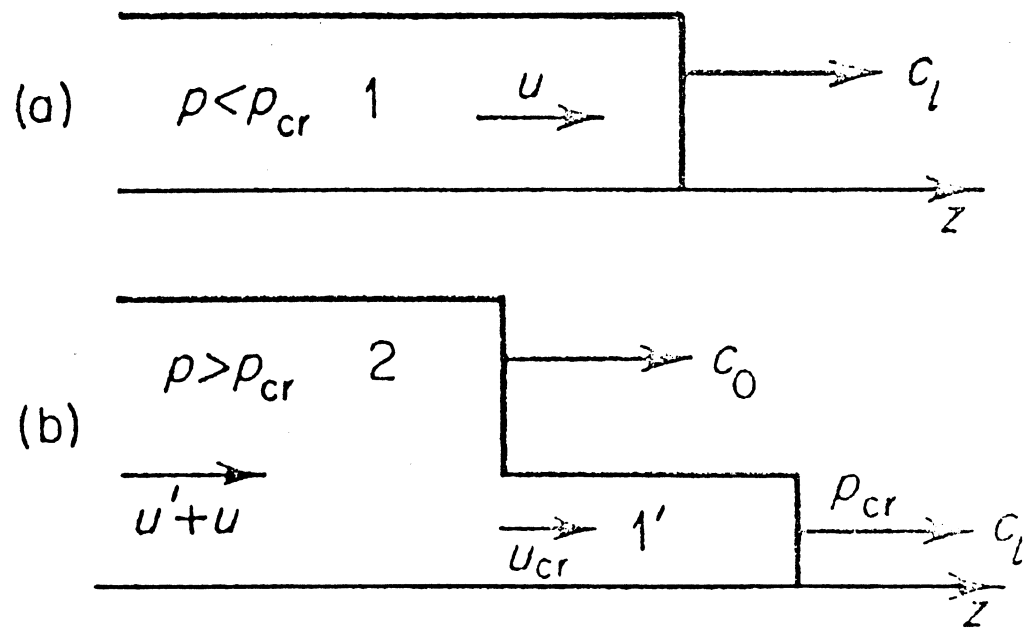

Figure 5: Two cases of Propagation of a Shock Wave [17]:
(a) One Elastic Wave.
(b) A system consisting of a plastic & an elastic wave.

an acoustic wave. Moreover, according to Zeldovich, Y.B. and Raizer, Y.P. [17], for pressures of about 10^5 atmospheres the isentropic approximation for the shock compression yields an error in the energy of not more than 5 percent (the error in pressure is even less). Thus, within the above mentioned pressure range, the shock wave can be considered as an acoustic wave.

CHAPTER 4

SELECTION OF PRESSURE SENSING ELEMENT

The primary objective of this development effort is to provide a system with an element and insulation which will produce the minimum perturbation of the shock. Ideally, the shock should not be altered at all in passing the transducer, and the transducer should provide an accurate pressure history under adverse noise conditions.

Gage design must be conducted with an awareness of two classic problems common to all free-field measurements: 1) assuring that the physical quantity to be measured is not significantly changed by the sensor, and 2) assuring that the transducer element responds only to the particular quantity of interest [18].

The range of in situ properties possible in stress experiments in geologic media vary widely as do the conditions of installation dictated by the experiment. To further complicate the problems, stress fields usually are significantly triaxial so that sensor elements must be isolated from several extraneous stress components. The measurement task may require the transient observation of mean stress or it may require recording one or more individual components of the stress tensor. This chapter

covers the general guide lines for the design of the pressure transducer (Sec. 4.1), concept of piezoelectricity (Sec. 4.2) and the comparison of PVF_2 film (selected as the pressure sensing material) to other commercially available piezoelectric materials (Sec. 4.3).

4.1 Guide Lines for the Design

Some common-place guidelines for the design of dynamic free-field pressure gages include the following

1. The presence of an inclusion such as a gage in a granular medium disrupts the stress field causing either stress concentration or stress relief depending on whether the inclusion is more or less stiff than the medium [19]. This stress mobilization has been termed soil-arching, further defined as passive-arching when the soil deforms more than the gage, and active-arching when the gage deforms more than the soil. Arching can seriously affect gage output; so, a gage that is to be placed in a soil mass ideally should have the same deformation characteristics as the soil it replaces. Hence the bulk density of the gage should approximate that of the surrounding medium.

2. Because a sensor which functions under shock-compression loading is destroyed in use [20], it require a high degree of reproducibility and repeatable calibration capability.

3. The gage should have good output signal levels in the stress region of 0 - 4 GPa.

4. The gage should have a small sensing element to approximate a point recording source. A small gage area is important to both rise time and, where the sample is of small diameter, total record time. Rise time becomes a function of gage area when the shock front is not planar with respect to the gage plane [21]. Accurate total record time becomes a function of gage area when the gage is large enough and/or the sample is small enough in diameter to allow the relief wave from the sample's edge to enter the gage element during the time of interest.

5. The gage must be thin enough to provide the desired rise time response. The rise time is a function of gage thickness as follows:

$$t_T = t_{in} + \text{Gage element thickness} / U_s$$

where,

t_T = minimum observable rise time from gage electrical output.

t_{in} = rise time of the pressure pulse moving into the front plane of the active element.

U_s = shock velocity in the gage element.

6. The gage should have the capability to record the stress history for long times, including release after the stress peak (of the order of micro seconds) [22].

7. The sensing element could be embedded in castable ceramics or epoxies.

8. The gage should be able to operate in a non-one-dimensional strain field.

No existing dynamic pressure measuring system has demonstrated the capability of meeting all the requirements listed above. Previous studies by Kawai [23], Murayama [24] and Bauer [25], [26], [27], [28], [29], determined that Piezoelectric PVF_2 film gauge is a likely candidate to fulfill the above mentioned requirements.

4.2 Concept of Piezoelectricity

4.2.1 General Definitions

It was first discovered by Pierre and Jacques Curie in 1880 that some crystals when compressed in particular directions show positive and negative charges on certain portions of their surfaces; the charges are proportional to the pressure and disappear when the pressure is withdrawn. This effect was observed in a number of crystals such as

zinc blende, sodium chlorate, boracite, tourmaline, quartz, calamine, topaz, tartaric acid, cane sugar and rochelle salt, and was called piezoelectricity.

Cady [30] defines Piezoelectricity as "Electric polarization produced by mechanical strain in crystals belonging to certain classes, the polarization being proportional to the strain and changing sign with it". It is clear that the reverse is also true. That is, an electrical polarization will induce a mechanical strain in piezoelectric crystals.

Pyroelectricity may be defined as "Electric polarization induced by thermal absorption in crystals, the polarization being proportional to the thermal change" [34]. The opposite effect, or the electrocaloric effect, is of minor importance. Vigot had pointed out that a distinction must be made between "true" pyroelectricity caused by a change in temperature alone and the "false" pyroelectricity that is due to the deformation which accompanies a change in temperature and which is therefore of piezoelectric origin.

The characteristic feature of ferroelectric crystals is the appearance of a spontaneous electric dipole moment which can be reversed, with no net change in magnitude, by an applied electric field. Because of this reversibility the ferroelectrics form a distinct subclass of the pyroelectrics [31]. Many ferroelectrics possess a

spontaneous dipole moment only in certain temperature ranges. At the boundaries of these ranges the crystal undergoes a phase transition to a non-pyroelectric phase. The phases with and without a spontaneous dipole moment are referred to as ferroelectric and paraelectric respectively. This phenomena of variation of charge with voltage across the ferroelectric material is called a Hysteresis Loop.

4.2.2 Crystal Cuts and their Properties

The ideal crystal consists of identical unit cells, each similarly situated with respect to its neighbors, to form a crystal lattice. The unit cell is the smallest parallelepiped, identical with all others in dimensions and atomic content, with which the crystal can be constructed.

All crystals belong to one of 32 point groups or symmetry elements. A crystal may be symmetrical with respect to a point, a line, a plane, or any combination of these. If symmetrical with respect to a point, the body is centrosymmetrical and can possess no polar properties; hence, no piezoelectric crystals are found in any of the 11 centrosymmetrical classes. With one exception, all classes devoid of a center of symmetry are piezoelectric. The single exception is Class 29, which, although without a center of symmetry, nevertheless has other symmetry elements that combine to exclude the piezoelectric property [30]. Out of the 20 piezoelectric crystals, 10 exhibit

both piezo- and pyroelectricity. Moreover, the existence of a polar axis in the crystal gives rise to an inherent spontaneous polarization. The spontaneous polarization of a crystal is present before any electric field has been applied.

Crystals are designated by the axis perpendicular to the largest face of the cut; they are further identified by the angular orientation of the length axis with respect to the other two axes. Thus a 45^{o} X-Cut represents a crystal with its thickness direction along the X axis, and its length axis 45^{o} between the other two axis; the output voltage is measured along the thickness direction.

Piezoelectric crystals are anisotopic in nature i.e. their electrical, mechanical and electromechanical properties differ for electrical or mechanical excitation along different directions. Thus for a systematic tabulation of piezoelectric properties following convention will be followed.

Numbered subscripts identify the vector and tensor directions. The first numerical subscript identifies the axis of polarization or applied electrical field; the second numerical subscript indicates the mechanical stress or strain axis. Positive mechanical action or reaction is defined as tensile, negative mechanical action as compressive. Positive electrical action or reaction causes an increase in the polarization and vice versa. For

example, d_{32} means the crystal is free to move in the (1) and (3) directions and a charge is developed in the surface of the film (3) for a change in stress in the transverse (2) direction. Alternatively, g_{31} is the applicable constant for mechanical stress (either tensile or compressive) applied in the (1) longitudinal direction resulting in an electrical field developed in the (3) direction.

One exception to the double numeric subscript system applies to hydrostatic forces in which the pressure field stress acts with equal amplitude on all surfaces of a crystal. Here, an (h) subscript is used for the hydrostatic condition

$$d_h = d_{31} + d_{32} + d_{33}$$

$$\& \quad g_h = g_{31} + g_{32} + g_{33} \qquad \text{---- (29)}$$

A second exception is the thickness mode strain constant d_t. The crystal in the thickness mode is clamped in the (1) and (2) directions. A charge is developed in the (3) direction in response to the change in stress in the (3) direction or, conversely, an electrical field applied in the (3) direction develops a stress in the (3) direction.

The electrical field output caused by an applied force (generator action) can be defined by

$$E = g_{ij}\,\sigma_j \qquad \text{---- (30)}$$

where σ is the applied mechanical stress, E is the resultant (induced) electrical field and g_{ij} is the

piezoelectric voltage constant. Alternatively, the deformation of a piezoelectric material caused by an applied electrical field (motor action) can be defined by the simple formula

$$S_j = d_{ij} E \qquad j = 1, 2, 3 \qquad \text{---- (31)}$$

where S_j represents the strain (relative deformation) of the body in the x_i direction at a certain electrical field strength (E), while d_{ij} is the piezoelectric strain constant.

Since piezoelectric materials interchange electrical and mechanical energy, the electrical properties depend on mechanical boundary conditions. When a piezoelectric element is completely free to vibrate, the dielectric constant, ϵ^X, is higher than when the element is mechanically restrained. Accordingly, superscripts are added to the symbol for dielectric constant to indicate the mechanical boundary conditions. Superscript X denotes a condition of constant stress (no mechanical restraint). Superscript S denotes a condition of constant strain (the material is completely restrained to prevent any mechanical deformation when the field is applied -- a condition that can be approached only under very special conditions). Thus, ϵ^X is the dielectric constant or permittivity under the condition of constant stress on the element, and ϵ^S is the dielectric constant or permittivity under constant strain.

$$\epsilon^S = \epsilon^X (1-k_{33}^2) \qquad \text{---- (32)}$$

Similarly, the mechanical (elastic) properties of a piezo element depend on the electrical boundary conditions. For example, when the electrode surfaces of a metallized Piezo Film element are connected together (short circuit E = 0), the element displays higher elastic compliance s than when the electrodes are not connected (open circuit). Thus, in defining elastic properties we must identify boundary conditions. Superscript E is used when the electrical field across the piezo film element is held constant (short circuit). Superscript D is used when the electrical charge density is held constant (open circuit).

Piezoelectric materials can be divided into following classes:

1. Natural crystals and synthetic crystalline materials.
2. Polarized ferroelectric ceramics.
3. Piezoelectric polymers.

The next three sections, contain a brief discussion of each class.

4.2.3 Natural Crystals & Synthetic Crystalline Materials

Quartz, rochelle salt and tourmaline are the earliest known highly polar natural piezoelectric crystals. Examples of synthetic crystalline materials are ammonium dihydrogen phosphate and lithium sulfate. In natural and synthetic crystalline materials, the relation between

applied stress and the generated charge depends on the symmetry of the crystal, the direction of the applied stress, and the location of the electrodes. For a long time, Quartz has been used successfully as a shock pressure sensing element.

4.2.4 Polarized Ferroelectric Ceramics

Recently, ceramics that have improved piezoelectric activity have been synthesized. Barium titanate ($BaTiO_3$) and lead zirconate titanate (PZT) are in common use. These ceramics are polycrystalline in nature. The individual crystallites possess polar axes which are randomly aligned with respect to each other. Therefore the ceramics do not have piezoelectric properties in their original state. Piezoelectric behavior is induced in these materials by polarizing treatment (poling) which aligns the polar axes of the individual crystallites. This process is sometimes carried out by raising the temperature of the ceramic above its Curie temperature (the temperature above which the material loses its ferroelectric properties), applying a biasing voltage, and then cooling the ceramic slowly under the influence of the bias. For PZT, bias voltages usually are between 30,000 volts/in. and 100,000 volts/in. of thickness [32].

In the polarized ferroelectric ceramics, the relationship between the applied stress and the generated

charge depends on the direction and magnitude of the induced polarization, the direction of the applied stress, and the location of the electrodes.

Because of their higher dielectric constant and greater sensitivity, polarized ferroelectric ceramics usually can be used to measure smaller stresses extending over a longer time than piezoelectric crystals such as quartz. This factor, together with the ease of fabrication and the lower cost, makes such materials particularly useful. These materials suffer from the disadvantage that their sensitivities change appreciably with time as a result of aging, and from the fact that very large stresses and high temperatures may cause them to become depolarized. Since ceramics donot give reproducible results under all circumstances, ceramic based sensors cannot be classed as primary standard.

4.2.5 Piezoelectric Polymers

Naturally occurring materials such as wood and other biological substances were the first piezoelectric polymers to be investigated. Fukada [33] studied a number of these materials. Kocharyan in 1967 investigated a number of polar and non-polar polymers subjected to a high poling voltage and a high frequency field, and discovered that the higher the polarity of the unit cell of the polymer the higher the "induced" piezoelectric effect. They discovered

that polytrifluoroethylene (PVF_3), plasticized polyvinyl chloride (PVC), and rigid polyvinyl chloride had the highest piezo activity. In 1969, Kawai [23] discovered that polyvinylidene fluoride (PVDF) could be poled to a level of activity not previously obtained with any other polymeric material. Of all known polymers, those based on vinylidene fluoride show the highest piezo- and pyroelectric activities.

Natural Crystals and Ceramics, which are discussed above, generally are dense, brittle, stiff, difficult to produce in large sizes and impractical to fabricate into complex shapes, while the polymeric piezoelectric materials are pliant, flexible, tough, light weight and cheap.

4.3 Characteristics of PVDF film

Polyvinylidene Fluoride also called PVF_2 or PVDF is a semi-crystalline high molecular-weight polymer of monomer (CH_2 - CF_2) whose structure is essentially head-to-tail (i.e. CH_2 - CF_2 - $(CH_2$ - $CF_2)_n$ - CH_2 - CF_2). PVDF is approximately 50 percent crystalline and 50 percent amorphous. Some years ago Kureha Chemical Company was the only firm to produce these polymers. Pennwalt Corporation, Rhone Poulenc, and Thomson Lcr, France, are presently engaged in producing piezoelectric PVF_2 polymers of high quality.

4.3.1 Crystal Structure of PVDF

PVDF exhibits at least three crystal forms; α, β and γ forms. The α form is found mainly in melt cast PVDF. The β form crystals appears in oriented PVDF; the amount of β form crystals depends mainly on stretching conditions. The molecule in the β form crystal are in a planar zigzag conformation, and the unit cell is orthorhombic (Crystal Class C_{2v}) and there are two polymer chains per unit cell. The β form crystal show a high piezoelectric effect without any polarizing procedures, and is as stable as α form crystal. The form chain has a small dipole moment, but the overall dipole moment in a unit cell is zero. The γ form crystals are very similar to the β form crystals.

PVDF samples obtained from the melt usually exhibit α form. But samples which are grown under high pressure or precipitated from some specific solvents can exhibit β or γ form. The α form makes a transition to β form when it is stretched at low temperatures (usually below 100° C) or heat-treated under high pressures. The copolymer of vinylidene fluoride with vinyl fluoride, trifluoroethylene, or/and tetrafluoroethylene is apt to become β form.

The PVDF crystals possess a Orthorhombic class mm2 symmetry. According to the Voigt classification, these crystals are called Hemimorphic and according to the Miers classification, they are called Diagonal Polar. The piezoelectric constants matrix for these crystals is given

as

$$[d] = \begin{bmatrix} 0 & 0 & 0 & 0 & d_{15} & 0 \\ 0 & 0 & 0 & d_{24} & 0 & 0 \\ d_{31} & d_{32} & d_{33} & 0 & 0 & 0 \end{bmatrix}$$

A material can have atmost 21 independent elastic coefficients. However, only in the crystal class of lowest symmetry do all 21 elastic coefficients have values differing from zero. The number decreases with ascending symmetry, becoming 3 for cubic crystals, 2 for isotropic solids and 1 for fluids. Since PVDF crystals have a orthotropic character (material symmetry w.r.t two orthogonal planes) with respect to their elastic properties, they have nine independent elastic coefficients given as

$$[C] = \begin{bmatrix} c_{11} & c_{12} & c_{13} & 0 & 0 & 0 \\ c_{12} & c_{22} & c_{23} & 0 & 0 & 0 \\ c_{13} & c_{23} & c_{33} & 0 & 0 & 0 \\ 0 & 0 & 0 & c_{44} & 0 & 0 \\ 0 & 0 & 0 & 0 & c_{55} & 0 \\ 0 & 0 & 0 & 0 & 0 & c_{66} \end{bmatrix}$$

where $\{\sigma\} = [C]\{S\}$

4.3.2 Fabrication of PVDF piezo film

There are many reported investigations on the piezoelectricity of PVDF, but the results are not always consistent. This discrepancy is likely because piezo film is commercially available from many different sources which may use different production processes. From an extensive research program, F. Bauer [25] has developed a detailed understanding of the procedures required to produce a highly reproducible material. This patented Bauer process, described below, is the only known method which achives such high degree of polarization in a reproducible manner.

The PVDF film is prepared from solution or dispersion casting or melt extrusion. The Piezo film is then extruded into sheets of selected thickness. When PVDF is initially extruded, the non-piezo, non-polar α - crystallite phase predominates. Orientation of the polymer chains in the plane of the film is necessary to attain enhanced piezoelectricity. Orientation is accomplished by stretching along one face dimension (uniaxially), usually in the direction of the machine travel or in both machine and transverse directions (biaxially).

Mechanical orientation of the film at elevated temperatures causes partial transformation to the piezoelectric polar phase and orients the polymer chains in the direction of stretch.

Film for poling is usually coated on one or both sides

with aluminum, chromium, nickel, silver or another electrode metal to provide an intimate electrical contact with the PVDF film during the polarization as well as in subsequent use. The coatings (electrodes) are applied by vacuum deposition.

The polarization (poling) process subjects the PVDF film to an intense electrical field at elevated temperature followed by cooling within the applied field. This process aligns the polar β phase crystallites normal to the stretched alignment of the polymeric chains along the thickness direction. The fields also partially convert the non-polar α form to a polar α and polar β form.

During the poling process, the sample is placed between spherical electrodes in a dielectric liquid. A novel experimental arrangement is used to measure the polarization of the material directly (figure 6). A sine high voltage signal is applied to the specimen at a very low frequency 0.1 Hz and the current traversing the PVF_2 sample is measured. Since D is equal to $\epsilon E + P$, the current i passing through the polar dielectric is given by

$$i = i_D + i_R = \frac{dE}{dt} + \frac{dP}{dt} + \frac{E}{R} \qquad \text{---- (33)}$$

where,

i_D : Displacement Current

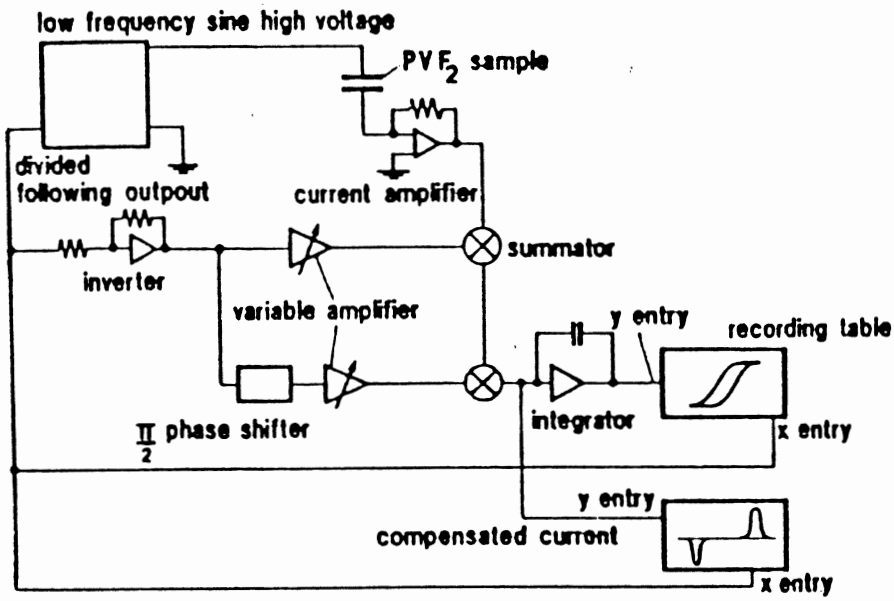

Figure 6: Schematic Diagram showing the Cycling Hysteresis Device [28].

i_R : Current into the resistance R

D : Electric Induction

P : Polarization of the material

R : Internal resistance of the material

E : Applied Field Strength

ϵ : Permittivity of the material per electric field

The resistive component (E/R) as well as the capacitive component (dE/dt) are subtracted from the measured i. Thus a cycle for i such that (i=dp/dt) is obtained. By integrating the current, the curve, which indicates the total polarization, appears as a hysteresis loop. Typical experimental results for a biaxially oriented sample are shown in figure 7. The hysteresis loop is traversed many times at room temperature in order to drain the ions and local space charges. PVF_2 showing this hysteresis loop is therefore "ferroelectric". The remanent polarization attains approximately 10 $\mu c/cm^2$ in the samples of 23 μm. The polarization of the material is stable between -40°C and +80°C. It has been verified by F. Bauer that the coefficient d_{33} is proportional to the remanent polarization (figure 8). Reproducible d_{33} values of PVF_2 samples can be obtained with this poling process. The maximum values of d_{33} are obtained for an electric field which is just below the value of dielectric breakdown.

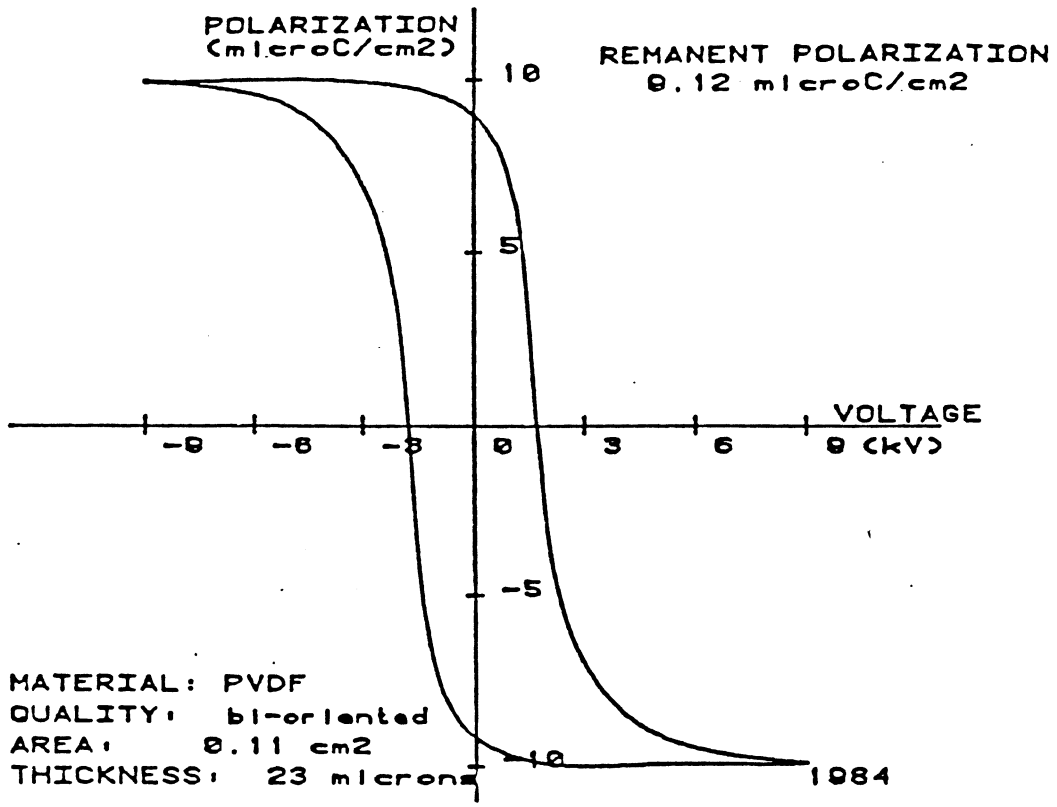

Figure 7: Hysteresis curve for Biaxially stretched PVF_2 [25].

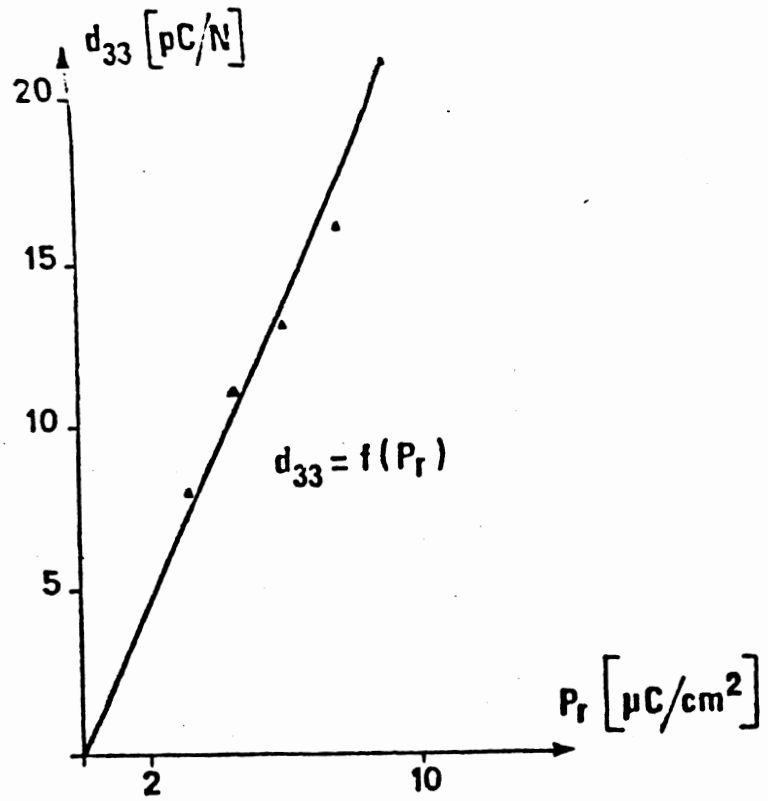

Figure 8: d_{33} versus remanent polarization P_r [25].

4.3.3 General Properties of PVDF film

PVDF material is tough, lightweight, transparent and flexible. It is readily maunfactured in sheet form in a continuous roll process and can be fabricated into complex shapes for specific applications. Piezoelectric cable, for example, has been maunfactured for hydrophone and geophysical transducer applications. PVDF film is compliant, and can be readily adhered to supporting structures of complex geometry or suspended as a membrane in a predetermined shape. The rigidity of ceramics is great compared to polymers and is an advantage in converting from electrical energy to mechanical vibration. But ceramics are also brittle and stiff and therefore difficult to produce with large areas and impractical to fabricate into complex shapes. Piezo film is more sensitive than Quartz and far more sensitive than ceramic as a transformer of mechanical to electrical energy. Temperature dependence and aging characteristics of Piezo film are important design parameters that have been extensively studied. Piezo film activity decay is proportional to working temperature. There is no substantial decay in activity up to a working temperature of 70^{o}C, and remarkably high activity (50 percent of initial value) is maintained at a temperature of 110^{o}C. A comparision of properties of PVDF film and other piezoelectric materials is given in Table 1. The detailed

Material	Cut	Density [Kg/m^3]	Acoustic Impedance [Kg/m^2-s] $*10^6$	K	Elastic Coeff. [N/m^2] $*10^9$	Relative Dielectr. Constant ϵ/ϵ_o***	Piezo. Constant [C/N] $*10^{-12}$	Ref
Quartz	X	2650	14.4	0.1	85	4.5	6.5	33
Rochelle Salt	45X	1770	5.7	0.73*	16**	350	275+	33
PVDF	Z	1780	2.7	0.12*	3**	12	23	34
$BaTiO_3$	Z	5500	23	0.45*	100**	1500	78+	33
Collagen	45	1200	1.5	0.14	2	8	8	33
PMG	45	1300	1.6	0.25	2	4	10	33
PZT	Z	7500	30.0	0.3	83.3	1200	110	34
$LiNbO_3$	Z	4640	31.72++	--	203	30+++	-0.2+	18

* : K_{31}
** : G_{11} measured in Short Circuit Mode
*** : ϵ_o (Permittivity of free spaca) = $8.854*10^{-12}$ F/m
\+ : d_{31}
++ : Sound Speed measured in "2" direction
+++ : measured in 33 direction @ constant stress

LIST OF SYMBOLS USED:

K : Electro-Mechanical Coupling Constant
PVDF : Polyvinylidene Fluoride
$BaTiO_3$: Barium Titanate
PMG : Poly Methyl Glutamate
PZT : Lead Zirconate Titanate
$LiNbO_3$: Lithium Niobate

Table 1: Comparision of PVDF film and other piezoelectric materials.

properties of Kynar Piezo film can be found in Referance [34].

4.3.4 Shock Response of PVDF Film

The behavior of shock loaded PVF_2 has been the subject of extensive investigations, especially at Institut Franco-Allemand de Saint-Louis (ISL), France. Figures 9 and 10 are examples of current-time records at 2.44 Kbar and 120 Kbar. It is obvious from the figures that the electrical charge output of PVF_2 describes the shock profile. PVF_2 is piezoelectric in the 0 - 120 Kbar range with no apparent hysteresis upon unloading.

LASL shock wave data is being used to determine the hugoniot curve for the PVDF film. Appendix A contains this data along with a figure showing the shock wave velocity v/s the particle velocity. By using a linear curve fit, the following expression is obtained

$$U_s = 2.6002 + 1.507447\ U_p$$

U_s = Shock wave velocity (km/sec)

U_p = Particle velocity (km/sec)

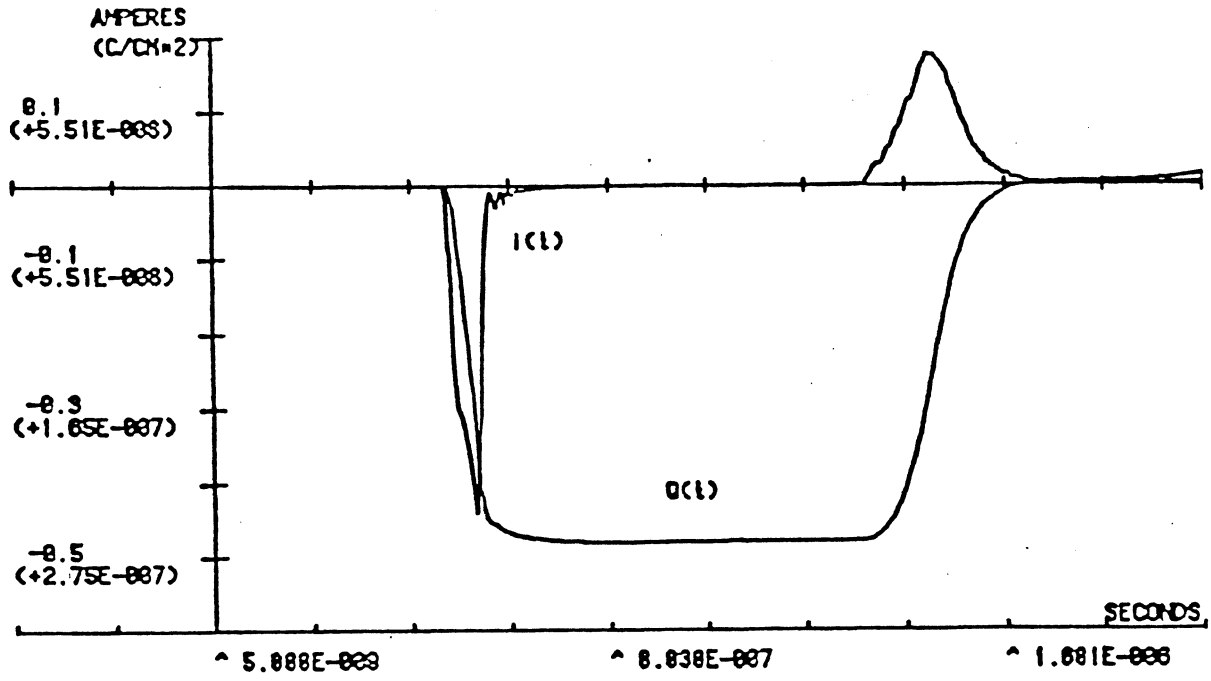

Figure 9: Step Shock Compression, PVF_2 35 micrometer, Target PMMA (2.44 Kbar) [25].

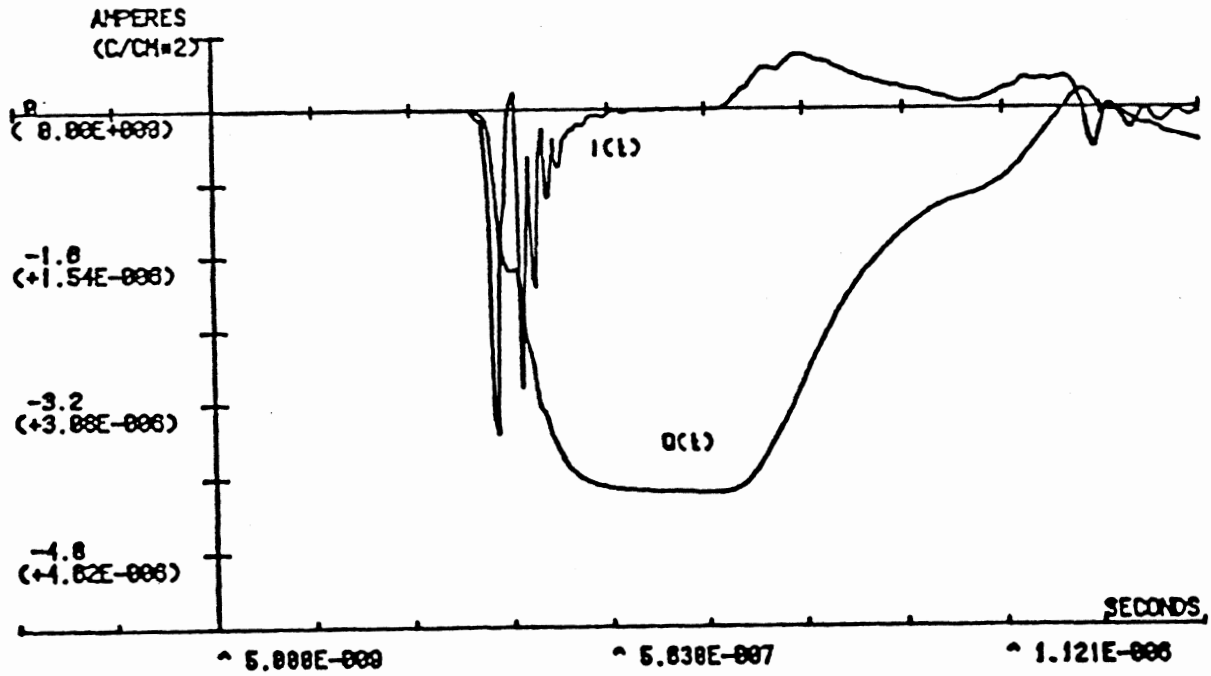

Figure 10: Step Shock Compression, PVF_2 35 micrometer, Target copper (120 Kbar) [[25].

CHAPTER 5

SELECTION OF THE POTTING MATERIAL

Piezoelectric materials have been proved to be an effective and accurate means of measuring pressure-time histories to levels above 300 Kilobars when they are imbedded in a potting material with known shock characteristics.

Ideally, the potting material used with the piezoelectric sensing material should have a matched mechanical impedance, and perhaps with time a class of materials allowing a reasonable match will be perfected. For the present, efforts are directed towards a material which will provide satisfactory insulation and has well defined shock characteristics. In the past, various epoxies have been used successfully for potting or encapsulation purposes. We have selected a mixture of Epon-828 resin and Z-hardner as the potting material for the pressure transducer. This epoxy has been used with success in a carbon piezoresistive stress gauge developed by Williams [21]. The response of the epoxy to acoustic waves is known [35], [36] and Drumheller [37] has used this epoxy to model a system of small solid aluminum oxide particles dispersed in a continuous epoxy matrix material.

This chapter covers the general guide lines for the

selection of the potting material (Sec. 5.1) and characteristics of the Epon-828 epoxy which is selected as the potting material. The constitutive modeling of the Epon 828-Z mixture will be discussed in Chapter 7.

5.1 Guide lines for the Selection

1. A shock impedance difference between the potting epoxy and the sensing element can cause a difference in particle velocities under shock loading and possibly result in relative motion between the leads and the sensing element, as observed by Keough [38]. Thus the shock impedance difference between the constituents of the pressure transducer should be minimized.
2. The temperature coefficients of expansion of the constituents of the transducer should be carefully matched because mismatching can cause fractures during the inadvertent temperature cycling of the assemblies.
3. The curing temperature of the potting material should be lower than the curie point of the piezoelectric sensing element.
4. The adhesion characteristics of the potting material should be good, in order to ensure a perfect bond between the constituents of the transducer.
5. Since the pressure transducer will be subjected to temperatures of about 6000^{o}F for about two microseconds, the thermal conductivity of the epoxy should be low

enough to keep the temperature of the sensing element below 250°F.

5.2 Characteristics of the EPON 828-Z mixture

Epon 828 is a reactive, light colored liquid epoxy resin produced by Shell Chemical Company [39]. It is a condensation product of epichlorohydrin and bisphenol-A, with no diluents. Epoxide equivalents are controlled to give 183-195 g of resin per gram atom of the epoxy group. This polymer is cured with hardening agent Z, an aromatic eutectic mixture of methylene dianaline, metaphenylenediamine (MPDA), and phenyl glycidyl ether. Z hardner is used for applications which require excellent chemical and solvent resistance as well as high deflection temperatures. The resin-hardner mixture is cured for 4 hour at room temperature, followed by 4 hour at 55°C, and 16 hour at 93°C. Specimens are molded to the desired size in cylindrical containers and then are machined to the desired thicknesses.

5.2.1 Mechanical Properties

High performance, high strength composites are obtained when Epon 828 resin is cured with a variety of curing agents. Unfilled composites in common use have tensile values greater than 10,000 psi with modulus values greater than 400,000 psi. Such composites are normally

very rigid. If greater flexibility is needed, composites can be formulated to give up to 300 percent elongation.

5.2.2 Adhesive Properties

One of the most widely recognized properties of cured Epon resin 828 is excellent adhesion to a broad range of substrates. Such composites exhibit shear strength of up to 6,000 psi. One factor which contributes to this property is the low shrinkage shown by these composites during cure. Compared to other polymers, these epoxy resins have low internal stresses which results in strong and durable finished products.

5.2.3 Electrical Properties

Epon resin 828 composites have excellent electrical insulating characteristics and dielectric properties. For example, composites can be obtained having volume resistivities up to $1*10^{16}$ ohm-cm and relative capacity or relative dielectric constant of 3-5 at ambient conditions.

5.2.4 Shock Response

Selection of the proper epoxy shock response is quite difficult because epoxy often exhibits instantaneous and equilibrium responses, and the response is related to the time frame of the experiment. The equilibrium Hugoniot equation for the Epon 828-Z is given as follows [40]

$U_S = 2.64 + 1.66\ U_p$ km/sec

Density = 1200 kg/m^3

Some other properties are as follows:

Longitudinal Acoustic Velocity	: 2.64 km/sec	[40]
Shear Acoustic Velocity	: 1.21 km/sec	[40]
Bulk Acoustic Velocity	: 2.24 km/sec	[40]
Bulk Modulus, K	: 6.02 GPa	[40]
Specific Heat	: 0.5 Cal/g/^oC	[39]
Poisson Ratio	: 0.385	[36]
Specific Gravity @ 20^oC	: 1.16	[39]
Viscosity, @ 25^oC	: 110-150 poise	[39]
Pounds/gallon, 20^oC	: 9.7	[39]
Refractive Index, 25^oC	: 1.573	[39]

CHAPTER 6

HEAT TRANSFER ANALYSIS OF THE SENSOR

Since the pressure transducer will be subjected to a temperature of more than 6000 ^{o}F for approximately two microseconds, it is important to determine the transient temperature distribution inside the transducer immediately after the occurrence of the blast. The importance of this analysis is increased by the fact that the operational temperature for the piezo film, being used as a sensing element is only 176 - 248 ^{o}F. Thus the transient temperature distribution must be understood sufficiently well to guide material selection for the insulating material around the piezo film sensing element. The considerations may relate to the temperature limitations of materials, to heat-transfer characteristics, or to the thermal stressing of materials which accompanies changing temperature distributions. Moreover, since we know from Chapter 3 that the temperature rise due to the shocks, generated by the detonating explosives will be negligible , we are neglecting that factor during the analysis.

The solution of unsteady-state problems is in general more difficult than the solution of steady-state problems because of the additional independent variable, time. The temperature is a function of position in the

conduction region, but, in addition, this distribution changes with time. If this change in temperature is periodic, the process is called periodic. Nonperiodic processes are called transients.

The solution is approached by stating the boundary conditions (which may be time-dependent) and the simplest form of differential equation applicable. In addition, in a transient process the initial temperature distribution throughout the conduction region must be given. The problem then amounts to finding how this distribution changes with time.

The general three dimensional heat conduction equation in cartesian coordinates is

$$\frac{\partial^2 t}{\partial x^2} + \frac{\partial^2 t}{\partial y^2} + \frac{\partial^2 t}{\partial z^2} + \frac{\dot{q}}{k} = \frac{\dot{\partial t}}{\alpha . \partial \tau} \qquad \text{---- (34)}$$

Since there are no heat sources, $(\dot{q}/k)$ becomes zero and equation (34) becomes

$$\frac{\partial^2 t}{\partial x^2} + \frac{\partial^2 t}{\partial y^2} + \frac{\partial^2 t}{\partial z^2} = \frac{\partial t}{\alpha . \partial \tau} \qquad \text{---- (35)}$$

Since the temperatures does not vary in the Y or Z direction, $(\partial^2 t/\partial y^2)$ and $(\partial^2 t/\partial z^2)$ becomes zero and equation (35) can be written as

$$\frac{\partial^2 t}{\partial x^2} = \frac{\partial t}{\alpha . \partial \tau} \qquad \text{---- (36)}$$

This is called the heat diffusion equation, in cartesian coordinates.

6.1 Analytical Solution to the Heat Diffusion Equation

Description of any heat transfer problem includes a specification of boundary conditions and an initial condition, usually in the form of a specified temperature distribution at some particular time. The solution to a particular problem is a function of x and may, in general, be written as

$$t = f(x,\tau) = X(x)*F(\tau) \qquad \text{---- (37)}$$

Substituting equation (37) into equation (36), give

$$F.X'' = \frac{X.F'}{\alpha} \qquad \text{or} \qquad \frac{X''}{X} = \frac{F'}{\alpha . F}$$

As a result of the definitions of X and F, the left-hand side may be a function only of τ. Since x and τ are independent, neither side is a function of x or τ and, therefore, both sides are equal to a constant λ^2 or $-\lambda^2$:

$$X'' = \pm \lambda^2 . X$$

$$F = \pm \alpha . \lambda^2 . F$$

The solutions of these equations are

$$\text{For } +\lambda^2: \quad X = C_1 . e^{\lambda x} + C_2 . e^{-\lambda x} \qquad \text{---- (38)}$$

$$\text{For } -\lambda^2: \quad X = C_3 . e^{i\lambda x} + C_4 . e^{-i\lambda x}$$

$$= C_3 . \text{Cos}\, \lambda x + C_4 . \text{Sin}\, \lambda x \qquad \text{---- (39)}$$

$$\text{For } \pm\lambda^2: \quad F = C_5 . e^{\pm \alpha \lambda^2 \tau} \qquad \text{---- (40)}$$

The above forms anticipate the various types of problems which may be encountered. The separation constant λ^2 may be real, imaginary, or complex. The choice is based upon the conditions to be satisfied in a given problem. For λ^2 real, the x dependence is either exponential $(+\lambda^2)$ or periodic $(-\lambda^2)$, the latter permits an infinite-series expansion of an initial condition. The accompanying τ dependence is an exponential growth or decay of the temperature field. For λ^2 imaginary, the time dependence is purely periodic, and the x dependence for this choice results in combined periodic and exponential behavior in x. For λ^2 complex, the τ- and x-dependent behaviors are each a combination of exponential and periodic effects.

Now, consider a plate of thickness L which is assumed of infinite extent, in order to make the process one-dimensional. The plate has an initial temperature distribution of $t_i = F(x)$ (see figure 11). At $\tau = 0$, the temperature of the two surfaces are changed to t_o. Now, the subsequent distribution in the plate as a function of

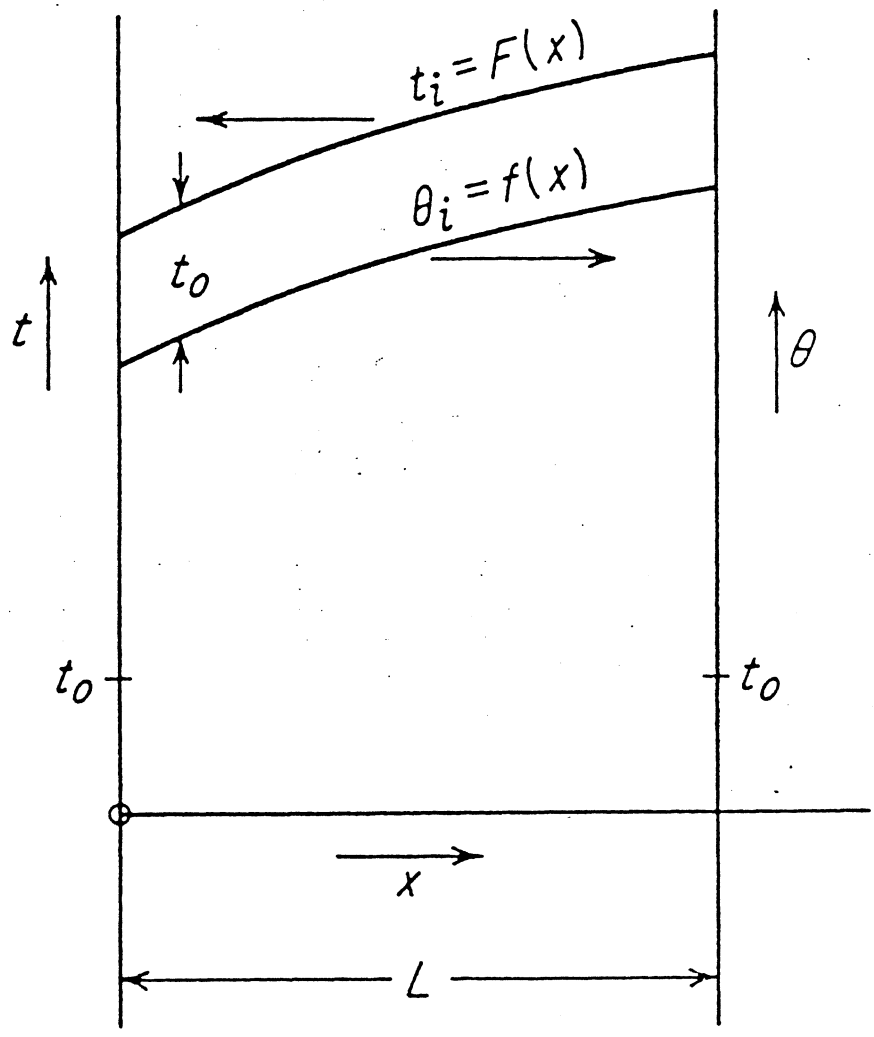

Figure 11: Transient conduction in a plate [41].

time is required. In order to simplify the analysis, the problem is stated and solved in terms of temperature excess θ. The local temperature excess is the amount by which the local temperature differs from t_o. The problem statement is

$$\frac{\partial^2\theta}{\partial x^2} = \frac{\partial\theta}{\alpha.\partial\tau}$$

At $\tau = 0$: $\theta_i = F(x) - t_o = f(x)$ for $0 \leq x \leq L$

For $\tau > 0$: $\theta = 0$ at $x = 0$ and $x = L$

Since the temperature variation with time is not periodic, the separation variable λ^2 is a real number. Since the temperature decays with time, the exponent of e in equation (40) must be negative. Therefore, equation (39) is used for X, and the following is a solution:

$$\theta = C_5.e^{-\alpha\lambda^2\tau}(C_3.\text{Cos}\lambda x + C_4.\text{Sin}\lambda x) \qquad \text{---- (41)}$$

Since $\theta = 0$ at $x = 0$ for all $\tau > 0$, C_3 must be zero. Similarly, $C_4.\text{Sin}\,\lambda x$ must be zero at $x = L$ for all $\tau > 0$. Since C_4 can not be zero, $\sin\lambda L$ must be zero. This occurs for $\lambda L = n\pi$, where n is any integer. The solution, then, is the sum of all particular solutions:

$$\theta = \sum_{n=1,2}^{\infty} C_n.e^{-(n\pi/L)^2\alpha\tau}.\text{Sin}\,(nx\pi/L) \qquad \text{---- (42)}$$

The initial condition (at $\tau = 0$) determines the C_n:

$$\theta_i = f(x) = \sum_{n=1,2}^{\infty} C_n . \text{Sin}\ (nx\pi/L)$$

This is a Fourier sine series expansion of f(x). The coefficients are given by

$$C_n = \frac{2}{L}\int_0^L f(x') . \text{Sin}(n\pi/L) . x' . dx' \qquad \text{---- (43)}$$

Equations (42) and (43) constitute a solution of the problem when f(x) is specified. If the initial temperature excess distribution is uniform and equal to θ_i, the constants are evaluated as

$$C_n = \frac{2\theta_i}{L}\int_0^L \text{Sin}(n\pi/L) . x' . dx' = 0 \quad \text{for } n = 0,2,4,\ldots$$

$$= \frac{4\theta_i}{n\pi} \quad \text{for } n = 1,3,5,\ldots$$

The solution is

$$\frac{\theta}{\theta_i} = \frac{4}{\pi} \sum_{n=1,3}^{\infty} \frac{e^{-(n\pi/L)^2 \alpha \tau}}{n} . \text{Sin}\ \frac{n\pi}{L} x \qquad \text{---- (44)}$$

6.2 Numerical Solution to the Heat Diffusion Equation

An analytical solution of the above parabolic equation may be obtained by employing methods such as separation of variables and Laplace transforms. However, for complex boundary conditions and arbitrary initial temperature

distributions, such analytical solutions become very involved and numerical methods are much more convenient.

The solution to equation (36) can be obtained for increasing time. It requires the specification of two boundary conditions in x and an initial condition, which is the temperature distribution at a given time. Starting with the given initial temperature distribution, the temperatures are obtained at the next time step. The results thus obtained are then used to evaluate the temperatures at the end of the second time step. Thus, the solution proceeds for increasing time until results are obtained over a specified time or until a particular temperature level or the steady state is attained.

The equation (36) may be nondimensionalized to obtain a general solution applicable to a variety of different problems, governed by a similar equation. The only parameter is and, employing the nondimensionalization of x and t in terms of the characteristic length L and a reference temperature t_r, respectively, and of time as $\alpha\tau/L^2$, the governing equation is obtained, in dimensionless terms, as

$$\frac{\partial\theta}{\partial\bar{\tau}} = \frac{\partial^2\theta}{\partial X^2} \qquad \text{---- (45)}$$

where $\theta = t/t_r$, $X = x/L$, and $\bar{\tau} = \alpha\tau/L^2$. The temperature t_r

may be taken as the initial temperature of the body, if it is isothermal, or as the maximum or minimum temperature in the initial distribution.

6.2.1 Stability Criteria

Stability is often the overriding concern in the choice of a numerical method. The conditional stability of the two-level explicit schemes, may at times lead to extremely small time steps. However, this disadvantage must be weighed against the simplicity of an explicit method and the ability of such methods to handle nonlinear problems without iteration. In addition, the accuracy of the time integration depends on the time step, and implicit methods are often restricted for accuracy reasons to $\Delta\tau$'s that are a small multiple of the $\Delta\tau$'s for explicit methods.

6.2.2 Crank-Nicolson Implicit Method

The Crank-Nicolson method is very frequently used for solving one-dimensional transient conduction problems because of the resulting second-order accuracy in time. Also since the resulting matrix is tridiagonal the resulting system of linear algebraic equations is easier to solve. The problem is of one-dimensional unsteady-state conduction in a plate, which is initially at a uniform temperature $\Theta = 0$. At time $\overline{\tau} = 0$, the temperature Θ at one surface, $X = 0$, is raised to 1.0 and held at this value,

while the other surface is kept perfectly insulated. The finite difference equation for the application of the Crank-Nicolson method to equation (45) is

$$-r.\theta_{i+1}^{(n+1)} + 2(1+r).\theta_i^{(n+1)} - r.\theta_{i-1}^{(n+1)} = r.\theta_{i+1}^{(n)} + 2(1-r).\theta_i^{(n)} + r.\theta_{i-1}^{(n)} \qquad \text{---- (46)}$$

where $r = \Delta\bar{\tau}/(\Delta X)^2$

$\bar{\tau} = n.\Delta\bar{\tau}$

$X = i.\Delta X$

The initial and boundary conditions are

$$\theta(X,0) = 0 \quad \theta(0,\bar{\tau}) = 1 \quad \frac{\partial\theta}{\partial X}(1,\bar{\tau}) = 0$$

For the last condition, at X = 1, the second-order difference approximation is employed, given by

$$\left(\frac{\partial\theta}{\partial X}\right)_i = \frac{-\theta_{i-2} + 4.\theta_{i-1} - 3.\theta_i}{2.\Delta X}$$

So the resulting equation is given as

$$\theta_o^{(n+1)} = \frac{r}{r+1}\theta_1^{(n+1)} + \frac{r}{r+1}\theta_1^{(n)} + \frac{1-r}{1+r}\theta_o^{(n)} \qquad \text{---- (47)}$$

where θ_o is the temperature at the surface and θ_1 at the adjacent grid point.

6.3 Ending Discussion

In order to determine the transient temperature distribution in the pressure transducer, both the analytical [41] and Crank-Nicolson Numerical method [42] are used to provide better understanding of the phenomena. For the analysis, the pressure transducer is idealized as an isotropic cylinder and following assumptions are made

1. There is no heat transfer along the Y or Z direction.
2. The back surface of the pressure transducer is perfectly insulated.
3. The temperature of the front surface of the transducer is raised from the normal temperature to a high value in a zero time period, which is practically impossible.

In order to carry out the analysis, the following numerical values are used

Length of Pressure Transducer, L = 0.1 meter

Thermal Diffusivity of material, = 0.032087E-05 m^2/s

Initial Temperature, t_o = 90^oF

Temp. of surface exposed to blast = 6000^oF

Table 2 contains the numerical results of the analysis. The results from the Crank-Nicolson numerical method are given in figure 12, for a time step of 0.0311 second. As shown in figure 13 the analytical solution converges to the numerical result, when the number of terms used in Equ. 44 are increased from 200 to 1400. The data represents the temperature at a section 0.02 meter from the

Time Sec	Temperature, ^{o}F Analytical Sol.	Temperature, ^{o}F Crank-Nicolson
0.0311	90.0006135191188150	90.0002731385581711
0.0622	90.0006129764906290	90.0005093495868102
0.0933	90.0006129764760771	90.0012545326879163
0.1244	90.0006129764706202	90.0019627882628547
0.1555	90.0006129764660727	90.0031792613944183
0.1866	90.0006129764615252	90.0043588070090550
0.2177	90.0006129764615252	90.0060458167138577
0.2488	90.0006129764578872	90.0076958989168360
0.2799	90.0006129764560682	90.0098526927914619
0.3110	90.0006129764542492	90.0119725591852244

Table 2: Table showing the transient temperature at 0.01 meter.

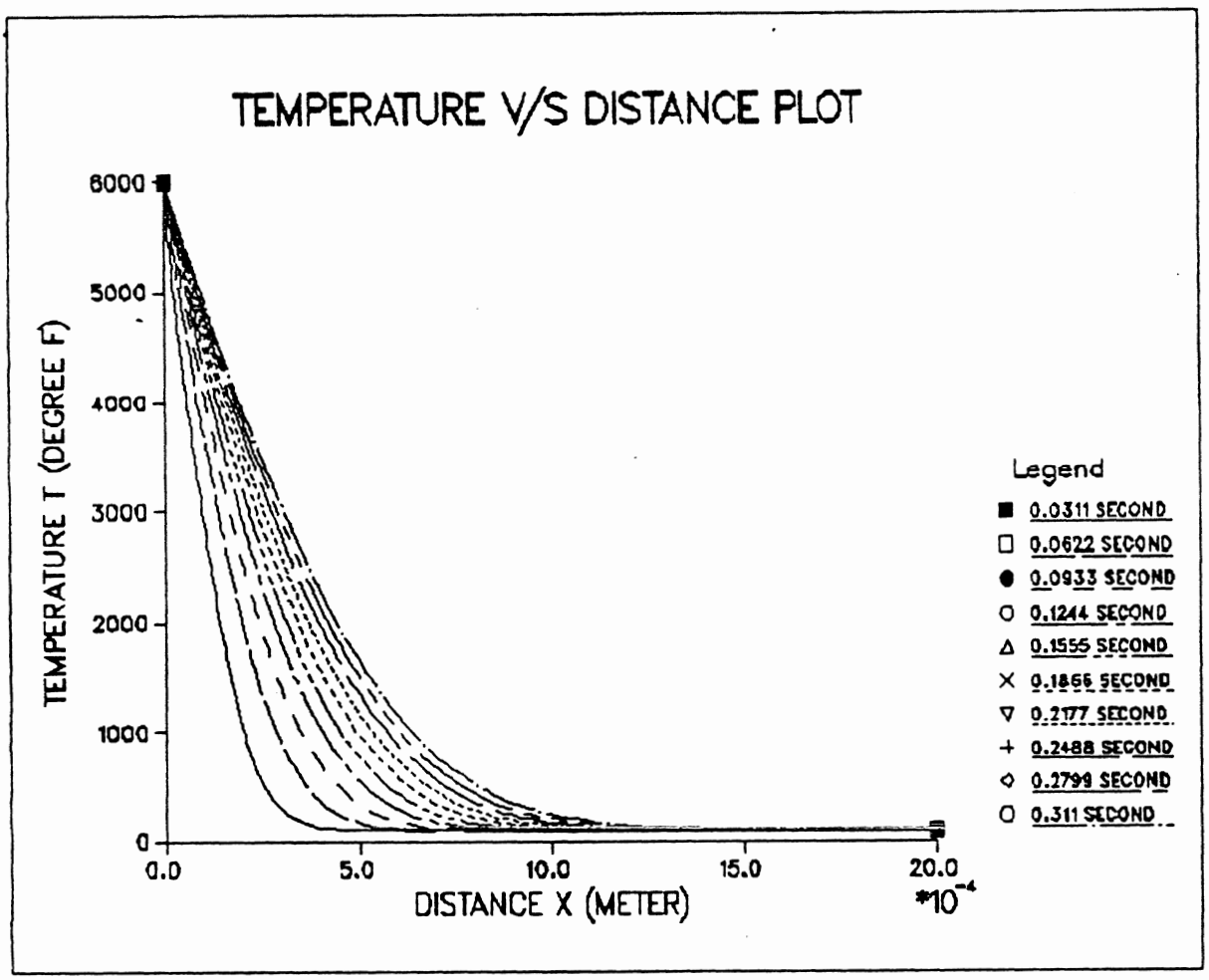

Figure 12: Solution from Crank-Nicolson Numerical Method.

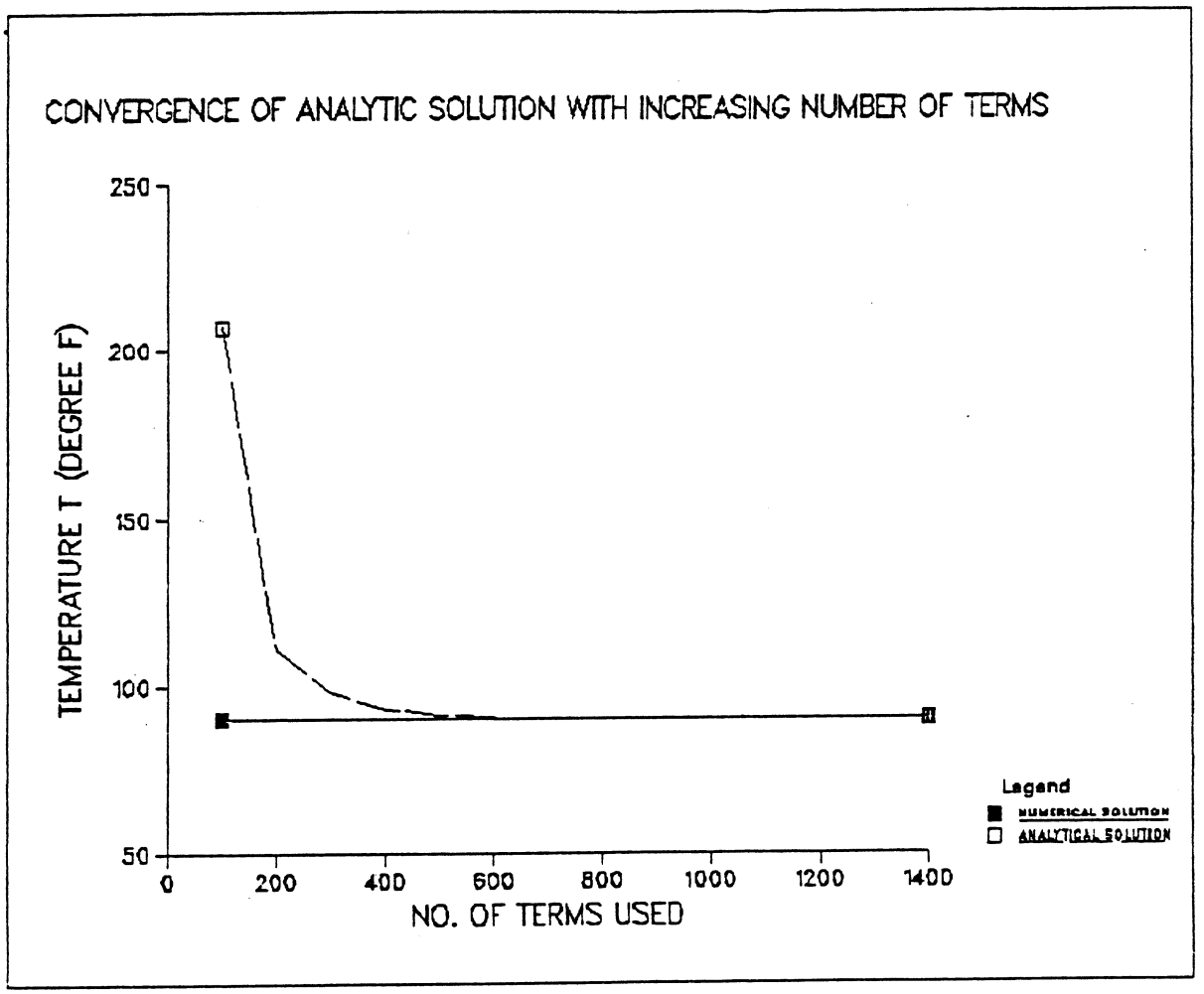

Figure 13: Convergence of Analytical Solution with increasing number of terms.

high temperature side at time 0.0623 second. The result clearly indicates that the two analysis techniques yield almost identical results. Moreover figure 14 contains the analytical solution for a time step of 0.0311 second and using 1400 terms in equation (44). These results demonstrate that the temperature becomes practically constant at a distance of about 0.5 mm from the hot surface. Analysis done by W.H.Gourdin [43] for high energy shocks had shown similar results.

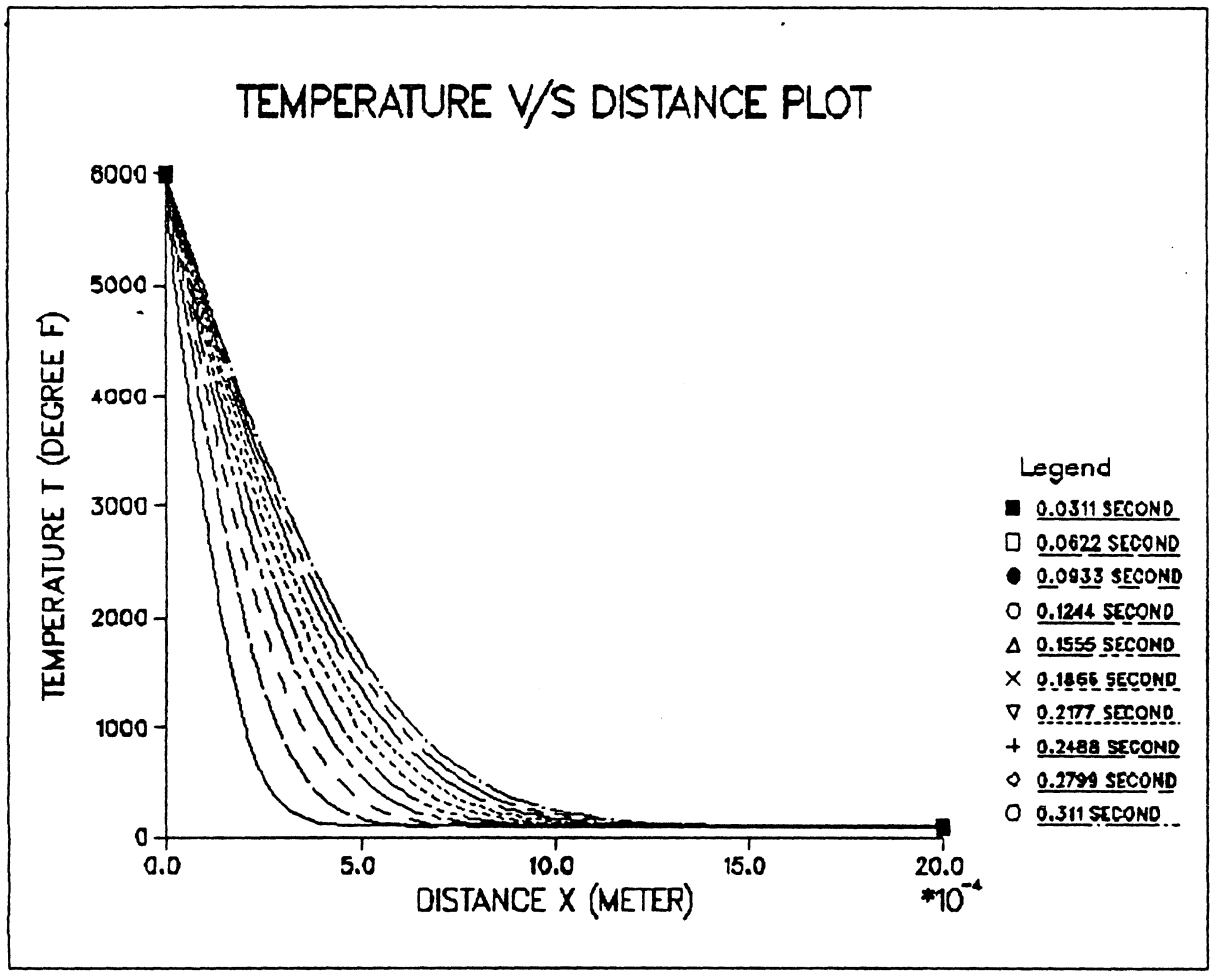

Figure 14: Analytical Solution using 1400 terms.

CHAPTER 7

COMPUTER MODELING OF THE SENSOR

Most analyses of the propagation of shock waves in condensed matter are based on the continuum approximation and are conducted numerically. This approach not only lends itself to the solution of practical problems in complex geometrical settings but also permits analyzing the physical response of materials exhibiting viscoelasticity, plasticity, viscoplasticity, compaction, phase transformation, electromagnetic activity, chemical decomposition, fracture, fragmentation, and other responses.

During the propagation of compressive waves, the stiffness, and therefore the wave velocity, increases with compression, causing the propagating wave front to steepen into a shock wave or discontinuity. The presence of such a front violates the continuity assumption inherent in the differential equations. There are two methods of dealing with these discontinuities as described below.

7.1 Shock Fitting Technique

In this technique, the shock waves are considered to be mathematical discontinuities and are treated as internal moving boundaries [44]. Discretized numerical methods are

used in the continuous regions between shocks, and the solutions are joined across shocks by means of the shock jump relations.

A variant of the shock fitting method utilizes a discrete mesh in the characteristic directions [45], rather than along constant space and time directions. This method has been used quite successfully in one dimension; in particular, the SWAP code [46] utilizes the fact that the shock jump relations reduce to the acoustic relations for infinitely weak shocks. Smooth motions are, in effect, represented as a series of weak shocks. The logic of handling wave interactions is thereby reduced to a manageable size, and the SWAP code can handle a wide variety of problems.

Nevertheless, the shock fitting method obviously involves severe complications in logic to keep track of numerous moving boundaries, particularly when shock waves can interact with each other, with material interfaces and with boundaries to give rise to further shocks. While the method has been applied successfully in one dimension and to some extent in two dimensions, computer programs are usually limited to specific kinds of problems in which shock waves are known to propagate in certain regions and in certain directions.

7.2 Artificial Viscosity Technique

A second method of dealing with shock waves involves the use of viscosity to limit the high frequency content of solutions. In effect, shock waves are broadened so that they may be represented as continuous profiles with a reasonable computational grid. Thus shock waves are recognized as very steep but finite gradients in the solution. It is clear that a shock wave must occupy several zone widths in order to satisfy the requirement that differences in physical quantities across a zone remain small.

Natural viscosity can be used. However, for most materials natural viscosity is so small that shocks would be extremely narrow and very difficult to resolve numerically. To insure that a shock occupies several zones, the zones would need to be very small. This approach would result in an extremely large number of zones for most physical problems. To avoid this problem, an artificially large viscosity is introduced. Care is necessary that the viscous term does not affect the solution anywhere except near shocks. At shocks the solution is intentionally distorted to insure that gradients are much lower than in nature. In effect, use of artificial viscosity broadens or smears shock waves. Thus, for normal materials, the tendency for pressure waves to steepen is balanced by the spreading caused by the artificial viscosity. This

approach provides the benefit of accurate results in the area of interest while the total number of zones are kept to a reasonable level.

7.3 WONDY Computer Code used for Analysis

The author contacted several laboratories that are involved in research on transient response of solids to shock waves. These sources supplied software to simulate and analyze shock waves as listed below

	TITLE	AUTHOR	AFFILIATION
1.	SWAP-9 [46]	Barker, L.M.	Sandia National Laboratories
2.	HEMP [47]	Giroux, E.D.	Lawrence Livermore National Laboratories.
3.	WONDY-V [48]	Kipp, M.E.	Sandia National Laboratories

Table 3 is a list of the merits and limitations of different shock wave analyzing programs. Based on this comparison the WONDY-V was implemented on the VAX-751 computer at Ohio University. WONDY is a one-dimensional, Lagrangian finite difference, wave propagation code. The method of artificial viscosity is used to analyze the shock wave; different material layers, initial conditions, and boundary conditions may be accommodated. A second order, finite difference algorithm replaces the spatial derivatives in the equations of motion. The fields that

	Dimensions	Rectangular Symmetry	Cylindrical Symmetry	Spherical Symmetry	Lagrangian, Eulerian	Multiple Materials	Spall and Join	Sliding Interfaces	Rezone	Hydro (2)	Explosives (2)	Elastic-Plastic (2)	Porous (2)	Viscoelastic (2)	Composite (2)	Stress Spall Criterion (2)	Cumulative Damage (2)	Thermal Conduction	Radiation Diffusion
WONDY	1	Y	Y	Y	L	Y	Y	na	Y	Y	Y	Y	Y	Y	Y	Y	Y	N	N
SOC	1	Y	Y	Y	L	Y	Y	na	N	Y	Y	Y	Y	N	N	Y	N	N	N
PISCES 1DL	1	Y	Y	Y	L	Y	Y	na	Y	Y	Y	Y	Y	N	N	Y	N	Y	N
CHART D	1	Y	Y	Y	L	Y	Y	na	N	Y	Y	Y	Y	N	N	Y	N	Y	Y
PUFF IV	1	Y	N	N	L	Y	Y	na	Y	Y	N	Y	Y	N	N	Y	N	N	N
SRI PUFF	1	Y	N	N	L	Y	Y	na	Y	Y	N	Y	Y	N	N	Y	Y	N	N
RIP	1	Y	N	N	L	Y	Y	na	N	Y	N	Y	N	N	N	Y	Y	N	N
TENSOR	2	Y	Y	na	L	Y	Y	Y	Y	Y	N	Y	Y	N	N	Y	N	N	N
HEMP	2	Y	Y	na	L	Y	Y	Y	Y	Y	Y	Y	Y	Y	N	Y	Y	Y	N
TOODY	2	Y	T	na	L	Y	Y	Y	Y	Y	Y	Y	Y	Y	N	Y	Y	N	N
PISCES 2DL	2	Y	Y	na	L	Y	Y	Y	Y	Y	Y	Y	Y	N	N	Y	N	N	N
DORF	2	Y	Y	na	E	Y	N	na	N	Y	Y	Y	N	N	N	Y	N	N	N
HELP	2	Y	Y	na	E	Y	N	na	N	Y	Y	Y	N	N	N	Y	N	N	N
CSQ	2	Y	Y	na	E	Y	N	na	N	Y	Y	Y	Y	N	N	Y	N	Y	Y
SMITE	2	Y	Y	na	E	Y	N	na	N	Y	Y	Y	N	N	N	Y	N	N	N
AFTON	2	Y	Y	na	C†	Y	N	na	N	Y	Y	Y	N	N	N	Y	N	N	N
HEMP 3D	3	Y	na	na	L	Y	Y	N	Y	Y	Y	Y	Y	Y	N	Y	Y	Y	N
TRIOIL	3	Y	na	na	E	Y	N	na	N	Y	Y	Y	N	N	N	Y	N	N	N

Table 3: Comparision of computer programs for dynamic response analyses of solids.

describe the material response are approximated as finite dimensional vectors. The components of these vectors correspond to zones of the spatial finite difference mesh. The evolution in time of these vectors is given at discrete points which are determined by time increments of length Δt_N. The increments are determined by the program which uses a criterion for numerical stability.

The fields that describe the initial state of the first zone of the spatial mesh are known. The equation of motion are evaluated to give the acceleration of the zone in terms of the stress and density of the zone as well as those of its neighbors. Since the acceleration of the zone in known, the first time increment, Δt_1, may be used to calculate the velocity and displacement of the zone at the end of the time increment. The continuity requirements are then used to determine the zone strain at the end of the time increment. By using an equation-of-state subroutine, the new zone stress can be calculated from the constitutive relation for the material in the zone. The calculation proceeds in the same manner through the remaining zones of the mesh. The equation-of-state subroutine also calculates the speed of sound for the material in a given zone. The speed of sound and zone thickness are used to determine a new time step, using the stability criterion. The new time step is the smallest of the time increments found for each zone of the mesh. The calculations of new values of

velocity, displacement, strain, and stress for all zones of the mesh is called a mesh cycle. The mesh cycle calculation is repeated for each new time increment until the problem is completed.

WONDY has been employed as a research tool for studying dynamic fracture, piezoelectricity, ferroelectricity, viscoelasticity, explosive reactions, and the behavior of granular, porous and bubbly materials.

7.4 Construction of Constitutive Relations

The response of materials to the application of physical phenomena such as contact forces, heat, electrical fields, etc. is represented mathematically by equations called constitutive relations [49]. Hooke's law is one: it says that stress is proportional to strain. Newton's law of viscosity and Ohm's law of electrical resistance are others. Constitutive relations can take various mathematical forms, including those of algebraic, differential or integral equations and functionals of the history of deformations to which the material has been subjected. Various levels of sophistication can be represented in the material description by the inclusion or exclusion of effects such as finite compression, entropy variation, strain hardening and viscosity. To be useful, these theories must accurately represent the underlying physical processes and be computationally feasible. The

following two sections contain a discussion on the constitutive modeling of PVDF piezo film and EPON 828-Z potting mixture.

7.4.1 Constitutive modeling of PVDF piezo film

In impact problems which involve only mechanical effects the material ahead of the wave is at rest and conditions prevailing at the downstream boundary of the material have no effect on the wave until it arrives there. In the case of piezoelectric materials, the dependence of the stress on the electric field or, equivalently, the electric displacement, results in the development of stresses in regions of the materials that would be undisturbed in a purely mechanical or open-circuit problem [50]. Thus the disturbance introduced at the impact surface will immediately result in stresses in the region near the downstream surface of the material. Since this surface is to be free of stress, a relief wave will arise here and propagate into the interior of the material. This wave would be absent if there were no electro-mechanical coupling. This behavior distinguishes these materials from simpler materials in which information travels only at the local sound wave speed.

There are other effects of electromechanical coupling as well. Lysne [51] has pointed that if this coupling is neglected, the relative error in computations tends to

increase with time as the wave is allowed to reverberate in the piezoelectric material.

A fully coupled nonlinear theory of propagation of plane longitudinal stress waves in piezoelectric solids has been developed by Chen, Davison and McCarthy [50]. The numerical method used to implement this theory, using WONDY computer code is discussed below.

7.4.1.1 Assumptions and Preliminaries

A plane wave of uniaxial strain propagating in a material body may be described by a function giving the present position x of each material point X of the body at time t, i.e.,

$$x = \chi(X,t)$$

Moreover, the particle velocity $\dot{x}$, deformation gradient F and strain S are defined by the relations

$$x = \partial\chi / \partial t$$

$$F = \partial\chi / \partial X$$

$$S = F - 1 = \partial u/\partial X \qquad \text{---- (48)}$$

In the above relations $F > 0$, while $S > 0$ for extension of the body and $S < 0$ when it is compressed. The voltage V across the disk is the integral of the electric field and is given as

$$V(t) = -\int_{x_1}^{x_2} E(x,t)\, dx \qquad \text{---- (49)}$$

By changing the limits of integration, we get

$$V(t) = -\int_{X_1}^{X_2} F(X,t)\ E(\chi(X,t),t)\ dX$$

When the external circuit consists simply of a resister of resistance R connected across the disk, the current I in the circuit is given as $I = A.\dot{D}$. Also $V = I.R$. So

$$A\ R\ \dot{D}(t) = -\int_{X_1}^{X_2} (1+S)\ E(\chi,t)\ dX \qquad \text{---- (50)}$$

where,

X_1, X_2 : material coordinates of the faces of the disk.

A : area of the charge-collecting electrode on the disk.

R : resistance of the external circuit connected across the two electrodes.

E : electric field strength.

For the piezoelectric materials, the constitutive functions σ and E are adequately represented by expressions of the form [52]

$$\sigma(S,D) = c^D_{11}\ S + 0.5\ c^D_{11S}\ S^2 + 0.166\ c^D_{11SS}\ S^3 - h_{11}\ D - h_{11S}\ S\ D + 0.5\ \beta^S_{11S}\ D^2 \text{ --- (51)}$$

$$E(S,D) = -h_{11}\ S - 0.5\ h_{11S}\ S^2 + \beta^S_{11}\ D + \beta^S_{11S}\ S\ D \qquad \text{---- (52)}$$

In these equations, the superscripts follow the convention

described in Section 4.2.2. Subscripts 11, 11S, 11SS implies first, second and third order material constants. Moreover

C : Elastic Coefficients (GPa)

β : Dielectric Coefficients (Gm/F)

h : Piezoelectric Strain Coefficients (GN/C)

When Equ. (52) is substituted into the current equation (50), we obtain the reduced form

$$A\ R\ \dot{D} + \alpha(t)\ D = \beta(t) \qquad \text{---- (53)}$$

where,

$$\alpha(t) = \int_{X_1}^{X_2} (\beta^S_{11} + \beta^S_{11S}\ S)\ (1 + S)\ dX \qquad \text{---- (54)}$$

and

$$\beta(t) = \int_{X_1}^{X_2} (h_{11}\ S + 0.5\ h_{11S}\ S^2)\ (1 + S)\ dX \qquad \text{--- (55)}$$

The function α^{-1} is the capacitance per unit area of the piezoelectric disk and β is the voltage generated at the electrodes due to the piezoelectric polarization of the materials.

7.4.1.2 Numerical Analysis

To adopt the WONDY code to the fully coupled electro-mechanical problem, the electrical circuit equation (53)

must be solved simultaneously with the momentum equation and the stress relations. The WONDY code provides the frame work for simultaneous solution of the latter two expressions, so the present modifications involve incorporation of the circuit equation (53). This equation is a linear, first-order ordinary differential equation. It represents the time-dependent behavior of an electrical circuit containing a constant resistance R and a capacitance $C = A/\alpha$. As such, its temporal response is characterized by a response time

$$\tau = R C = R A/\alpha$$

In the case of a shock pressure gage response, a value of τ on the order of 0.01 ns is typical. In the absence of the electrical coupling, the momentum balance calculation would typically proceed in time steps, ΔT, of the order of 1.0 ns. Since this calculation takes the majority of the computer time, the discrepancy in the response times suggests that the circuit calculation should proceed on a subcycle basis, being advanced a rather large number of time steps before the next necessary advance of the momentum balance calculation. This subcycle integration of the circuit equation is feasible since the coefficients $\alpha(t)$ and $\beta(t)$, which couple the electrical response to the mechanical state of the system, change with time at the same rate as the average strain in the material changes. Thus these coefficients need to be updated only at the

relatively infrequent intervals ΔT when the momentum balance calculation is advanced. On the basis, we can write

$$D^{m+1} = \frac{D^m(1/\Delta t - \alpha/2AR) + \beta/AR}{(1/\Delta t + \alpha/2AR)} \quad , \quad m = 1, \ldots, M$$

as a first-order centered finite-difference representation of Equ. (53). In this equation α and β are calculated from the difference expressions

$$\alpha = \sum_j (\beta^S_{11} + \beta^S_{11S}\, S_j)\ (1 + S_j)\, \Delta X_j$$

and

$$\beta = \sum_j (h_{11}\, S_j + 0.5\, h_{11S}\, S_j^2)\ (1 + S_j)\, \Delta X_j$$

which are the discrete form of the defining integrals (54) and (55). In these expressions, the range of the summations corresponds to the Lagrangian zones of the piezoelectric layer. The integer M is the number of time subcycles of the circuit equation within one cycle of the momentum balance calculation. The new value of D realized when the subcycle integration has run through its M steps can be used along with the strain to evaluate the stress relation and thus complete a computational cycle. Substituting the difference, ΔD, between the new and the old values of D into the finite-difference analog of equation (53), gives

$$I = A\, \Delta D / \Delta T \qquad \text{---- (56)}$$

This equation represents the current in the external circuit.

7.4.1.3 Experimental Validation

Experimental results obtained by Graham [53] were used to validate the prediction of this constitutive formulation. In these experiments a X-cut quartz sample was impacted by similar quartz plate at a velocity of 328 m/sec. The result of the comparison between the experimental and calculated results is given in figure 15. Properties of X-cut quartz and the experiment parameters are given below:

Velocity of quartz impactor	: 328 m/sec
Diameter of quartz sample	: 0.00015 m^2
Thickness of quartz sample	: 0.007 m
Density	: 2650 Kg/m^3
Bulk Sound Speed	: 5724 m/sec
Poisson's Ratio	: 0.345
1st order Dielectric Coefficient, β_{11}	: 25 Gm/F
2nd order Dielectric Coefficient, β_{11S}	: 11.5 Gm/F
1st order Piezoelectric Constant, h_{11}	: -4.28 GN/C
2nd order Piezoelectric Constant, h_{11S}	: 58 GN/C
1st order Elastic Constant, C_{11}	: 86.8 GPa
2nd order Elastic Constant, C_{11S}	: -210 GPa
3rd order Elastic Constant, C_{11SS}	: 6600 GPa

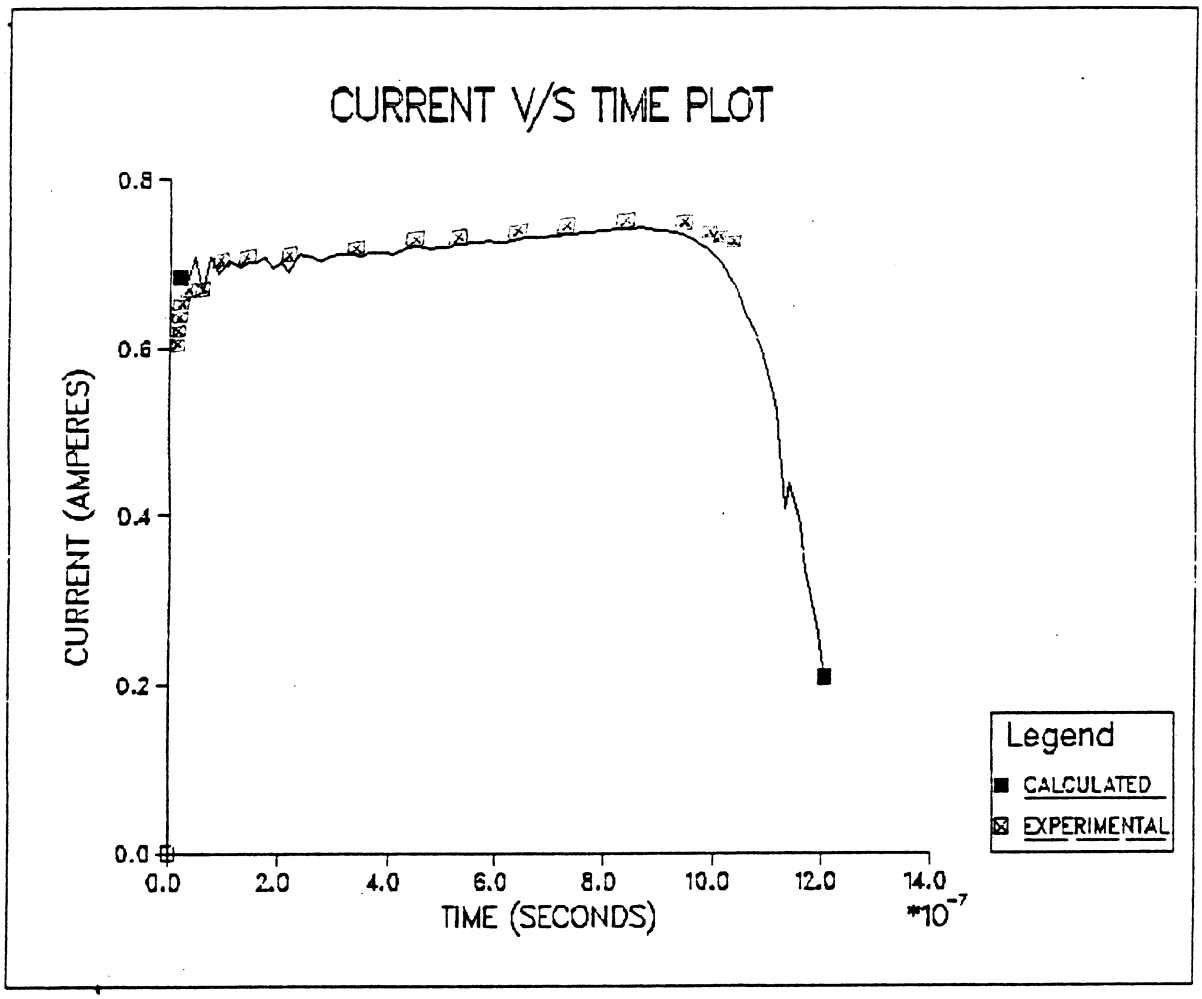

Figure 15: Calculated and observed current from X-cut quartz slab during the first transit of a wave produced by impact with a similar slab at a velocity of 328 meter/sec.

It is apparent from figure 15, that the experimental and calculated results are in good agreement with each other. The disagreement at early time can largely be a result of nonplanarity of impact ("tilt") in the experiment, although the oscillations in the computed current are a numerical artifact. The steep drop in the current is the result of the exit of the shock wave from the sample material. Since the experimental data was available only for one pass of the shock wave, the numerical simulation has also been restricted to one transit.

7.4.2 Constitutive modeling of Epon 828-Z mixture

The STAT1 routine provides a numerical approximation to the behavior of Epon 828-Z mixture. This routine is a part of the original WONDY V code and is based on the elastic-perfectly plastic behavior of materials. For lower stress levels or where stress deviators cannot be assumed negligible, the elastic-plastic portion of the material model must be considered.

For a material which can support shear stress, the constitutive relation is of the following form:

$$\sigma_x = f(S_x, S_y, S_z, \varepsilon) \qquad \text{---- (57)}$$

with similar equations for σ_y and σ_z. In the above

equations S_x, S_y, S_z are the strain rates and $\mathcal{E}$ is the internal energy.

7.4.2.1 Stress-Strain Relations

In one dimensional motion the coordinate axes coincides with the principle stress and strain orientations. Since the shear strains are absent, it is convenient to work in terms of the strain rate or stretching. In the direction of motion, i.e., the x direction, the stretching function is

$$d_x = \partial u / \partial x \ , \qquad \text{---- (58)}$$

and since there is no motion in the y and z coordinate directions

$$d_y = 0 \quad \text{and} \quad d_z = 0$$

The volumetric strain rate or dilation is defined as

$$d = d_x + d_y + d_z \qquad \text{---- (59)}$$

which is related to the rate at which the density is changing by

$$d = -\partial \rho / \rho . \partial t \qquad \text{---- (60)}$$

The deviatoric strain rate components in the x direction are defined as

$$d_x^d = d_x - d / 3 \qquad \text{---- (61)}$$

and similar relations hold for d_y^d, d_z^d. They are a measure of the rate of distortion independent of the volume change. Substituting equation (61) in equation (59) gives

$$d_x^d + d_y^d + d_z^d = 0 \qquad \text{---- (62)}$$

Since the shear strains are zero in one dimensional motion, shear stresses are zero. The stress components in the coordinate directions are σ_x, σ_y, σ_z. The pressure is defined as

$$(-p) = (\sigma_x + \sigma_y + \sigma_z) / 3 \qquad \text{---- (63)}$$

the minus sign is in agreement with the convention that stresses are considered positive in tension, and pressure is considered positive in compression. Deviatoric stresses are defined as

$$\sigma_x^d = \sigma_x - (-p) = \sigma_x + p \qquad \text{---- (64)}$$

Similar relations hold for σ_y^d and σ_z^d. Combining equation

(63) and equation (64), we get

$$\sigma_x^d + \sigma_y^d + \sigma_z^d = 0 \qquad \text{---- (65)}$$

7.4.2.2 Numerical Analysis

In the case of materials exhibiting plasticity, the deviatoric stresses have an upper limit determined by the yield condition. The Von Mises yield condition is

$$f_y = (\sigma_x^d)^2 + (\sigma_y^d)^2 + (\sigma_z^d)^2 <= 0.667\ Y^2 \qquad \text{---- (66)}$$

where $Y(\rho, \mathcal{E})$ is a material constant called the yield stress. Combining equation (65) and equation (66), gives

$$f_y = 2\ \{(\sigma_x^d)^2 + \sigma_x^d \cdot \sigma_z^d + (\sigma_z^d)^2\} <= 0.667\ Y^2 \qquad \text{---- (67)}$$

The symmetry inherent in rectangular and spherical one dimensional motion implies that $\sigma_y = \sigma_z$. Thus

$$s_y^d = s_z^d = -0.5\ s_x^d \qquad \text{---- (68)}$$

$$\sigma_y^d = \sigma_z^d = -0.5\ \sigma_x^d \qquad \text{---- (69)}$$

Combining equation (67) and equation (69), gives

$$f_y = 1.5\ (\sigma_x^d)^2 <= 1.5\ Y^2 \qquad \text{---- (70)}$$

The STAT1 routine uses the finite difference form of the above equations to determine the values of the stresses. A detailed description of STAT1 routine and example problems are given in Reference [48].

CHAPTER 8

EXPERIMENTAL VALIDATION AND RESULTS

In the last decade considerable progress has been made in the development of experimental techniques for studying constitutive relationships. The determination of meaningful material properties from shock-loading experiments requires well-defined loading conditions. Since the loading method is such a crucial element in the design of an experiment, improvements in loading methods have played a leading role in advancing the study of shock pressure sensing. If the load is applied uniformly over a large planar area and the measurements are restricted to the central portion of an appropriate sample, a state of uniaxial strain is achieved, that is, the particle velocity and strain are in the direction of wave propagation. Controlled planar-shock loading has been achieved with direct-contact high explosives, explosively driven flying plates, precisely controlled impacts from gas gun projectiles, and by the deposition of energy in bulk with intense pulsed radiation from lasers, electron beams, or x-rays. The following sections contain brief discussions of the first three techniques.

8.1 Direct-Contact High Explosives

The development of explosive lenses to provide planar pressure pulses over diameters of 100 to 300 mm was instrumental in developing the science of shock-wave loading. These lenses makes it possible to obtain plane-wave detonation fronts and essentially one-dimensional planar shock fronts. These devices employ a combination of fast-detonating and slow-detonation explosives. As shown in figure 16, the explosive lens produces a planar output which is typically imparted to an explosive pad 50 to 100 mm thick. The pressure pulse then propagates through a metallic driver plate before entering the sample. By employing a variety of explosive pads, pressures from 15 to 40 GPa can be achieved. Pressures intermediate to those achieved by specific explosive materials can also be achieved by driver plates composed of alternating layers of materials of different impedances [2].

8.2 Explosively Driven Flying Plates

To achieve pressures higher than those obtained from direct-contact high explosives and to make measurements more convenient, samples are loaded with metal plates which have been accelerated to high velocities by explosive plane-wave generators. The arrangement shown in figure 17 is similar to the direct-contact method except that the plate is separated from the high explosive by a buffer of

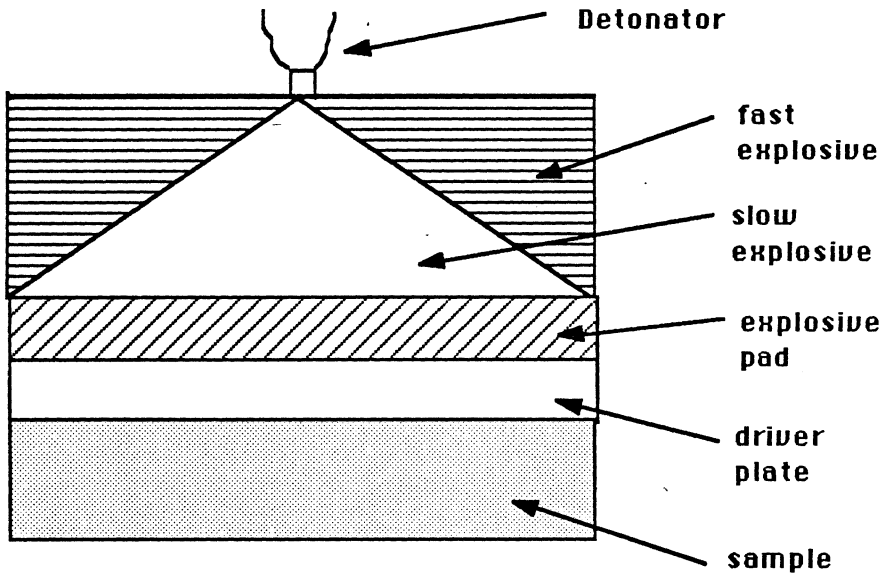

Figure 16: Direct-Contact explosive loading Method.

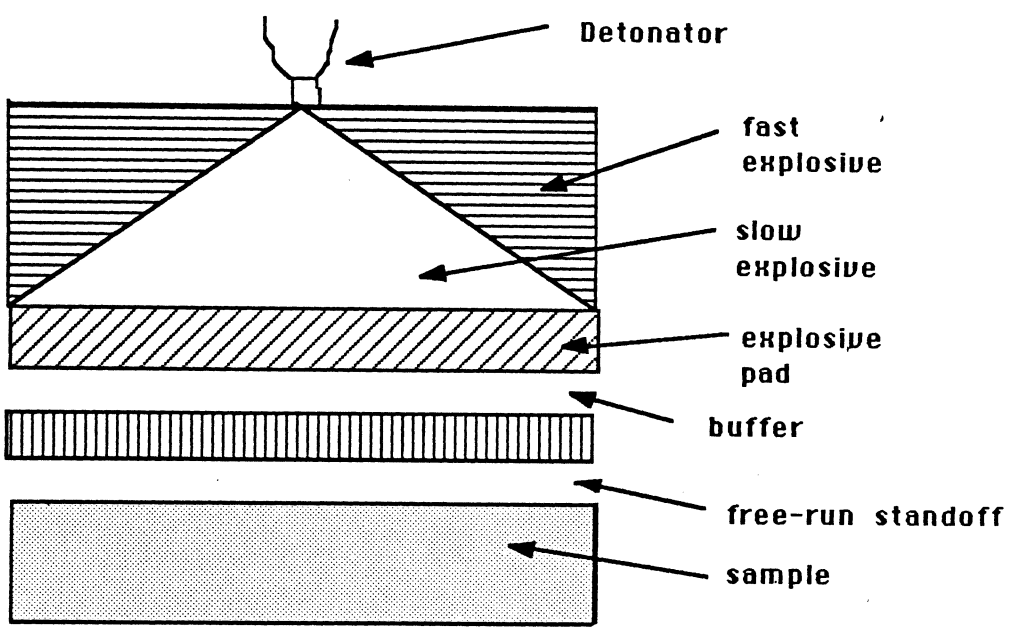

Figure 17: Explosively driven flying-plate Method.

air or plastic material and the plate is spaced from the sample by a 'free-run' distance of about 20 to 50 mm. During acceleration, the plate is heated and plastically deformed by the reverberating shock waves, but through experimentation, it is possible to avoid plate break-up or excessive bowing. Plate velocities form 1 to 7 km/s can be achieved with typical explosive driving systems.

8.3 Compressed Gas Guns

In recent years, much of the shock-wave work which was formerly done with high explosives has been carried out with one- and two-stage gas guns. These guns have several advantages, first, they enable high-pressure shock-wave experiments to be conducted under laboratory conditions; it is no longer necessary to carry out the experiments in a remote location adapted for large-scale high-explosive detonations. Second, these guns produce shock waves of a very controlled nature; the profiles behind the shock front are flat, since they are achieved by the impact of a projectile on a sample, rather than by detonation followed by a steadily decreasing pressure. It is much easier to interpret complex wave interactions in such a system. The experimenter control the shock duration and pressure with great precision and achieve velocities up to 8 km/s with much greater accuracy and convenience than with high-explosive systems.

8.4 The Experimental Setup

Battelle Laboratories have loaned the compressed gas gun used in this experiment. The gun is a short-barreled, compressed-nitrogen-operated gun equipped with vents milled into the barrel near the muzzle. The vents allow the escape of the accelerating gas from behind the projectile so that the projectile travels at essentially constant velocity for the last few inches before the impact with the target. This condition is necessary to ensure that the velocity determined by the velocity-measuring-sensors in the barrel would be the same as the impact velocity. Some of the characteristics of the gas gun are as follows [54]:

Accumulator Volume	: 60 $inch^3$
Maximum Accumulator Pressure	: <= 1000 psi
Total Barrel Length	: 36.37 inch
Barrel Inner Diameter	: 2.505 inch
Unvented Acceleration Length	: 24.0 inch
Total Length of Vented Area	: 8.5 inch
Total Vent Area	: 44.88 $inch^2$

Figure 18 contains photographs of the complete compressed gas gun firing arrangement and figure 19 is a cross section view of the gas gun firing arrangement. The following sections contain descriptions of the major features of the test setup and operation including the launcher performance, design of the projectile, design of

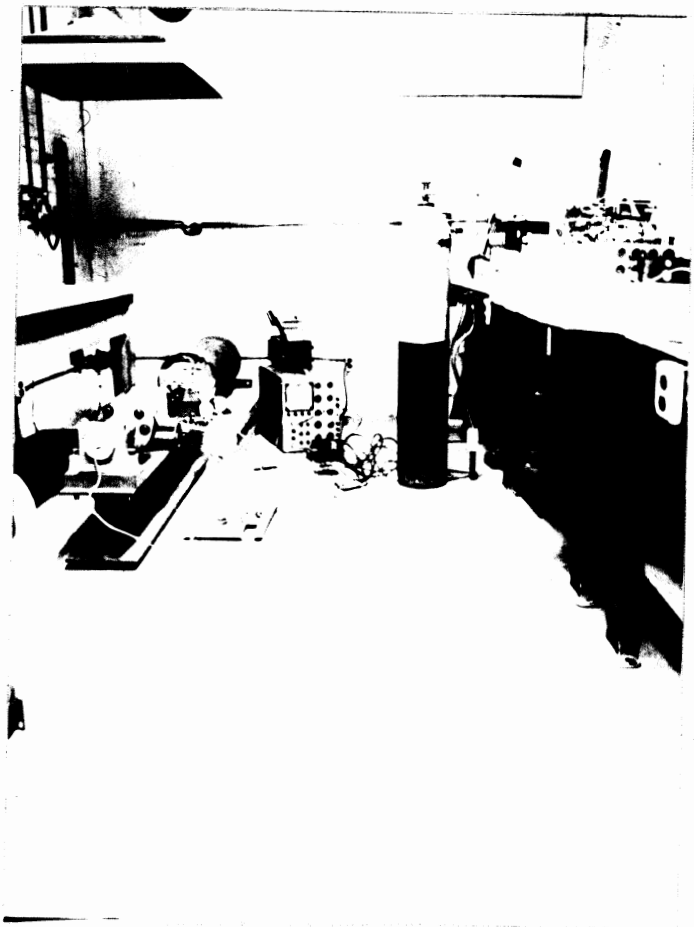

Figure 18: Photographs of the compressed gas gun firing arrangement.

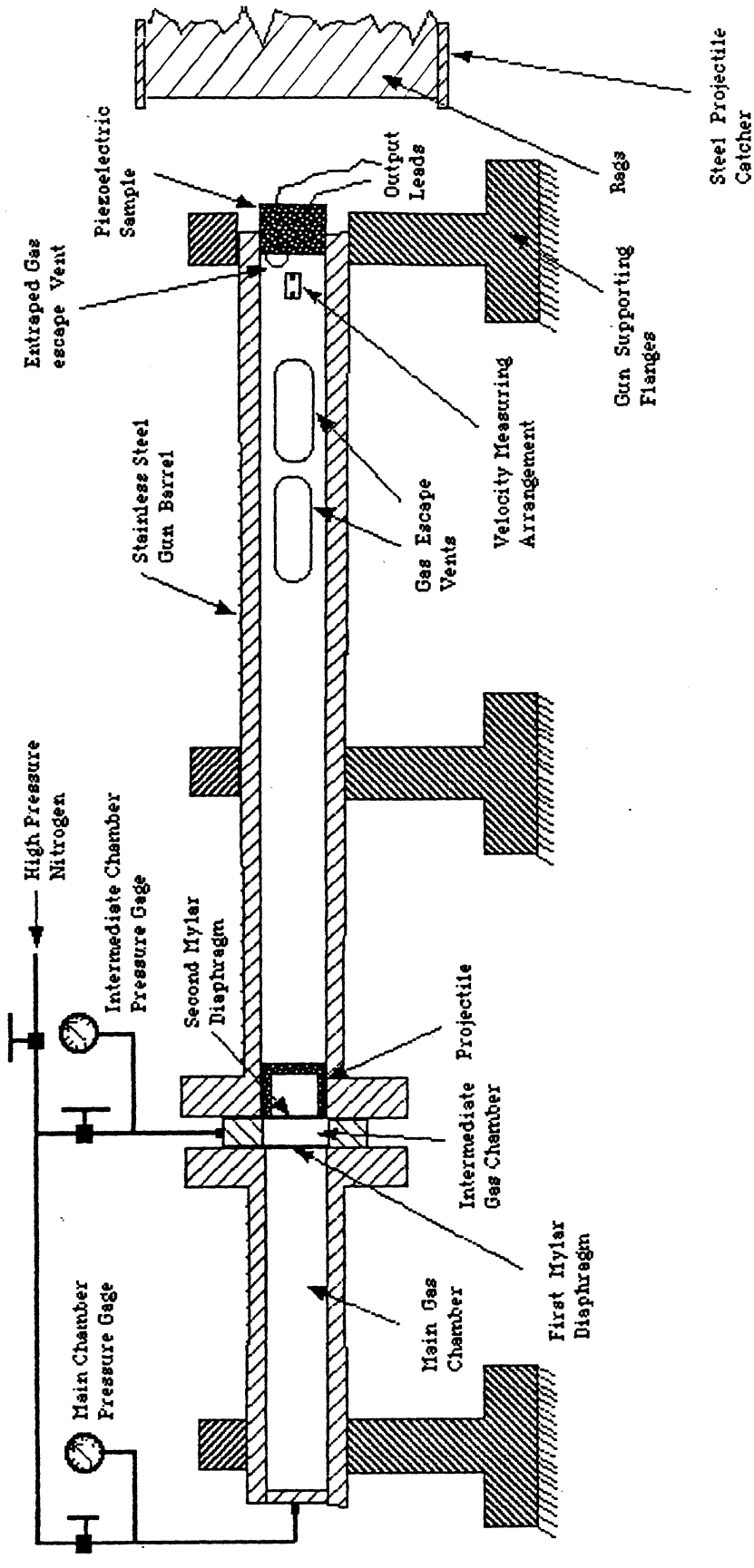

Figure 19: Cross section view of the gas gun.

the piezoelectric sample, design of the velocity measuring system, calibration of the gas gun and the test results.

8.5 Launcher Performance

The detailed design of the launcher includes two rupture diaphragms of mylar sheet plastic between the accumulator volume of pressurized gas and the initial projectile position. These diaphragms are separated by approximately one inch and each is sealed with an O-ring. In the original design, 1/8" Dia. O-rings were used, however 3/16" Dia. O-rings provided a better seal and were used in the later firings. In operation, the volume between the diaphragm is pressurized to one-half the final pressure desired in the accumulator before the accumulator is finally pressurized. Thus, the pressure drop across each diaphragm is one-half the accumulator pressure. The thickness of the mylar diaphragms is chosen such that an individual diaphragm will rupture at a pressure greater than one-half the desired accumulator pressure and less than the total pressure.

After the desired accumulator pressure is attained and stabilized, the gun is fired by venting the pressure between the diaphragms. The two diaphragms then rapidly ruptured in sequence and the accumulator pressure is applied to the rear of the projectile.

Table 4 contains the observed rupture pressures for

several thicknesses of mylar diaphragms and the comparison with the results obtained by D.B.Trott [55]. The pressure was increased slowly by bleeding in gas (pure dry nitrogen) from a high pressure cylinder and observing the rupture pressure on a Bourdon pressure gage. Several combinations of diaphragm thicknesses were used in conjunction with a range of accumulator pressures.

8.6 Projectile Design

In order to match the projectile used by B.D.Trott in his experiment at Battelle Laboratories, the projectile had a total weight of 1.0 pound. Since a high shock impedance was required, copper was chosen for the front surface of the projectile. To keep friction low and for other reasons, aluminum was chosen for the projectile material in contact with the barrel. The barrel supplied by Battelle laboratories was made of stainless steel. This combination allowed running the barrel completely clean and scratch-free, which contributed to reproducible friction effects. The thickness of the aluminum projectile skirt was chosen to be the minimum which would keep the elastic expansion of the skirt to < 0.0008 inch in diameter when launched by 300 psi gas pressure. Allowance for this expansion in the projectile diameter was made considering the 0.001 inch diametral clearance between the projectile and launch tube. The 2.10 inch length of the aluminum projectile skirt

No. of Mylar Sheets	Mylar Thickness (inch)	Observed Rupture Pressure (psi)	Rupture Pressure [Ref 55] (psi)
1	0.003	70	72
1	0.003	73	--
1	0.005	--	120
2	0.006	155	--
1	0.007	--	153
3	0.009	240	--
3	0.009	238	--
3	0.009	239	--

Table 4: Observed Mylar diaphragm rupture pressures and comparision with the results obtained by D.B.Trott [55].

avoided any possibility that the projectile would tilt while it traveled in the launch tube. In addition, the copper front end of the projectile was champhered, to insure that the projectile did not get stuck in the launch barrel because of local deformation from impact with the target. Figure 20 is a schematic drawing of the projectile and figure 21 is a photograph of the projectiles used in the experiment.

8.7 Piezoelectric Target Design

The target consisted of a circular disk of poled PVDF material epoxied to a cylindrical copper disk. A schematic diagram of the target appears in figure 22 and figure 23 is a photograph of the finished specimen. Pennwalt Corporation supplied the piezoelectric PVDF disks which were 2.5 cm in diameter and 28 microns thick. The shock wave was generated by the impact of the copper projectile and propagated along the disk axis in the same direction to that of polarization. The PVDF film was placed at the center of the 6.36 diameter copper disk to assure a uniaxial state of strain in the PVDF film at the time of impact.

The PVDF film was fastened to the disk and the connecting leads were supported with Epon 828 epoxy. 26.26 gm of epoxy resin was mixed with 5.63 gm of Z-hardener and poured into a 0.32 inch long section of 2.5 inch diameter

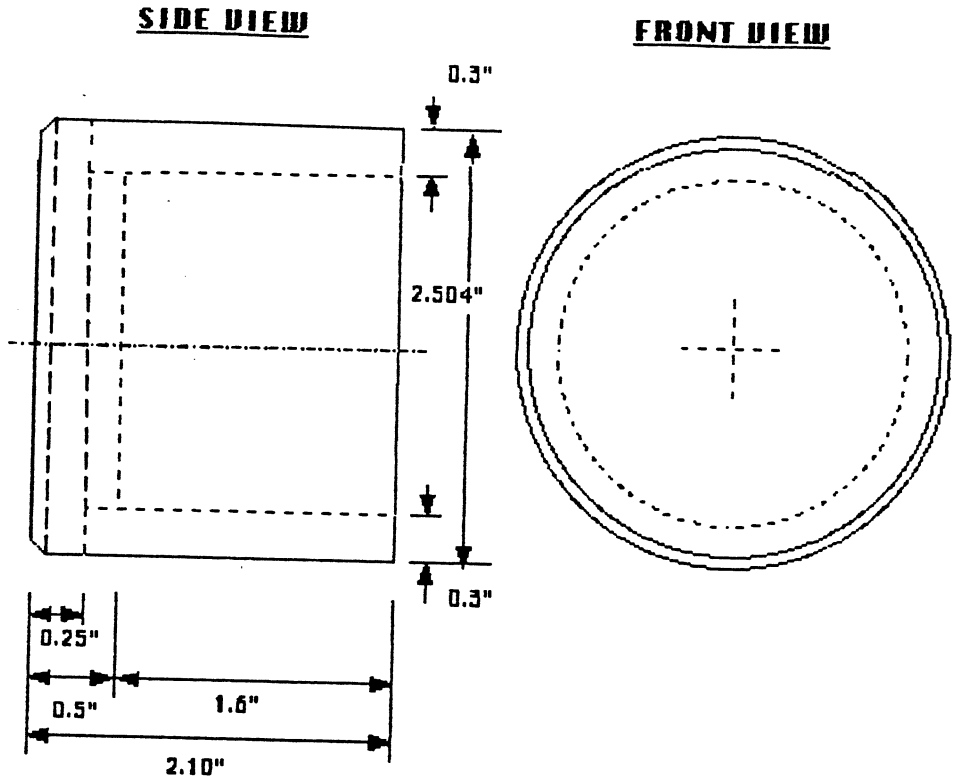

Figure 20: Drawing of the projectile used in the experiment. (Scale: 1" = 1")

Figure 21: Photograph of the projectiles.

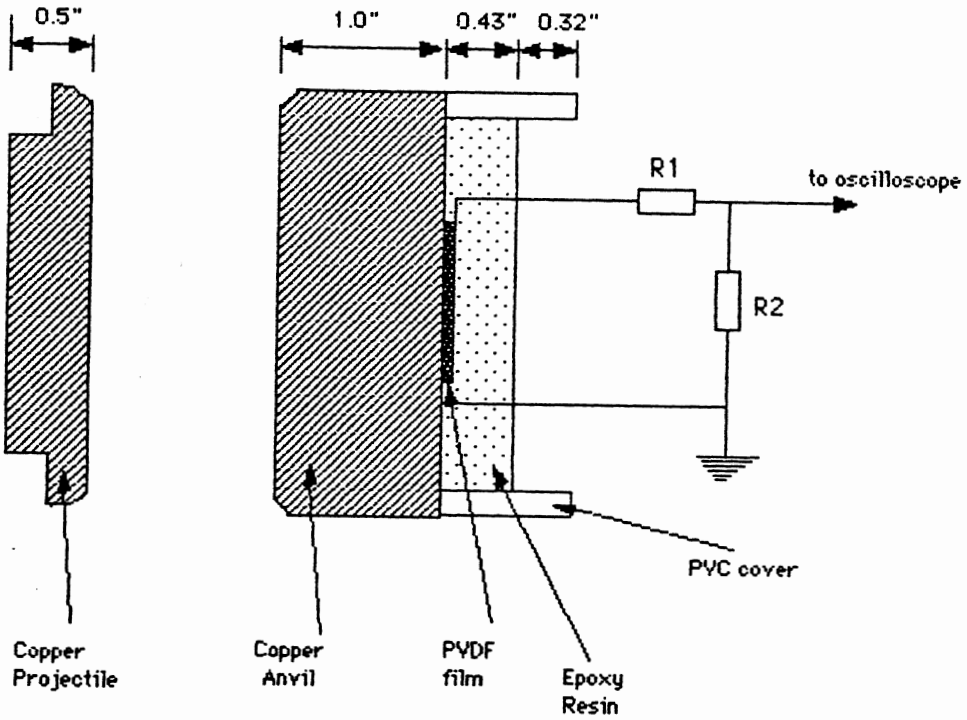

Figure 22: Schematic drawing of the piezoelectric sample and copper impactor. (Scale: 1" = 1")
Attenuation Factor = (R1 + R2) / R2

Figure 23: Photograph of the piezoelectric sample.

PVC pipe which was fastened to the back of the target. The resulting specimen was cured for 20 hours at a temperature of 88°C. The oven used for this purpose had a temperature variation of ±3°C.

Since the voltage output of hundreds of volts was expected during the impact, a 1:1181.26 voltage divider was connected to the output of the piezoelectric film.

8.8 Velocity Measuring Arrangement

Accurate measurement of velocity is a crucial factor in determining the exact shock pressure in the target material. In the original Battelle design velocity was determined from the times when the projectile contacted three accurately spaced brass pins which extended into the launcher barrel. These pins were attached to a pulse-forming circuit to trigger two electronic time interval meters. This procedure of measuring velocity was very time-consuming since new brass pins had to be fitted to the gun barrel for each firing. Two optical methods to measure velocity were developed for this experiment.

8.8.1 LASER-Photo Transistor Arrangement

In this arrangement, the projectile interrupted a LASER beam that was focused on two photo transistors that were located at the end of the barrel and spaced exactly 0.6 inches apart in the axial direction. Clairex model

CLT2160 silicon planar epitaxial photo transistors [56] were chosen for the receivers and the emitter was a portable Helium-Neon LASER with a power of 0.5 milliwatts. The spectral response characteristics of the photo transistors are given in figure 24 and the schematic drawing of the arrangement appears in figure 25. The LASER beam was split and directed by mirrors to focus on the photo transistors. The wavelength of the LASER beam was 0.6328 microns, at which the photo transistor response would be 65 percent of its peak response, as shown in figure 25. The output of each photo transistor is 0.5 volt with the beams focused on it and 5.07 volts when the LASER beam is interrupted. The response time of the photo transistors is 3 micro second which gives a sharp rectangular pulse on an oscilloscope. The time lag between the rising edge of the second pulse and the rising edge of the first pulse equals the time taken by the projectile to travel between the precisely spaced photo transistors. Since the distance between the photo transistors is known, one can determine the velocity of the projectile at that instant.

Although this arrangement gave good results upto 120 ft/sec of projectile velocity, at higher velocities the vibration of the I-beam on which compressed gas gun was mounted caused misalignment of the LASER beams and the photo transistors. Since it was impractical to mount the

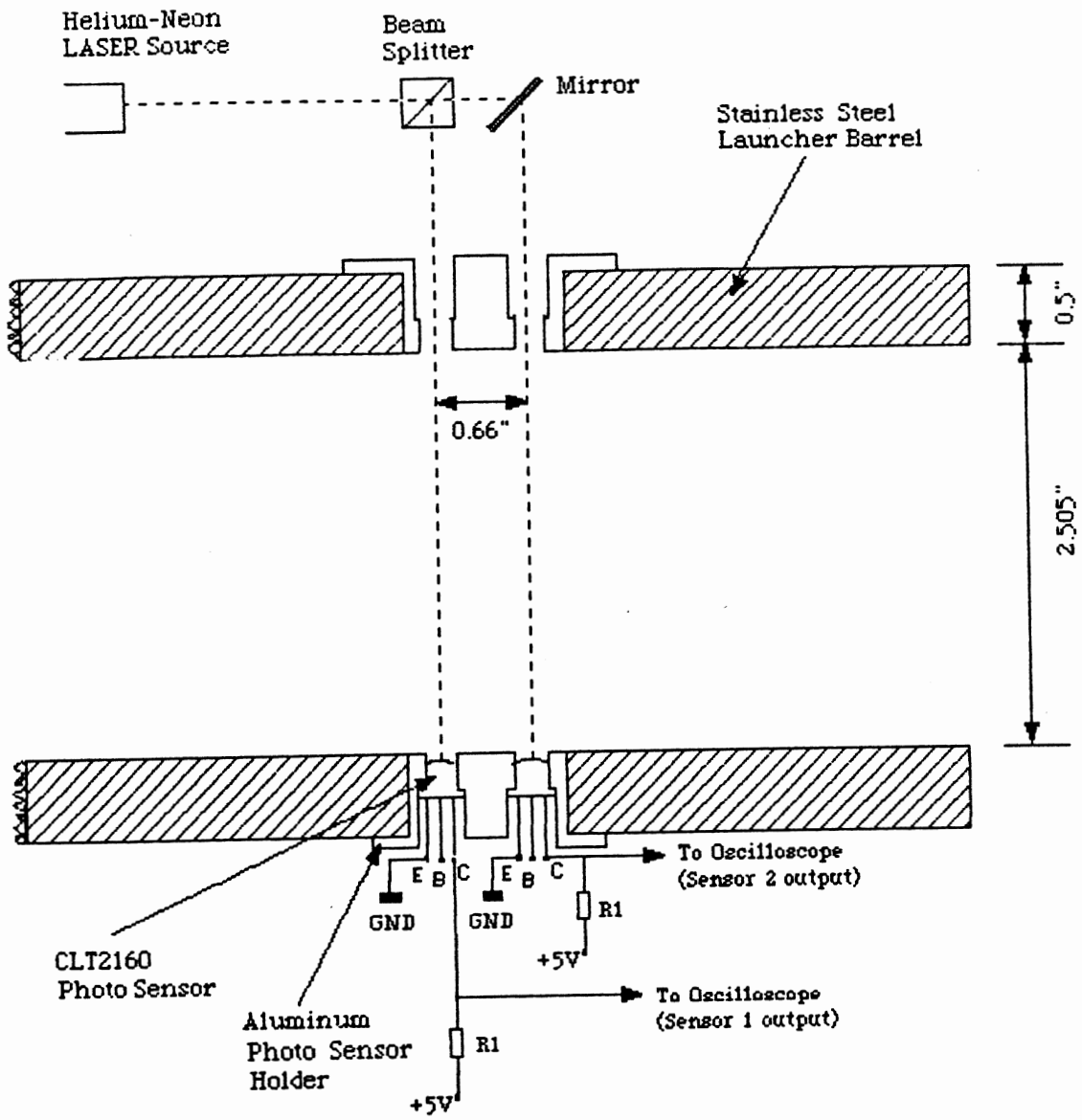

Figure 24: Schematic drawing of the LASER-Photo transister velocity measuring arrangement.

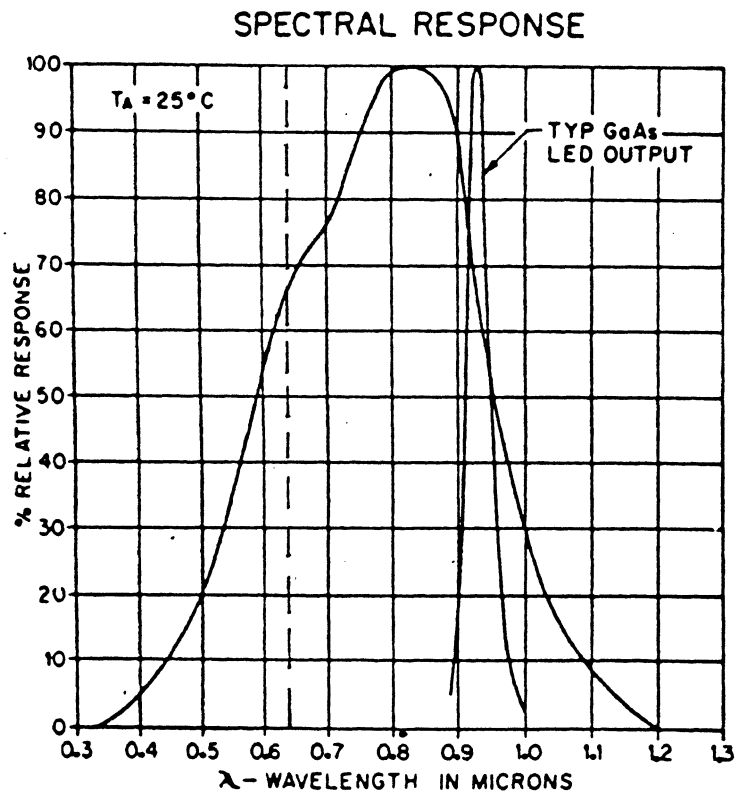

Figure 25: Spectral response characteristics of the CLT2160 photo transisters. Dotted line represents Helium-Neon LASER output [56].

LASER on the I-beam, this system was abandoned.

8.8.2 LED-Photo transistor Arrangement

In this arrangement, the same CLT2160 photo transistors were used as discussed above. However, instead of LASER beams, the light sources were two Gallium Aluminum Arsenide Infrared Emitting Diodes CLED155, manufactured by Clairex Electronics. The peak spectral point of these diodes is 880 nm which closely matches the peak response range of the photo transistors (see figure 25). These Infrared emitting diodes were mounted on the launcher barrel using a holder identical to the mounting for the photo transistors. Figure 26 is a schematic drawing of the setup. The LED's gave outputs that were identical to those obtained from the LASER-photo transistor arrangement and worked perfectly at all test velocities. Figure 27 contain photographs of the oscilloscope traces from the two different velocity measurement setups.

8.9 Calibration of the Compressed Gas Gun

To calibrate the gas gun, 6 shots were fired at different accumulator pressures. The velocity performance of the gun is shown in figure 28. The solid line corresponds to observed values and the predicted curve is dotted. Although the results of this investigation and the data supplied by D.B.Trott match quite closely, they are

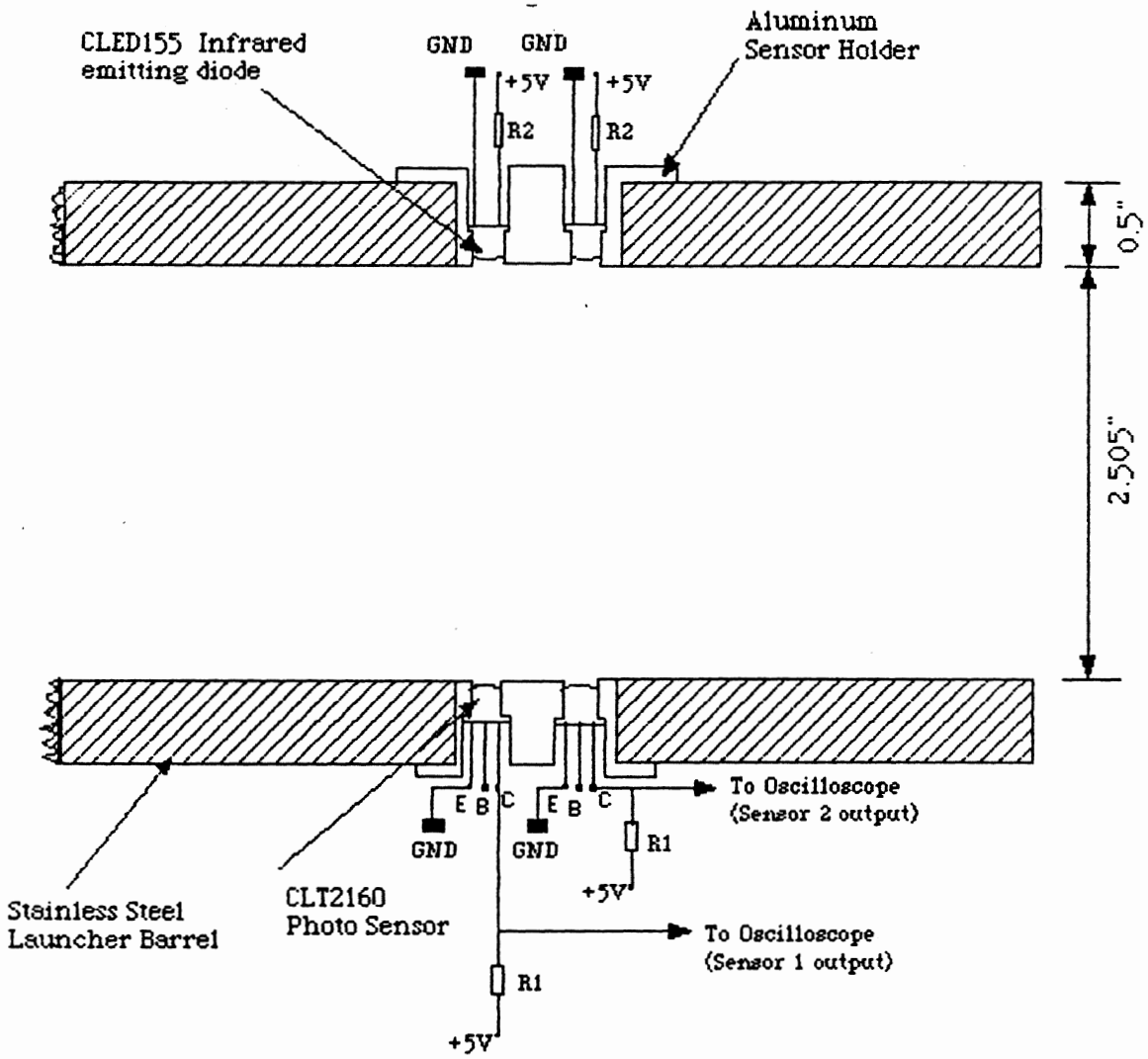

Figure 26: Schematic drawing of the LED-Photo transister velocity measuring arrangement.

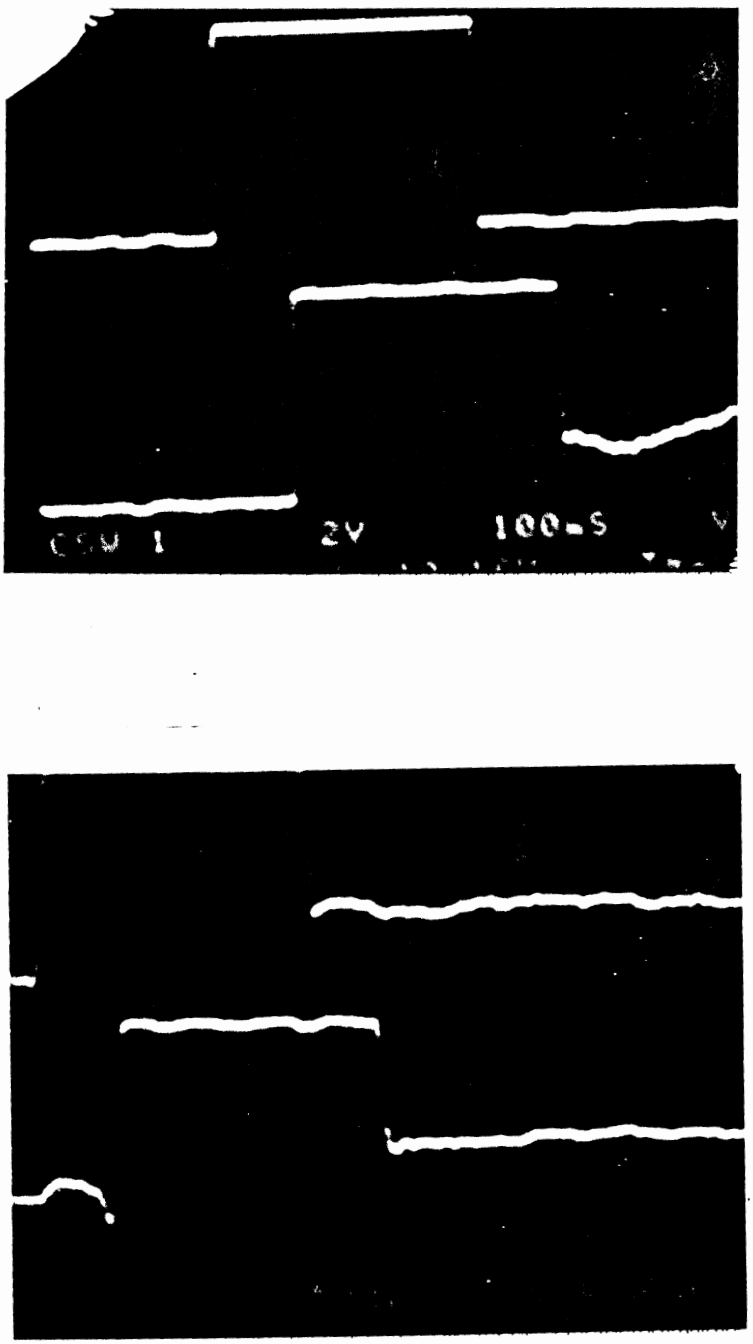

Figure 27: Above) Results obtained from the LASER velocity measuring arrangement.
Time/Div: 500 micro sec. Volt/Div: 2
Below) Results obtained from the LED velocity measuring arrangement.
Time/Div: 500 micro sec. Volt/Div: 1

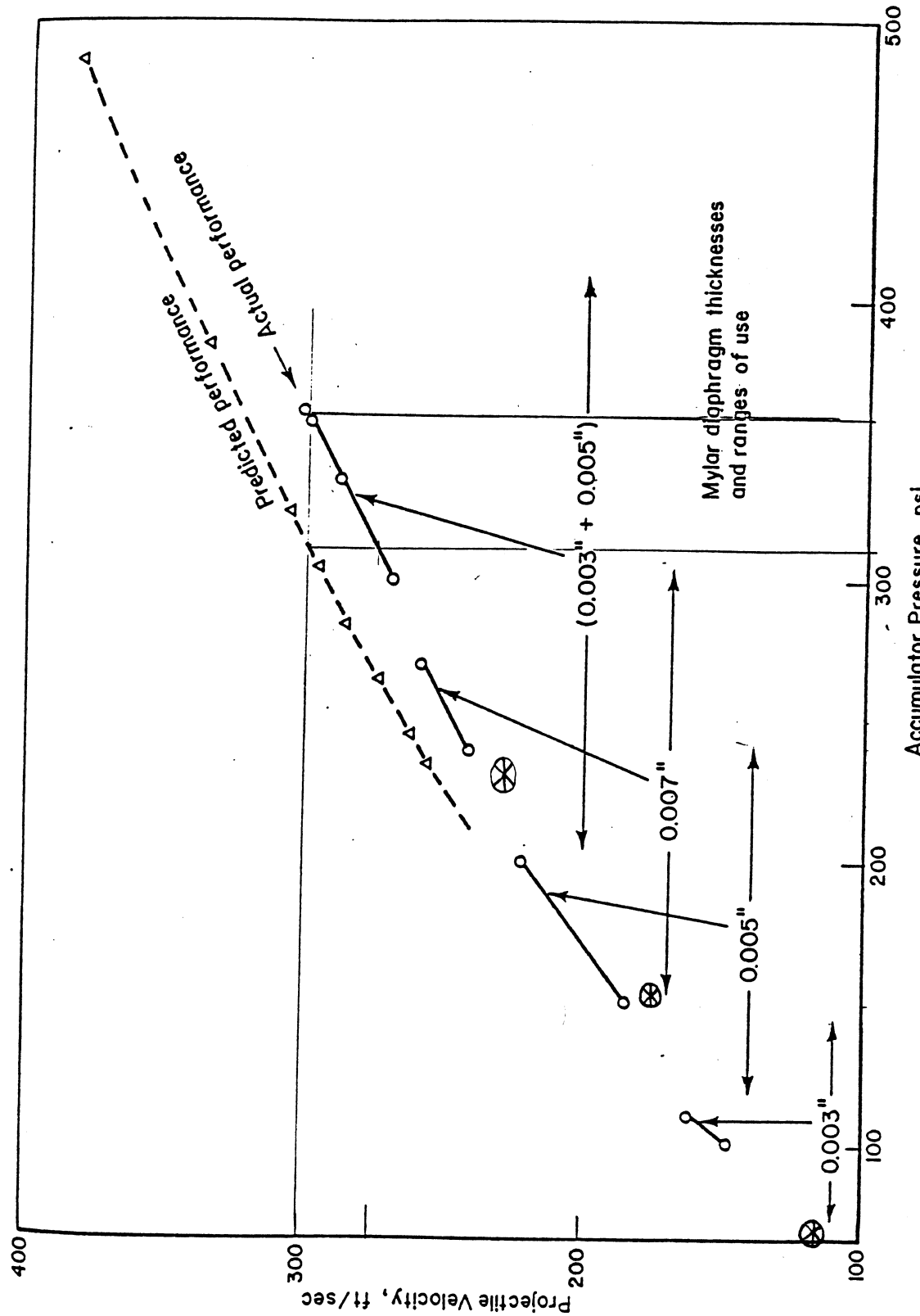

Figure 28: Observed velocity performance of the gas gun, (*) represents our results.

below the predicted performance curve. The consistent discrepancy can be attributed to the following causes:

i) No adjustment was made for the unpressurized (or low pressure) volume between the first diaphragm and the inside of the cup-shaped projectile. This space amounts to about 5.0 $inch^3$ which is 8.33 percent of the initial accumulator volume of 60 cubic inches.

ii) Projectile-barrel friction was ignored.

iii) Failure of the Mylar diaphragms to rupture completely. Not infrequently, only about one-half the bore area is opened on diaphragm rupture.

Despite the discrepancy between calculated and observed performance, the launcher has met the velocity objectives quite easily and the results were very reproducible.

8.10 Experimental Results

Early in the program a Tektronix 558A oscilloscope equipped with Model C27 camera was used to record the sensor response. However, because of the very fast shock loading, the camera was unable to record the PVDF response to the very fast shock loading. Later in our experiment, we obtained a modern Tektronix 7603 digital storage oscilloscope. This digitizer in the self triggering mode has provided the preferred recording method.

The electrical voltage produce upon impact from electrode areas of about 1.13 cm^2 range from about 90 to 380 volts in the present experiments. To reduce the signal levels to acceptable values, a 1:1181.26 voltage divider was connected to the electrodes of the gauge. The resulting signal was transmitted through a low-loss coaxial cable to the digitizing oscilloscope.

To investigate the influence of electrical orientation of the gauge on output current, some gauges were studied with the positive sensor electrode as the impact surface, as well as the standard orientation used by Bauer [29] in which the negative electrode is placed on the impact surface. In addition gauges with different sensor area were used to determine its effect on the output signal.

Figure 29 contains the recorded voltage versus time pulses records from gauges with a sensor diameter of 12 mm and a negative current orientation. The data in figures 29-A and figure 29-B indicate that different projectile velocities are obtained at the same rupture pressure. This is because in the second firing, a remachined projectile was used. Moreover, figure 29-D shows the recorded voltage in a positive current orientation. In these photographs the initial voltage jump is due to the shock wave passing through the PVDF film. During the experiment, the planarity of the impact was not measured. In the case of a perfectly plane impact, a flat topped record would be

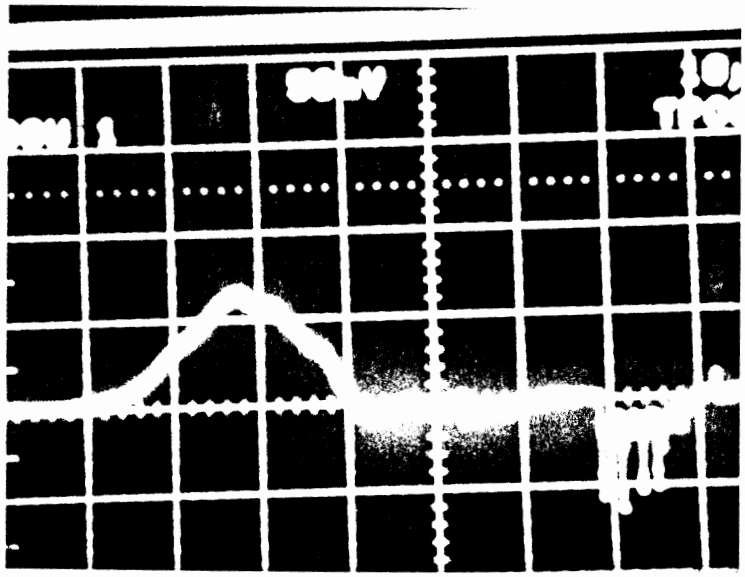

Figure 29-A: Oscilloscope record of Impact Vel. 35.55 m/sec
# of Diaphragms: 1, Rupture Pressure: 70 psi
Volt/Div: 50 mV, Time/Div: 10 micro Second.
Voltage output: 70 mV.

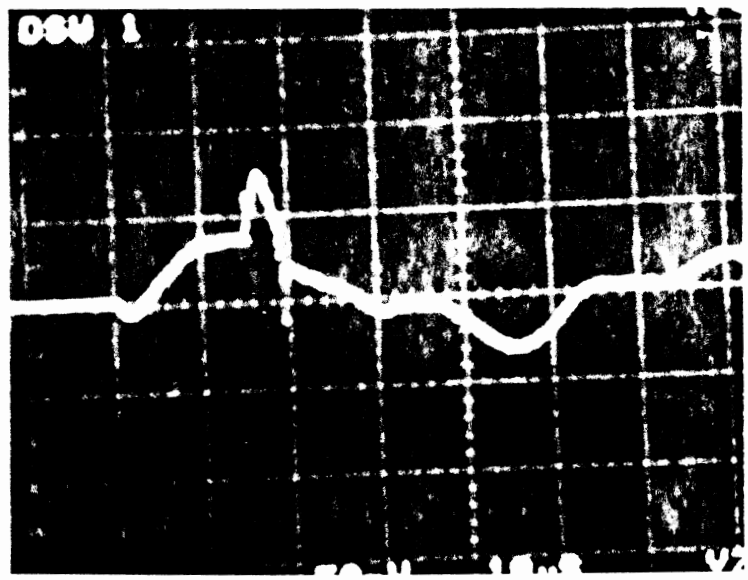

Figure 29-B: Oscilloscope record of Impact Vel. 39.00 m/sec
# of Diaphragms: 1, Rupture Pressure: 70 psi
Volt/Div: 50 mV, Time/Div: 10 micro Second.
Voltage output: 75 mV.

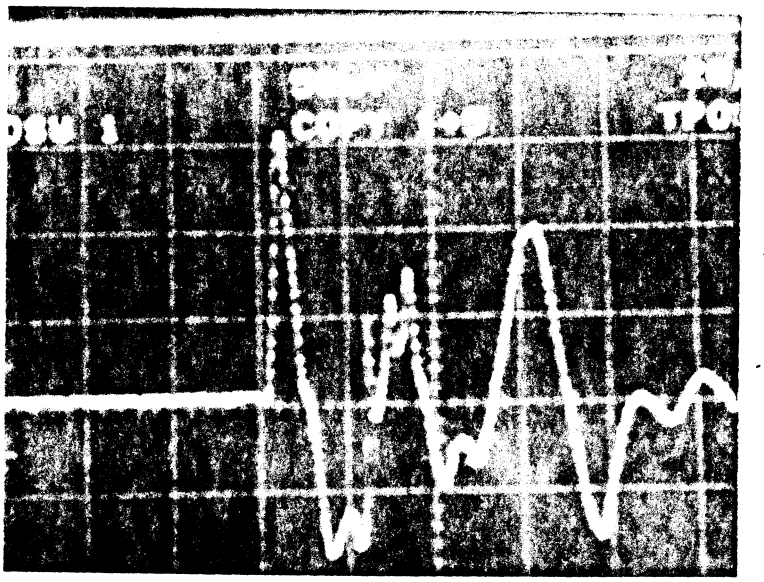

Figure 29-C: Oscilloscope record of Impact Vel. 50.80 m/sec
# of Diaphragms: 2, Rupture Pressure: 155 psi
Volt/Div: 50 mV, Time/Div: 20 micro Second.
Voltage output: 160.77 mV

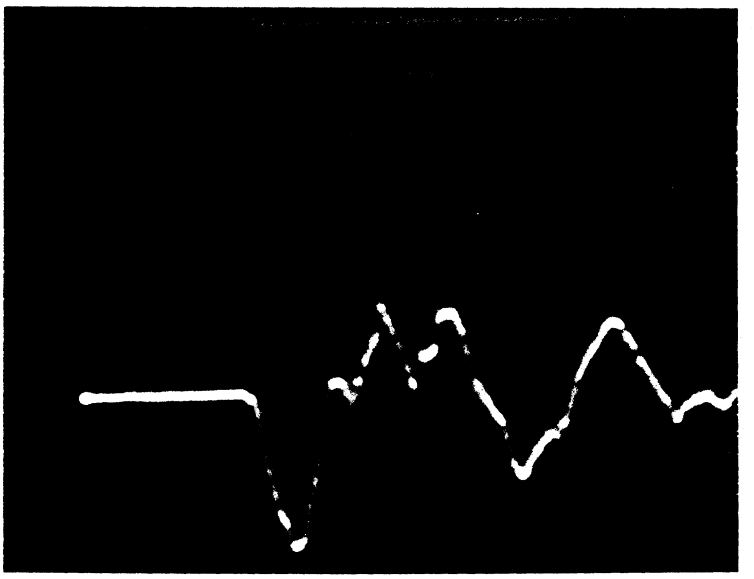

Figure 29-D: Oscilloscope record of Impact Vel. 71.03 m/sec
# of Diaphragms: 3, Rupture Pressure: 240 psi
Volt/Div: 200 mV, Time/Div: 10 micro Second.
Voltage output: 320 mV.

obtained. Our results show that the impact was not plane. After the initial jump, there was a time period during which the output of the gage was zero. This corresponds to the period during which the shock wave was propagated to the back of the sample and a rarefaction wave was reflected back to the PVDF film. The spikes of negative voltage indicates the reverberations of rarefaction waves through the PVDF film. The voltage levels obtained at different impact velocities are as follows:

IMPACT VELOCITY (m/sec)	VOLTAGE (Volts)
35.55	82.68
50.80	189.92
71.01	378.00

8.11 Numerical Simulation Results

WONDY program was used to determine the theoretical output of the PVDF film. The following material constants for copper, PVDF and Epon 828 epoxy were assumed.

	Copper	PVDF	Epon 828
Density (Kg/m^3)	8930.0	1780.0	1200.0
Sound Speed (m/sec)	3940.0	2100.0	2640.0
U_S/U_p	1.489	1.5	1.66
Poisson's Ratio	0.345	---	0.385
Gruneisen Parameter	1.99	1.5	1.5

Thickness (m)	0.0127	28E-6	0.011
Dielectric Constant	--	9.41E9 m/F	--
Piezo. stress Const.	--	6.21E8 N/C	--

The numerical results obtained from the WONDY program are shown in figure 30. A comparison of the numerical and the experimental results at selected velocities is given below:

VELOCITY (m/sec)	EXPERIMENTAL VOLTAGE OUTPUT (volts)	NUMERICAL VOLTAGE OUTPUT (volts)
35.55	82.68	89.1
50.80	189.92	193.2
71.03	378.00	402.5

Figure 31 contains a graph showing the voltage output of PVDF film v/s the stress applied. By using this graph, one can infer the stress magnitude of the shock wave based on the voltage output of the piezo film.

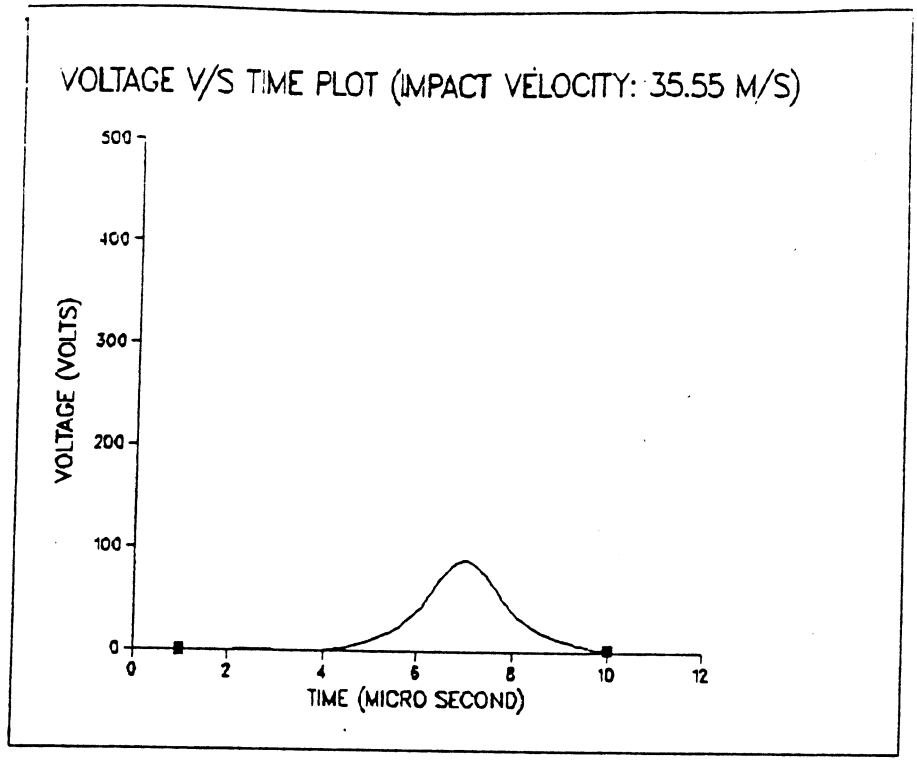

Figure 30-A: WONDY result showing the Voltage v/s Time curve for impact velocity of 35.55 m/sec.

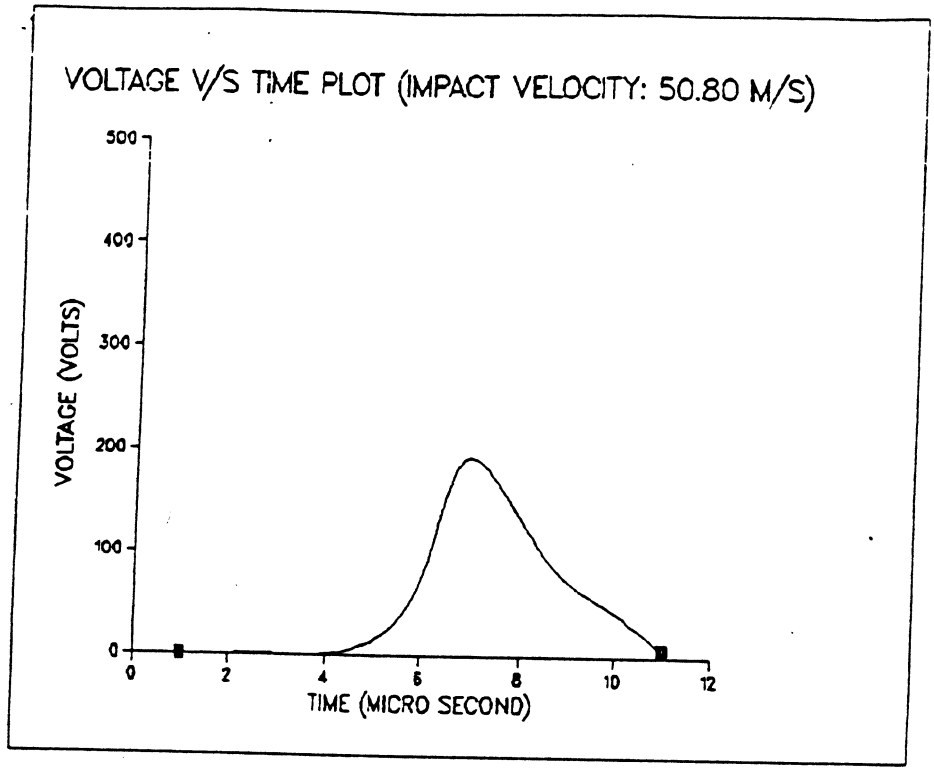

Figure 30-B: WONDY result showing the Voltage v/s Time curve for Impact velocity of 50.80 m/sec.

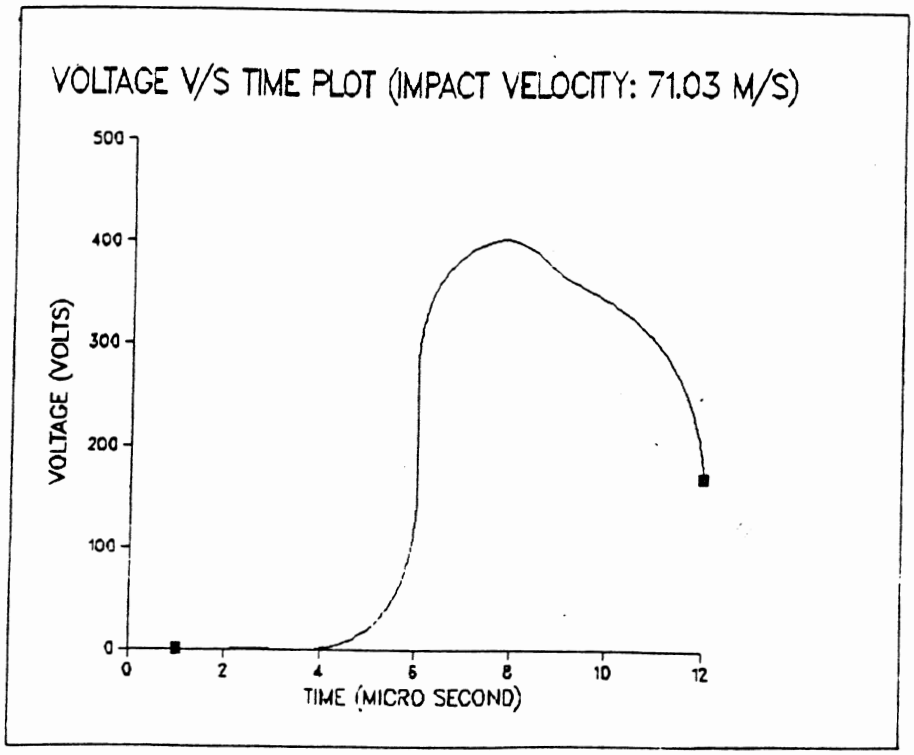

Figure 30-C: WONDY result showing the Voltage v/s Time curve for impact velocity of 71.03 m/sec.

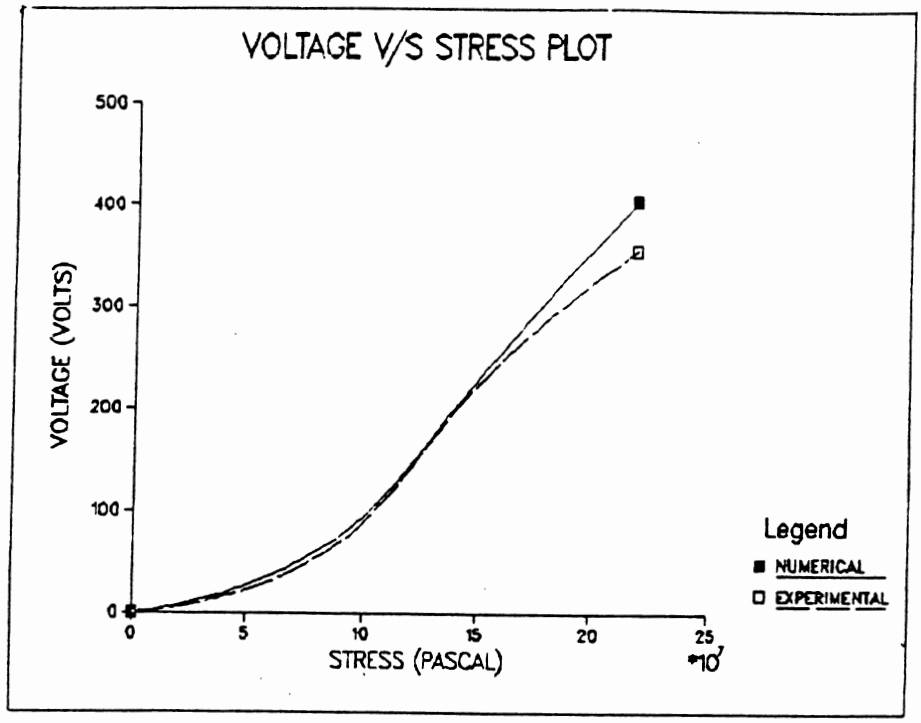

Figure 31: Experimental and Numerical voltage output of the PVDF film v/s the applied stress.

CHAPTER 9

CONCLUSIONS

The properties and principles of application of a new commercial piezoelectric material, polyvinylidene fluoride (PVDF), to the measurement of shock wave stress has been presented. This material can be economically used to measure dynamic peak stresses and stress pulse shapes in explosive and hostile environments. The material produces a large signal with good fidelity over a stress range of at least 20 GPa. These characteristics, along with its unobtrusive nature, provide a capability which does not presently exist and which can serve most measurement requirements within its limiting maximum stress.

In order to numerically simulate the behavior of PVDF film to the dynamic stress loading, a fully coupled nonlinear theory of piezoelectricity has been successfully incorporated in a general purpose computer program. A number of test problems have been solved and the computed results have been shown to be in good agreement with the experimental observations.

Numerical transient heat transfer analyses was done to determine the effects of the high temperatures to which the transducer will be subjected. The results demonstrated that the temperature at a distance of 0.5 mm from the hot

surface would not change during the response time of the PVDF film.

The present work succeeded in developing a controlled impact loading experiment in which precise shock loading can be carried out on PVDF piezoelectric polymer gages. Electronic instrumentation appropriate for the measurement of projectile velocity and the gage responses has been selected and optimized for the measurement.

A detailed study of a standardized gauge has shown that the experimental and numerical results agree with each other fairly well. The disagreement may be due to the experimental error, non-planarity of the impact and the non-reproducibility of the PVDF film source. It is well known from basic polymer physics and chemistry and from experimental studies of various physical properties of PVDF that, within the family of polymers designated PVDF, a wide range of physical responses can be anticipated. The different physical characteristics of the PVDF are sensitive to both mechanical treatment (film stretching) and electrical treatment (electrical poling of the crystallites). There are no inherent response properties independent of processing history. More work is required to determine the effect of these variables on the dynamic behavior of the PVDF film.

REFERENCES

1. Polarized Polyvinylidene Fluoride Polymer can be obtained from:
   - o Pennwalt Corporation, 900 First Avenue, P.O.Box C King of Prussia, PA 19406-0018.
   - o Thomson Lcr, France.

2. GRAHAM, R.A. & ASAY, J.R.: **"Measurements of wave profiles in Shock-loaded Solids"**, High Temperatures-High Pressures, Vol. 10, 1978.

3. GRAHAM, R.A., NEILSON, F.W. & BENEDICK, W.B.: **"Piezoelectric Current from Shock-loaded Quartz - A Submicrosecond Stress Gauge"**, Journal of Applied Physisc, Vol. 36, May 1965.

4. HARRIS, C.M. & CREDE, C.E.: Shock and Vibration Hand-Book, McGraw Hill Book Company, 1961.

5. DICK, R.D. & PARRISH, R.L.: **"Instrumentation Techniques for Monitoring Shock and Detonation Waves"**, Expermiental Techniques, August 1986.

6. COOK, M.A.: The Science of High Explosives, Reinhold Publishing Corporation, New York, 1958.

7. KELLER, R.N. & ROYCE, E.B.: **"Shock Waves in condensed media"**, Proceedings of the International School of Physics, Italian Physical Society, Lake Como, July 1969.

8. DORAN, D.G.: **"Measurement of Shock Pressures in Solids"**, presented at The High Pressure Measurement Symposium, New York City, November 1962.

9. ALEXANDER, J.M., BREWER, R.C. & ROWE, G.W.: Manufacturing Technology, Vol. 1, Ellis Horwood Ltd., 1986.

10. BERNSTEIN, D., GODFREY, C., KLEIN, A. & SHIMMIN, W.: **"Research on Manganin Pressure Transducers"**, Symposium on Behaviour of Dense Media Under High Dynamic Pressure, Paris, September 1967.

11. MCQUEEN, R.G., MARSH, S.P., TAYLOR, J.N., FRITZ, J.N. & CARTER, W.J.: **"The Equation of State of Solids from Shock Wave Studies"**, in High - Velocity Impact Phenomena, edited by KINSLOW, R. 1970.

12. GEHRING, J.W.: **"Theory of Impact on Thin Targets and Shields and Correlation with Experiment"**, in High - Velocity Impact Phenomena, edited by KINSLOW, R. 1970.

13. BLOOM, G.H.: **"Gruneisen Parameter Measurements for High Explosives"**, in Shock Waves in Condensed Matter-1981, edited by NELLIS, W.J., SEAMAN, L. & GRAHAM, R.A., American Institute of Physics, 1982.

14. MCQUEEN, R.G., MARSH, S.P. & CARTER, W.J.: **"The Determination of New Standards for Shock Wave Equation of-State Work"**, Symposium on Behaviour of Dense Media Under High Dynamic Pressures, Paris, September 1967.

15. KLEE, C., KROH, M. & LUDWIG, D.: **"Experiments on the Attenuation of Shock Waves in Condensed Media"**, in Shock Waves in Condensed Matter - 1981, edited by NELLIS, W.J., SEAMAN, L. & GRAHAM, R.A., American Institute of Physics, 1982.

16. DUVALL, G.E.: **"Shock Waves in Condensed Media"**, Proceedings of the International School of Physics, Italian Physical Society, Lake Como, July 1969.

17. ZELDOVICH, Y.B. & RAIZER, Y.P.: Physics of Shock waves and High-Temperature Hydro dynamic Phenomena, Vol. 2, Academy of Sciences, U.S.S.R.

18. REED, R.P.: **"A System for Measurement of Free-Field Stress Wave using Lithium Niobate Piezoelectric Transducers"**, presented at Ninth Transducer Workshop, Range commanders council, Transducer committee, Fort Walton Beach Florida, 26-28 April 1977.

19. INGRAM, J.K.: **"The Development of a Free-Field Soil Stress Gage for Static and Dynamic Measurements"**, Instruments and Apparatus for Soil and Rock Mechanics, ASTM STP 392, Am. Soc. Testing Mats., 1965.

20. LEE, L.M., FOGELSON, D.J. & WILLIAMS, W.D.: **"Dynamic Stress Transducer Qualification"**, in Shock Waves in Condensed Matter - 1983, edited by ASAY, J.R., GRAHAM, R.A. & STRAUB, G.K., North-Holland, 1984.

21. WILLIAMS, E.O.: **"An Etched Manganin Gage System for Shock Pressure Measurement in a High Noise Environment"**, Journal of Environment Sciences, June 1968.

22. WILLIAMS, W.D.: **"Carbon Piezoresistive Stress Gauge"**, in Shock Waves in Condensed Matter - 1983, edited by ASAY, J.R., GRAHAM, R.A. & STRAUB, G.K., North - Holland, 1984.

23. KAWAI, H.: **"The Piezoelectricity of Poly (Vinylidene Fluoride)"**, Japan Journal of Applied Physics, Vol. 8, 1969.

24. MURAYAMA, N., NAKAMURA, H., OBARA, H. & SEGAWA, M.: **"The Strong Piezoelectricity in Polyvinylidene Fluroide (PVDF)"**, Ultrasonics, January 1976.

25. BAUER, F.: **"Ferroelectric Properties and Shock Response of a Poled PVF_2 Polymer and of VF_2/C_2F_3H Copolymers"**, Institut Franco-Allemand de Recherches de Saint-Louis (ISL).

26. LEE, L.M., WILLIAMS, W.D., GRAHAM, R.A. & BAUER, F.: **"Studies of the Bauer Piezoelectric Polymer Gauge (PVF_2) under Impact Loading"**,

27. BAUER, F.: **"Piezoelectric and Electric Properties of PVF_2 Polymers under Shock Wave Action: Application to Shock Transducers"**, in Shock Waves in Condensed Matter - 1983, edited by ASAY, J.R., GRAHAM, R.A., & STRAUB, G.K., North - Holland, 1984.

28. BAUER, F.: **"PVF_2 Polymers: Ferroelectric Polarization and Piezoelectric Properties under Dynamic Pressure and Shock Wave Action"**, Ferroelectrics, Vol. 49, 1983.

29. BAUER, F.: **"Behavior of Ferroelectric Ceramics and PVF_2 Polymers under Shock Loading"**, in Shock Waves in Condensed Matter - 1981, edited by NELLIS, W.J., SEAMAN, L. & GRAHAM, R.A., American Institute of Physics, 1982.

30. CADY, W.G.: Piezoelectricity, First Edition, McGraw-Hill Book Company Inc., 1946.

31. The Second International Meeting on Ferroelectricity Kyoto, September 1969, organized by Science Council of Japan.

32. HARRIS, C.M. & CREDE, C.E.: Shock and Vibration Hand Book, Volume 1, McGraw Hill Book Company Inc., 1961.

33. FUKADA, E.: **"Piezoelectricity in Polymers and Biological Materials"**, Ultrasonics, 229, October 1968.

34. Technical Manual of **"Kynar Piezo Film"**, Pennwalt Corporation.

35. SUTHERLAND, H.J.: **"Dispersion of Acoustic Waves by an Alumina-Epoxy mixture"**, Journal of Composite Materials, Vol. 13, January 1979.

36. SUTHERLAND, H.J.: **"Acoustical Determination of the Shear Relaxation Functions for Polymethyl Methacrylate and Epon 828-Z"**, Journal of Applied Physics, Vol. 49, July 1978.

37. DRUMHELLER, D.S., TRUCANO, T.G. & CHHABILDAS, L.C.: **"Wave Code Constitutive Models: Particulate-Loaded Composites"**, SAND84-0714, Sandia National Laboratories, Albuquerque, NM, November 1984.

38. KEOUGH, D.D. & WILKINSON, W.: **"Manganin-wire Shock-Transducer Investigation"**, AFWL-TR-65-170, Stanford Research Institute, Menlo Park, CA, August 1965.

39. Epon Resin 828, Technical Bulletin, Shell Chemical Company, SC:235-85.828

40. MUNSON, D.E., BOADE, R.R. & SCHULER, K.W.: **"Stress-Wave Propagation in Al_2O_3-epoxy Mixtures"**, Journal of Applied Physics, Vol. 49, September 1978.

41. JALURIA, Y. & TORRANCE K.E.: **"Computational Heat Transfer"**, 1986.

42. GEBHART, B.: Heat Transfer, 2nd Edition, McGraw-Hill Book Company, 1971.

43. GOURDIN, W.H.: **"Prediction of Microstructural Modification in Dynamically consolidated metal powders"**, in Shock Waves in Condensed Matter - 1983, edited by ASAY, J.R., GRAHAM, R.A. & STRAUB G.K., North-Holland, 1984.

44. WALTER & PILKEY, B.: **"Shock and Vibration Computer Programs: Reviews and Summaries"**, SVM-10, the Shock and Vibration Information Center, United States Department of Defense, 1975.

45. CHESTER, C.R.: Techniques in Partial Differential Equations, McGraw-Hill Book Company, 1971.

46. BARKER, L.M. & YOUNG, E.G.: **"SWAP-9: An Improved Stress Wave Analyzing Program"**, SLA-74-0009, Sandia Laboratories, Albuquerque, NM, June 1974.

47. GIROUX, E.D.: **"HEMP User's Manual"**, UCRL-51079 Rev. 1, Lawrence Livermore National Laboratory, Livermore, CA, December 17, 1973.

48. KIPP, M.E. & LAWRENCE, R.J.: **"WONDY V - A One-Dimensional Finite-Difference Wave Propagation Code"**, SAND81-0930, Sandia National Laboratories, Albuquerque New Mexico, June 1982.

49. DAVISON, L.: **"Numerical Modeling of Dynamic Material Response"**, in Shock Waves in Condensed Matter -1983, edited by ASAY, J.R., GRAHAM, R.A. & STRAUB, G.K., North-Holland, 1984.

50. CHEN, P.J., DAVISON, L. & MCCARTHY, M.F.: **"Electrical Responses of Nonlinear Piezoelectric Materials to Plane waves of Uniaxial Strain"**, Journal of Applied Physics, Vol. 47, No. 11, November 1976.

51. LYSNE, P.C.: **"One-Dimensional Theory of Polarization by Shock Waves - Application to Quartz Gauges"**, Journal of Applied Physics, Vol. 43, No. 2, Feb. 1972.

52. DAVISON, L. & LAWRENCE, R.J.: **"Analysis of Nonlinear Plane-Wave Propagation in Piezoelectric Solids"**, Sandia Laboratories, Albuquerque, NM, 87115.

53. GRAHAM, R.A.: **"Strain Dependence of Longitudinal Piezoelectric, Elastic, and Dielectric Constants of X-Cut Quartz**, Physical Review B, Vol. 6, No. 12, December 1972.

54. TROTT, B.D.: **"Instrumented High Loading Rate Test for Impact-Member Materials"**, BMI-X-672, Battelle Memorial Institute Quarterly Report, July-Sept. 1976, October 1976, pp 29-38.

55. TROTT, B.D.: **"Instrumented High Loading Rate Test for Impact-Member Materials"**, BMI-X-676, Battelle Memorial Institute Quarterly Report, Oct-Dec. 1976, January 1977, pp 14-25.

56. Optoelectronics Designers Handbook, Clairex Electronics, Mount Vernon, New York 10550.

APPENDIX

SHOCK WAVE DATA FOR PVDF FILM

This appendix contains the shock wave data for the Kynar piezo film obtained from LASL SHCOK HUGONIOT DATA HANDBOOK, by S.P.Marsh, University of California Press, 1980. The relation between the particle veloity and the shock wave velocity for the piezo film is shown in figure A.1. From this curve the following relation is obtained.

$$U_s = 1.507447\ U_p + 2.6002$$

The shock wave data is given below:

ρ_0 (g/cm^3)	U_s (km/s)	U_p (km/s)	P (GPa)	V (cm^3/g)	ρ (g/cm^3)	V/Vo	Exp	
1.768	1.857	0.000	0.000	.5656	1.768	1.000	ssp	×
1.766	3.562	.642	4.038	.4642	2.154	.820	iml	o
1.766	3.604	.661	4.207	.4624	2.163	.817	iml	o
1.766	3.897	.816	5.616	.4477	2.234	.791	iml	o
1.766	3.963	.869	6.082	.4421	2.262	.781	iml	o
1.766	4.573	1.254	10.127	.4110	2.433	.726	iml	o
1.768	5.136	1.569	14.247	.3928	2.546	.695	iml	o
1.768	5.167	1.626	14.854	.3876	2.580	.685	iml	o
1.766	6.057	2.192	23.447	.3613	2.768	.638	iml	o
1.766	6.042	2.215	23.634	.3587	2.788	.633	iml	o
1.766	6.279	2.342	25.970	.3550	2.817	.627	iml	o
1.766	6.355	2.359	26.475	.3561	2.809	.629	iml	o
1.766	6.569	2.536	29.420	.3476	2.876	.614	iml	o
1.766	6.891	2.810	34.196	.3353	2.982	.592	iml	o
1.766	6.910	2.864	34.950	.3316	3.016	.586	iml	o
1.766	7.264	3.004	38.536	.3321	3.011	.586	iml	o
1.766	7.400	3.165	41.361	.3241	3.086	.572	iml	o
1.766	7.479	3.242	42.820	.3208	3.117	.567	iml	o
1.766	7.785	3.418	46.992	.3176	3.148	.561	iml	o
1.766	8.152	3.789	54.548	.3031	3.300	.535	iml	o
1.768	8.479	3.916	58.704	.3044	3.285	.538	iml	o
1.768	8.730	4.091	63.143	.3006	3.327	.531	iml	o
1.766	8.652	4.101	62.661	.2979	3.357	.526	iml	o
1.768	8.931	4.237	66.902	.2973	3.364	.526	iml	o
1.766	9.055	4.241	67.818	.3010	3.322	.532	iml	o
1.766	9.412	4.578	76.094	.2908	3.438	.514	iml	o
1.768	9.208	4.579	74.545	.2843	3.517	.503	iml	o

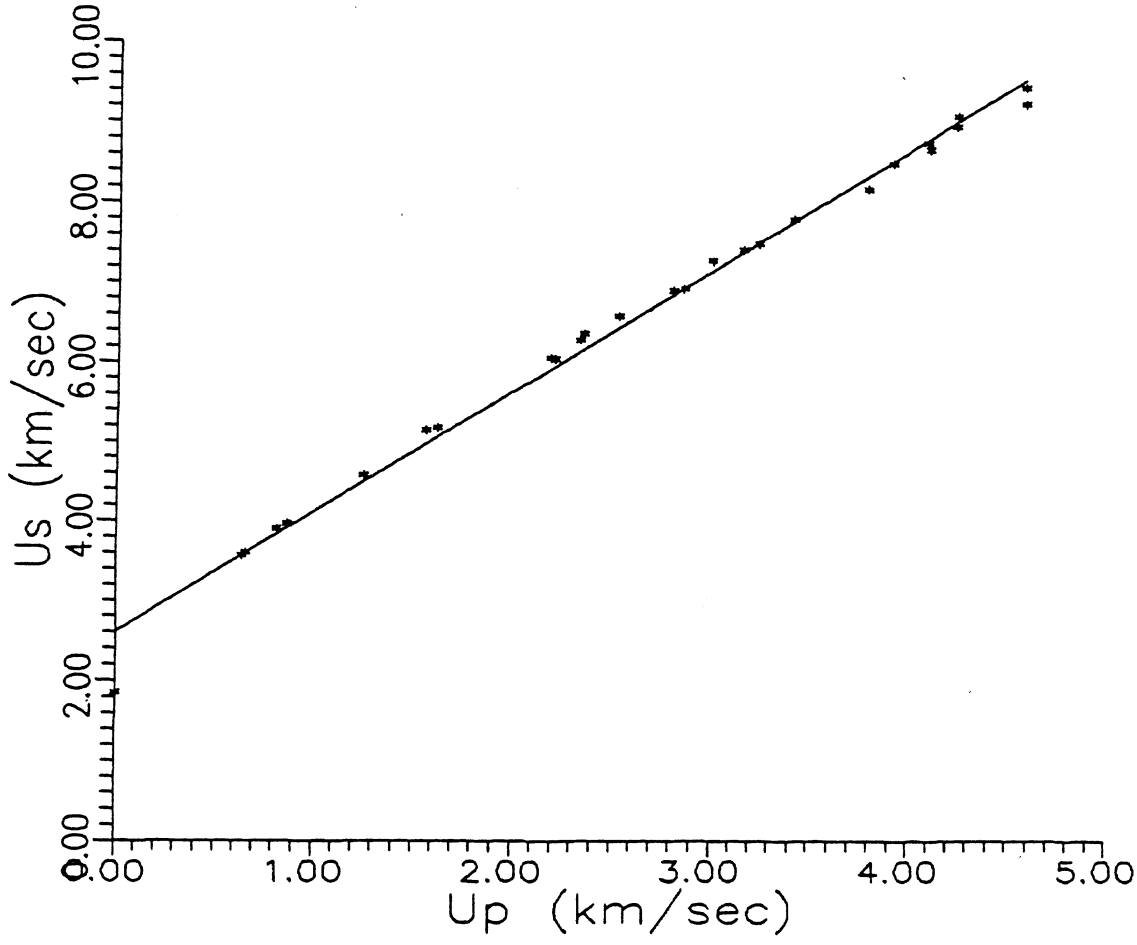

Figure A.1: Particle Velocity v/s Shock wave velocity for the Piezo film.